Light trapping in thin-film solar cells using dielectric and metallic nanostructures

Cover image: The front shows a glass substrate printed with an array of nanoholes in a silica sol-gel layer, illuminated from the top with a supercontinuum light source. The nanopattern leads to trapping of the incident light inside the glass layer. The light propagates in the plane of the glass layer and radiates out at the edges. Diffraction of the hole array leads to the colorful projection observed at the left side of the sample. The back shows a color edited scanning electron image of a cross section of a thin-film a-Si:H solar cell, grown on top of a light trapping pattern.
(photograph on front by Mark Knight)

Ph.D. thesis University of Amsterdam, October 2014
Light trapping in thin-film solar cells using dielectric and metallic nanostructures
Marie-Claire van Lare

ISBN nr 978-90-77209-85-1

A digital version of this thesis can be downloaded from http://www.amolf.nl.

LIGHT TRAPPING IN THIN-FILM SOLAR CELLS USING DIELECTRIC AND METALLIC NANOSTRUCTURES

Lichtverstrooiing in dunne-film zonnecellen met behulp van diëlectrische en metallische nanostructuren

ACADEMISCH PROEFSCHRIFT

ter verkrijging van de graad van doctor
aan de Universiteit van Amsterdam
op gezag van de Rector Magnificus
prof. dr. D. C. van den Boom
ten overstaan van een door het college voor promoties
ingestelde commissie,
in het openbaar te verdedigen in de Agnietenkapel
op dinsdag 7 oktober 2014, te 12:00 uur

door

Marie-Claire van Lare

geboren te Vlissingen

Promotiecommissie

Promotor:	Prof. dr. A. Polman
Copromotor:	Prof. dr. R. E. I. Schropp
Overige leden:	Prof. dr. T. Gregorkiewicz
	Prof. dr. W. C. Sinke
	Prof. dr. A. F. Koenderink
	Prof. dr. J. Knoester
	Dr. F. Haug

Faculteit der Natuurwetenschappen, Wiskunde en Informatica

This work is part of the research program of the 'Stichting voor Fundamenteel Onderzoek der Materie' (FOM), which is financially supported by the 'Nederlandse organisatie voor Wetenschappelijk Onderzoek' (NWO). It is also supported by the European Research Counsel.

Contents

1

Introduction

1.1 Global energy demand and photovoltaics

Ever since the late nineteenth century, global energy demand has been growing continuously [1]. Despite the economic crisis in 2009, the energy consumption has grown by 48% from 1990 to 2010 [2]. In 2013, the global energy use amounted to 18 TW. This number will grow further because of the rapidly growing world population and fast economic growth in countries such as India and China. With the current energy policy, a worldwide growth of 45% is predicted by 2035 [3]. Presently, fossil fuels dominate the energy market. In 2010 81% of the energy consumed globally was obtained from fossil fuels (36% oil, 24% coal, and 21% natural gas) [3]. Because of limited resources and environmental issues due to CO_2 production by fossil fuels, exploration of renewable energy sources is required. Among these sources, the sun is a promising candidate. It provides more than 1000 times our current global energy demand. Furthermore capturing the sun's energy allows for distributed rather than centralized generation of energy.

There are several technologies that can be used to harvest the sun's energy: Solar thermal technology involves the conversion of sunlight to heat for domestic use or for conversion to electricity. Sunlight can be turned into chemical energy by production of solar fuels. Photovoltaics (PV) is the direct conversion of sunlight to electricity. This thesis focuses on photovoltaics.

For photovoltaic power generation, solar modules are used, which are composed of a number of solar cells. The first practical solar cell was demonstrated in 1954, at Bell Labs. It was a crystalline Si (c-Si) solar cell with an efficiency of 6% [4], which has gradually increased over the past 60 years. The current record

efficiency for a laboratory Si cell, with a large area of 144 cm^2, is 25.6% [5]. This cell has a complex design and the record module efficiency is well below this number; it amounts to 22.9% [5]. Currently, standard commercial Si module efficiencies are 15–20%. Not only have conversion efficiencies increased, installed capacity has grown tremendously as well. From 2007 to 2013 the installed capacity has increased more than ten-fold from 3.1 GW to 37 GW [6].

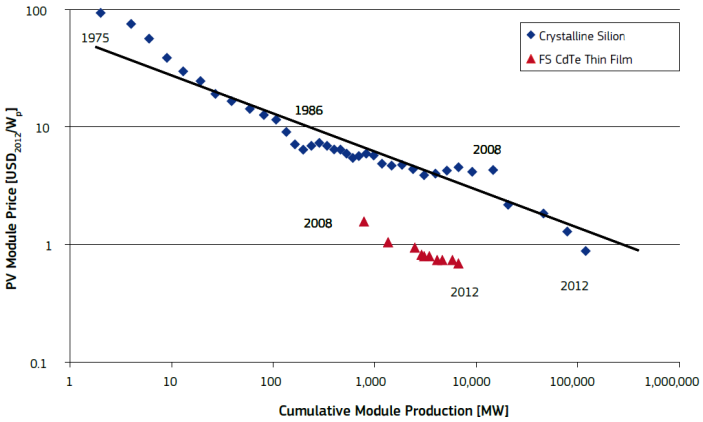

Figure 1.1: Actual module prices for c-Si solar modules as a function of cumulative production volume (blue) with a linear fit through the (logarithmically-plotted) data (black). Prices are also shown for CdTe modules (red). From: [6].

Figure 1.1 shows the module prices as a function of cumulative production for c-Si (blue) and thin-film CdTe (red) cells. The trend that can be observed for c-Si modules is that each time the cumulative production doubles, the price goes down with 20%. CdTe modules (red) start at a lower price, but follow a similar learning curve. This price trend was driven both by economies of scale and technological developments. Although PV electricity consumer prices have reached grid parity in some countries, a further cost reduction is required for PV to be fully competitive with conventional energy sources.

1.2 Reducing cost per watt

In order to reduce the cost per watt of generated energy, two approaches are used. First, the cell efficiency can be increased, while minimizing the increase in production cost. For single-junction solar cells, the theoretical maximum efficiency is given by the Schockley-Queisser (SQ) limit [7], which gives a theoretical maximum for the cell efficiency depending on the material's bandgap. This model assumes the cell is in thermal equilibrium with its environment through black-body radiation, recombination occurs by radiative recombination

only, and it takes into account the quantum defect, the fact that a high-energy photon always creates a photovoltage less than the potential corresponding to the photon energy. The SQ limit for c-Si solar cells with a band gap of 1.12 eV is 33%. It should be noted that for most materials it is practically impossible to reach the radiative-recombination limit. To overcome the SQ limit for single-junction solar cells, multi-junction cells [8, 9], hot-carrier cells [10, 11], intermediate band cells [12, 13], and up- or downconversion [14, 15] are among the concepts being studied. Up to now, except for multi-junction cells, these concepts are still in the research stage and focus has been mostly on proof-of-concept. Second, instead of increasing the cell's efficiency, the cost per watt can also be reduced by decreasing the cell's manufacturing cost while maintaining the original efficiency. This can be done by using less expensive materials and reducing the thickness of the absorber layer [16]. Nanophotonics plays an important role in both approaches [17]. In this thesis we will focus on reducing device cost by decreasing the thickness of the device.

1.3 Thin-film solar cells

Thin-film (TF) solar cells are cells made of materials with relatively large absorption coefficients with thicknesses ranging from a few 100 nm to a few μm. For most thin-film solar cell types, the carrier recombination properties of the absorber materials do not allow for larger thicknesses. Furthermore certain types of thin-film solar cells make use of scarce materials (Te, In), which also requires the use of absorber layers that are as thin as possible. Whereas c-Si solar cells are made from wafers, diced from ingots, TF cells are made by bottom-up approaches to grow materials on (flexible) substrates or superstrates. Table 1.1 shows the record cell efficiencies of different types of laboratory thin-film solar cells compared to c-Si cells [5].

Cell type	Efficiency (%)
c-Si	25.6
CIGS	20.8
CdTe	20.4
Perovskite	17.9
a-Si:H (triple-junction)	13.4
Dye-sensitized	11.9
Organic	11.1

Table 1.1: Different solar cell technologies with their corresponding record efficiencies.

Thin-film technologies that have already penetrated the market are hydrogenated amorphous Si (a-Si:H), CdTe, and Cu(In,Ga)Se_2 (CIGS) [18]. In 2013, CdTe had the largest market share of these technologies with 56%, and a-Si:H and CI(G)S both had a market share of 22% [19]. For these technologies, the module efficiencies are substantially lower than their cell efficiencies. The independently confirmed record efficiencies for modules are 16.1%, 15.7%, and 10.9% for CdTe, CIGS and a-Si (triple junction) modules respectively [5]. The other thin-film technologies have not penetrated the market yet at large volumes. A major problem of thin-film solar cells is the incomplete absorption of the above bandgap part of the solar spectrum. Figure 1.2 shows the AM1.5 solar spectrum (green) together with the spectrum that is absorbed in a 350 nm a-Si slab for a single pass (blue) and a double pass (black), assuming a perfect mirror on the back. The band gap for a-Si is near 800 nm. A substantial fraction of the above-bandgap light is not absorbed in the thin absorber layer. To solve this problem light trapping is required, in which scattering structures are integrated in the solar cells to enhance the absorption of the sunlight [20].

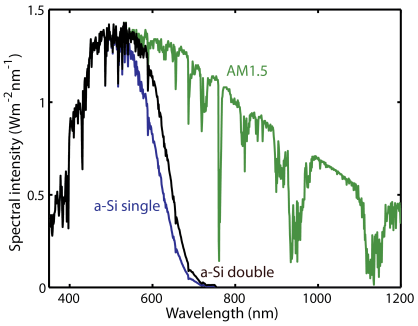

Figure 1.2: AM1.5 spectral intensity as a function of wavelength (green) and the amount of power absorbed in a 350 nm a-Si slab assuming a single pass (blue) and a double pass (black).

1.4 Light trapping

Scattering structures integrated in solar cells can enhance light absorption in multiple ways. The path length of a single pass through the absorber layer is enhanced since the scattered light propagates at off-normal angles. If this angle is larger than the critical angle, light is trapped by total internal reflection. Furthermore the angular redistribution gives the light parallel momentum which facilitates coupling to in-plane waveguide modes [20–22]. If the scattering structures are at the front side of the device they can also lead to enhanced incoupling of the light, since they preferentially scatter the light into the high-index absorber layer [20, 23].

Conventionally, light trapping in thin-film solar cells is achieved by growing the cells on top of textured transparent conductive oxides (TCO). However, these completely random patterns offer a very broad distribution of spatial frequencies and not all of these spatial frequencies are in the range that is useful for light trapping. In this thesis we study periodic and random arrays of nanoparticles that resonantly scatter the light. Both metallic and dielectric particles with sizes of the order of the wavelength can exhibit resonances, but the mechanisms on which these resonances rely are different due to the intrinsic differences in optical constants for metals and dielectrics. In metallic nanoparticles the resonance originates from the collective excitation of the free electrons in the metal by the electric field of the light. This phenomenon is called a plasmon resonance [24]. Dielectric particles exhibit resonances in which the light is confined in a well-defined geometrical mode inside the particle [25]. For spheres and infinite cylinders inside a homogeneous medium these resonances are also called Mie resonances, after the German physicist Gustav Mie.

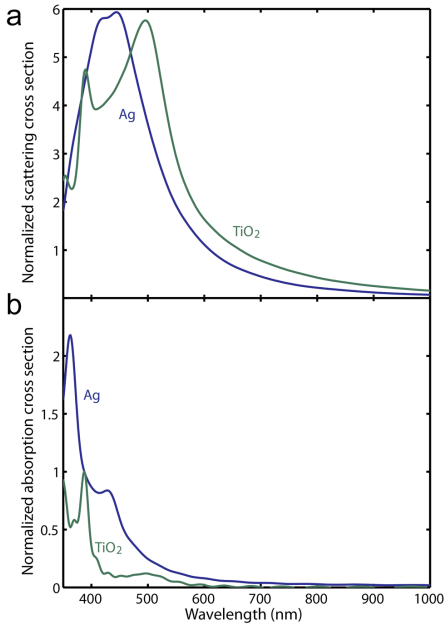

Figure 1.3: FDTD-simulated **(a)** normalized scattering cross sections for Ag sphere with d=120 nm and TiO_2 sphere with d=200 nm in air and **(b)** normalized absorption cross sections for the same particles.

An important design criterion for light trapping patterns is not only efficient scattering of the light, but also keeping absorption losses in the scatterers to a minimum. Figure 1.3a shows the absorption and scattering cross sections normalized to the geometrical cross sections for a single Ag sphere (d=120 nm)

and TiO_2 sphere (d=200 nm) in air. Data is shown for wavelengths starting at 350 nm, which is where the AM 1.5 starts to have significant intensity. Both particles show normalized scattering cross sections of 6, meaning that the scattering cross section is 6 times as large as the geometrical cross section. Figure 1.3b shows the normalized absorption cross section for the same particles. Whereas both particles have comparable scattering cross sections, the absorption cross section is substantially larger for the Ag particle. In this thesis we will study both dielectric and metallic scatterers for light trapping in different geometries. We apply the scattering patterns to front and back-side of both a-Si:H and CIGSe solar cells.

1.5 Outline of this thesis

In Chapter 2 we present the fabrication of nanoscale light trapping patterns using substrate conformal imprint lithography (SCIL). We fabricate arrays of dielectric and metallic light trapping patterns both at the front and back side of solar cells using SCIL in combination with evaporation and lift off. By sputter coating printed sol-gel layers with metals, we fabricate patterned metal back contacts.

In Chapter 3 we study light trapping in ultra-thin a-Si:H solar cells grown on top of periodically and randomly patterned metal back contacts. We show efficient light trapping due to scattering at the corrugated back contact as well as an enhanced blue-response that we attribute to geometrical resonances in the top of the device.

In Chapter 4 we print periodic arrays of metal nanoparticles on top of completed a-Si:H solar cells. We find an enhanced red response for the patterned device and relate peaks in external quantum efficiency to coupling of the scattered light to waveguide modes in the absorber layer. We find that the patterning also leads to a reduced blue-response, due to Fano resonances at wavelengths below the resonance and absorption in the nanoparticles. We show that by optimizing the array geometry we can also enhance the blue response of the cells. Finally we show that with dielectric nanoparticles we can even further enhance the absorption in the active layer of the cells.

In Chapter 5 we study the role of dielectric scatterers in a geometry similar to the geometry studied in Chapter 3. We explore the influence of patterning the dielectric buffer layer that is in between the metal and the absorber layer and we find that patterning this dielectric layer is indispensable for efficient light trapping in these devices.

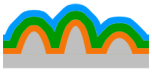

In Chapter 6 we study light trapping in thin-film a-Si:H solar cells grown on top of random arrays of ZnO nanorods. We find again that conformal growth of the devices results in a nanopattern at each interface of the device. The nanorod devices show efficient light trapping, and simulations show that they can be further improved by flattening the metal back contact and only patterning the

dielectric layers.

Chapter 7 presents solar cells on top of purely dielectric scattering patterns. The metal is completely flat and only the AZO layer on top of the metal is patterned. This purely dielectric scattering pattern results in very efficient light trapping and outperforms a geometry with patterned metal.

The dielectric scatterering patterns that are explored in previous chapters, are applied to achieve light trapping in ultra-thin CIGSe solar cells in Chapter 8. We find that scattering patterns at the front side of the device lead to an anti-reflection effect while no enhanced light trapping is observed. By patterning the back of the device, we demonstrate efficient light trapping and substantially reduced parasitic absorption in the highly absorbing Mo back contact.

Finally, in Chapter 9 we study the importance of the spatial frequency distributions in light trapping patterns. We compare periodic and random patterns and optimize a random pattern to have an elevated power spectral density in the frequency range that is required for waveguide mode coupling. We present an approach to make light trapping patterns that can be tailor-made for a specific frequency range and does not require patterning of the active layer, which makes them applicable to all thin-film solar cell concepts.

Overall, this thesis provides fundamental insights in light trapping concepts for thin-film solar cells. We compare metallic and dielectric scattering patterns and demonstrate the importance of minimizing absorption losses in the scattering pattern. We relate the spatial frequencies of scattering patterns to light trapping in thin-film solar cells and present an approach to optimize scattering patterns. The concepts presented in this thesis are applicable to all thin-film solar cell geometries.

2

Nanofabrication methods

We present large-area fabrication of periodic and engineered random nanopatterns for light trapping in thin-film solar cells using substrate-conformal imprint lithography (SCIL) combined with reactive ion etching, evaporation and lift off. This fabrication procedure is applied to both completed solar cells and on substrates onto which the absorber layer is grown. It is compatible with different solar cell layer materials, including transparent conductive oxides and can be applied directly onto metal front grids.

2.1 Introduction

Nanofabrication is the production of structures with at least one dimension below 1 μm. Many methods exist for the fabrication of nanostructures including electron-beam lithography (EBL), focused ion-beam (FIB) milling, UV-lithography, hole-mask colloidal lithography, chemical synthesis, and island annealing [26–31]. All methods have their advantages and disadvantages. For fabrication of nanostructures on solar cells scalability is extremely important. Furthermore, to study light coupling and trapping using nanopatterns and to design the optimal light trapping pattern, it is important to have a high degree of control over the fabricated structure.

Nanofabrication using EBL or FIB milling gives the freedom to fabricate periodic as well as engineered random particle arrays, or any other desired structure. The major drawback of EBL and FIB milling is that these methods

are not suitable for large-area fabrication, since they are relatively slow and expensive. Therefore they can not be used for the fabrication of nanostructures on solar cells at the centimeter scale or larger. UV-lithography does allow for patterning of wafer-scale samples. However the resolution of this method is limited by the diffraction limit. Furthermore, UV lithography does not allow as much flexibility in the pattern as FIB milling or EBL. Methods like island annealing, chemical synthesis, and colloidal hole-mask lithography are inexpensive and scalable, but do also not give the amount of control over the pattern geometry that is desired.

Nanoimprint lithography enables large-scale fabrication of arbitrary patterns [32–38]. These patterns are based on the replication of a master pattern in a resist layer by a stamp, which is the inverse of the master pattern. Conventional nanoimprint lithography makes use of rigid stamps which obstructs conformal contact between the stamp and the sample surface [34]. Particularly for printing of nanopatterns on solar cells this is a problem, since device fabrication usually occurs in a non-cleanroom environment which increases the probability on contamination on the sample surface. Furthermore, when printing on the front-side of a completed thin-film solar cell, metal grids are often present. Contamination and metal grids would not only prevent conformal coating by nanoimprint lithography, they could also damage the rigid stamps. To solve these problems, soft PDMS stamps are often used, which allow for conformal patterning on non-flat surfaces [32]. However, the spatial resolution of nanopatterns made using soft stamps is limited due to deformation of the stamp.

2.2 Substrate conformal imprint lithography

Substrate conformal imprint lithography (SCIL) combines the resolution of nanoimprint lithography with the conformal-coating ability of soft imprint lithography and is therefore perfectly suitable for the fabrication of light trapping patterns for thin-film solar cells [39]. To accomplish this, SCIL makes use of a bilayer stamp. A thin high-Young's modulus X-PDMS layer (typical thickness 50–100 μm) holds the nanoscale features; the high Young's modulus of this material avoids nanoscale features to stick together or collapse and hence allows for high-resolution patterning. The thin X-PDMS layer is laminated onto a thick low-Young's modulus PDMS layer that gives the stamp mechanical flexibility and allows for conformal contact with non-flat samples. The SCIL technique used in this thesis was developed by Verschuuren et al. at Philips Research [39]. The flexible stamp can be applied either by hand or using a dedicated SCIL tool onto a liquid sol-gel layer that is spin-coated on a sample. The sol-gel consists of two different liquid alkoxide precursors, namely tetramethylorthosilicate (TMOS, $Si(OCH_3)_4$) and methyltrimethoxysilane (MTMS, $C_4H_{12}O_3Si$) in alcohol and water, which is acidified to catalyze hydrolysis of the precursors. Si-O-Si bonds are formed mostly by hydrolysis and

condensation; in parallel other chemical reactions occur [39]. When the reaction mixture has reached a certain degree of hydrolysis and condensation, it can be spin-coated onto a substrate to form a thin-film. During the spin coating process alcohol and water are removed from the reaction mixture which further promotes the formation of a silica network. The mixture also contains a small volume fraction of the high-boiling a-polar solvent 2-ethoxy-ethyl ether, which remains in the resist after spin-coating and diffuses into the a-polar PDMS stamp during the imprint process.

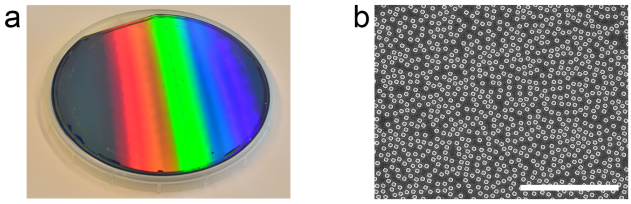

Figure 2.1: **(a)** Photograph of 6 inch Si wafer with a sol-gel layer that is patterned using SCIL. **(b)** SEM image of an engineered random array of sol-gel particles, fabricated using SCIL. The scale bar indicates 5 μm.

Figure 2.1a shows a photograph of a full 6" wafer that is patterned with sol-gel particles using SCIL. This demonstrates the scalability of this nanofabrication method. Figure 1b shows an SEM image of an engineered random array of sol-gel nanoparticles on Si that is fabricated using SCIL. In this thesis, SCIL is used to fabricate arrays of nanoparticles in different sections of the device.

2.3 Fabrication of nanoparticle arrays

Figure 2.2 schematically shows the steps of the process to make nanoparticles. Prior to these steps the samples are cleaned by rinsing with isopropanol (i-PrOH) and N_2 blow-drying. Figure 2.2a shows the first fabrication steps. First, the sample is spin-coated with PMMA (35k 300) in a spincoater (Suss Delta 80) with closed cover at a rotation speed of 1000 rpm. Depending on the desired particle height, this step is done with co-rotating lid, which results in a layer thickness of 300 nm, or without co-rotating lid, which results in a layer thickness of 550–600 nm. Thinner layers than 300 nm could be obtained by increasing the rotation speed. The layer thickness should be chosen such that it equals 2–3 times the desired particle height. After spin coating, the PMMA layer is baked in air at 150 °C for 15 minutes to obtain cross linking in the PMMA layer and make it insoluble in the silica sol-gel. Subsequently, the PMMA surface is made hydrophilic by a 3s low-bias O_2 reactive ion etch (RIE). Then, a layer of silica sol-gel is spin coated onto the sample in a multistep process. The layer thickness is determined by a 45 s step with closed cover; this is done at 800 rpm, which results in a 70 nm sol-gel layer. This is followed by a 2s 1000 rpm step to remove

thick liquid on the substrate edge, and finally the sample spins without cover to allow further evaporation of the water and alcohol.

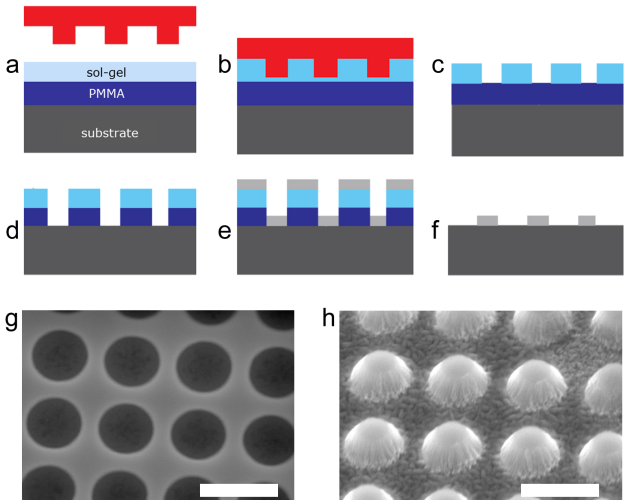

Figure 2.2: **(a)-(f)** Schematic overview of the fabrication steps to make nanoparticles using SCIL, showing the sample after **(a)** spin coating PMMA and sol-gel, **(b)** printing an array of holes using a SCIL stamp, (c) RIE etching to remove the residual sol-gel layer, **(d)** RIE etching to transfer the holes to the PMMA layer, **(e)** evaporation, and **(f)** lift off. **(g)** SEM image of an array of holes in the sol-gel layer, printed using SCIL, after the double-step breakthrough etch. **(h)** SEM image of an array of SiO_2 nanoparticles, printed onto a Mo layer on glass. The scale bars in (g) and (h) indicate 500 nm.

After spin coating of the sol-gel layer, the PDMS stamp, which contains an array of nanopillars, is molded in the sol-gel (Figure 2.2b) by hand; first the stamp is brought into contact with the sol-gel layer close to the left edge of the sample. Contact between the stamp and the liquid sol-gel layer is facilitated by the capillary forces of the patterned layer in the stamp. Then the right side of the stamp is gradually lowered in order to let the contact front advance over the sample until full contact is obtained. The resist is cured at room conditions for 20 minutes. After removal of the stamp an array of nanoholes is obtained with a residual layer of sol-gel. An anisotropic RIE process, using a gas mixture of CHF_3 and Ar is used to remove the residual sol-gel layer without significantly increasing the diameter of the holes (Figure 2.2c). The holes are then transferred to the PMMA layer using a low-bias O_2 RIE process (Figure 2.2d). The last RIE is deliberately carried out for a longer time than required to etch through the PMMA layer (12 min, when 3 min are required) in order to create an undercut profile in the resist and thereby facilitate the lift-off of the mask. After this breakthrough etch the desired material can be evaporated (Figure 2.2e) onto the mask. In this thesis, nanoparticles of different

materials are studied. SiO_x and Ag are thermally evaporated, and SiO_2 and TiO_2 are deposited using electron beam (e-beam) evaporation. The evaporation process is followed by lift off of the mask, which is done by dissolving the PMMA in 50°C acetone, followed by i-PrOH rinse and N_2 blow-dry, which results in an array of nanoparticles on top of the sample (Figure 2.2f). In the thesis, the nanoparticle fabrication is carried out on top of different materials including ITO, Al-doped ZnO (AZO), Mo, and Si. In this process the only solvents used are i-PrOH and acetone, which do not react with any of these materials, including the easily-soluble AZO. Figure 2.2g and h show SEM images of two stages of the fabrication process on top of Mo on glass. Figure 2.2g shows the holes in the resist after the two-step breakthrough etch, and Figure 2.2h shows an array of SiO_2 particles on top of the Mo.

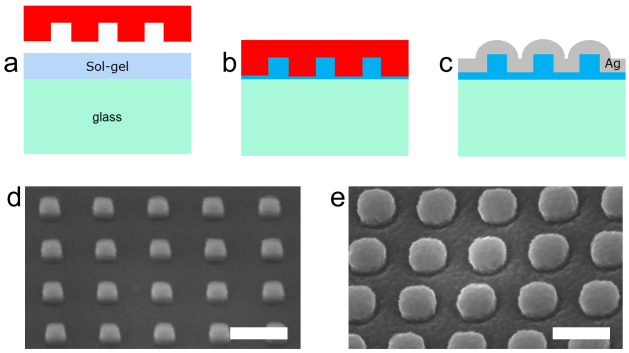

Figure 2.3: **(a)-(c)** Schematic overview of the fabrication steps to make patterned metal back contacts using SCIL, showing the sample after **(a)** spin coating sol-gel, **(b)** printing an array of sol-gel pillars using a SCIL stamp, (c) sputter coating with metal. **(d)** SEM image of an array of sol-gel pillars on Si, printed using SCIL. **(e)** SEM image of a patterned Al back contact. The scale bars in (d) and (e) indicate 400 nm.

2.4 Fabrication of patterned metal back contacts

Figure 2.3 depicts the fabrication process for a patterned metal back contact using SCIL. First a flat AF45 glass substrate is spin-coated with a 100 nm layer of silica sol-gel (Figure 3a). Then a stamp with nanoholes is applied onto the sol-gel layer. The sol-gel is cured for 20 minutes followed by release of the stamp which results in a sol-gel layer that is patterned with an array of sol-gel particles. The sol-gel particle array is post-cured at 200 °C (Figure 2.3b). Subsequently, the patterned sol-gel layer is sputter-coated with metal, to form a patterned metal back contact (Figure 2.3c). Figure 2.3e shows a SEM image of an array of sol-gel particles, printed by SCIL onto a Si wafer. Figure 2.3d shows

a SEM image of a patterned metal back contact, composed of a sol-gel pattern coated with 200 nm Nd-doped Al.

2.5 Printing on solar cells with metal grids

In this thesis we also print arrays of nanoparticles on top of completed thin-film solar cells with metal grids. Particles are printed onto two types of thin-film solar cells, namely hydrogenated amorphous Si (a-Si:H) and Cu(In,Ga)Se (CIGSe) cells. Since the CIGSe cells generate significantly more current, these cells require the thickest metal grids. The CIGS cells used in this thesis have metal grids of up to 2 μm on top. Figure 2.4a shows photograph of a 2.5 × 2.5 cm^2 CIGSe solar cell substrate, divided into 8 small solar cells, with metal grids, consisting of 10 nm Ni and 2 μm Al, on top before patterning. Figure 2.4b shows the same substrate after patterning a sol-gel layer on top using SCIL. The substrate is quite homogeneously coated; the different colors in the image are due to different interference contrast for different incident angles. Near the corners of the sample some inhomogeneities are observed which is due to the small size of the sample. Overall, except for some small defects, the entire substrate is covered with the imprinted resist layer.

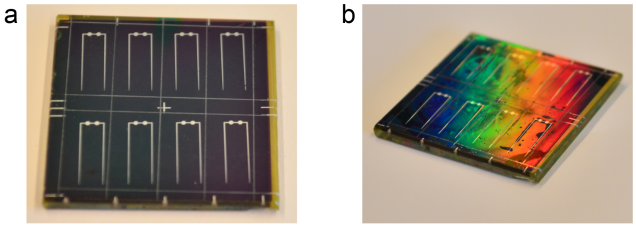

Figure 2.4: (a) Photograph of a 2.5 × 2.5 cm^2 CIGSe solar cell substrate, which is divided into 8 solar cells with have metal grids, consisting of 10 nm Ni and 2 μm Al, on top. **(b)** The same cell substrate after patterning a layer of sol-gel with holes using SCIL.

2.6 Conclusion

We have fabricated light trapping patterns for solar cells using SCIL. Arrays of metal and dielectric nanoparticles were made on top of different substrate materials by printing hole arrays using SCIL combined with RIE and using them as an evaporation mask. Patterned metal back contacts were made by patterning sol-gel layers on glass and subsequently sputter coating them with metal. We demonstrated the possibility of printing nanostructures on top of completed solar cells including 2 μm metal grids.

3

Optimized spatial correlations for broadband light trapping nanopatterns in high efficiency ultrathin-film a-Si:H solar cells

Nanophotonic structures have attracted attention for light trapping in solar cells with the potential to manage and direct light absorption on the nanoscale. While both randomly textured and nanophotonic structures have been investigated, the relationship between photocurrent and the spatial correlations of random or designed surfaces has been unclear. Here we systematically design pseudorandom arrays of nanostructures based on their power spectral density, and correlate the spatial frequencies with measured and simulated photocurrent. The integrated cell design consists of a patterned plasmonic back reflector and a nanostructured semiconductor top interface, which gives broadband and isotropic photocurrent enhancement.

3.1 Introduction

Thin and ultrathin-film solar cells are attractive candidates for low-cost replacement of thick, wafer-based devices. To achieve full absorption of the solar spectrum with ultrathin semiconductor volumes, light trapping is required over a broad spectral and angular range. To date, several light trapping geometries based on nanowires, nanocones, photonic crystals, nanoparticles, gratings, and

random textures have been demonstrated [20, 40–56]. While many researchers have demonstrated increased photocurrent due to scattering-mediated light trapping, the role of spatial correlations and surface topography of random or periodic arrangements of the scattering nanostructures has remained unclear. Here we identify the relation between these key parameters and the photocurrent spectrum for high efficiency, ultrathin (<100 nm thick absorber) film a-Si:H solar cells containing both integrated plasmonic and Mie scattering nanostructures. The nanostructure arrays described here are defined by their spatial coherence spectral density and are designed for broadband and isotropic response in ultrathin semiconductor volumes.

Ultrathin-film solar cells possess a number of advantages over their thicker counterparts. Ultrathin-films are less expensive due to the reduced cost of raw materials. For technologies based on scarce elements, such as CdTe and $CuIn_xGa_{1-x}Se_2$, a thickness reduction could expand scalability to the terawatt range [20, 57]. For thin-film Si cells, the use of ultrathin layers translates into faster manufacturing throughput, as overall cell production times are often limited by the chemical vapor deposition rate of the semiconductor film. For hydrogenated amorphous Si (a-Si:H) the use of ultrathin layers in addition strongly reduces the photodegradation that is commonly observed in thick cells due to the increased electric field across the ultrathin p-i-n junction [58, 59]. Moreover, for semiconductors that are not surface recombination limited, a reduction in semiconductor thickness leads to higher open-circuit voltages due to decreased bulk recombination [60]. While all of the above factors indicate that reducing semiconductor layer thickness is advantageous for the fabrication of inexpensive, stable, thin-film solar cells with high open circuit voltage, the major opposing requirement that limits the thickness is light absorption: to harvest the full solar spectrum the cell needs to be 'optically thick' for wavelengths up to the semiconductor bandgap.

Light-trapping nanostructures allow for nanoscale control of the direction and absorption of light in ultrathin-film solar cells, enabling new designs in which light is absorbed in semiconductor volumes much thinner than the optical absorption length. Indeed, an ultrathin-film solar cell can be considered as an optical integrated circuit in which light is received, guided, localized, and collected at the nanoscale. Inspired by optoelectronics, plasmonic nanostructures have recently attracted attention for light trapping in solar cells due to their large resonant scattering cross sections. Here we use plasmonic metal nanostructures integrated into the back contact of the solar cell to couple light into in-plane waveguide modes of the thin semiconductor layer, thereby increasing the path length and the short circuit current density (J_{sc}) [20, 56, 57]. The additional layers of the solar cell conformally coat the Ag back contact, producing a three-dimensional solar cell with a nanostructured top interface composed of Mie scatterers, leading to light trapping into localized modes near the surface as well.

Most light-trapping geometries studied, particularly for a-Si:H, are based

on random scattering structures with the geometry determined by the random nature of a deposition, growth, or etch process rather than by design. This is due to the fact that no suitable techniques were available that enable the controlled fabrication of engineered random scattering arrays at low cost. Recently, soft imprint lithography has been introduced as a technique that enables large-area, inexpensive fabrication of arrays of nanoscatterers [61–64]. We have shown that periodic arrays made using this technique show enhanced photocurrents in ultrathin-film a-Si:H solar cells over a narrow spectral range [46]. This new technique now also enables the design and fabrication of engineered random arrays with the spatial frequencies in the array pattern optimized for trapping a broad solar spectral band that is otherwise poorly absorbed. In this chapter, we systematically design and fabricate periodic and random arrays of nanoscatterers integrated in the back contact of an a-Si:H solar cell. By tailoring the spatial frequencies and obtaining an integrated understanding of both the localized and propagating modes resulting from plasmonic and Mie scattering in the three-dimensional structure, we are able to demonstrate an extremely thin cell with broadband photocurrent enhancement in both the blue and the red portions of the spectrum.

3.2 Methods

The fabrication process utilizes Substrate Conformal Imprint Lithography (SCIL), a wafer-scale nanoimprint lithography process to inexpensively replicate high fidelity, large area nanopatterns into silica sol-gel resist, which has been described in detail elsewhere [46, 61–64]. An initial large-area master substrate was patterned using electron-beam lithography on a Si wafer. The master substrate consists of 84 patterned regions containing one of 12 nanopatterns, tiled with repetition and rotation to control for deposition inhomogeneities, where each pattern covers a 6 mm × 6 mm area and the total master area is 10 cm × 3.6 cm. A bilayer stamp was molded from the master, consisting of a thin high-modulus polydimethylsiloxane (PDMS) layer holding the nanopatterns and a low-modulus PDMS layer to bond the rubber to a 200 μm thick glass support for in-plane stiffness. The stamp was used to emboss a 100 nm thick layer of silica sol-gel on AF45 glass substrates using SCIL. The sol-gel layer solidifies at room temperature by forming a silica network, while reaction products diffuse into the rubber stamp. After stamp release the sol-gel was post cured at 200 °C.

A thirteenth nanopattern is a reference pattern replicated from Asahi U-type texture. The texture is formed via a second stamp molded from an Asahi U-type reference substrate, and the texture transferred into sol-gel resist for use as a reference [63, 64]. Atomic force microscopy (AFM) comparison of the original and replica Asahi textures are in good agreement. We use a stamp transferred random texture rather than the original Asahi U-type glass substrate as both

the reference and the designed nanopatterns are later coated in Ag to form the back contact, and it is more appropriate to coat identical materials. Although there are examples of other highly performing, randomly deposited growth substrates available in the literature, we use Asahi U-type texture as a reference not because it is the optimal texture but because it is a commercially available and state of the art laboratory standard [52].

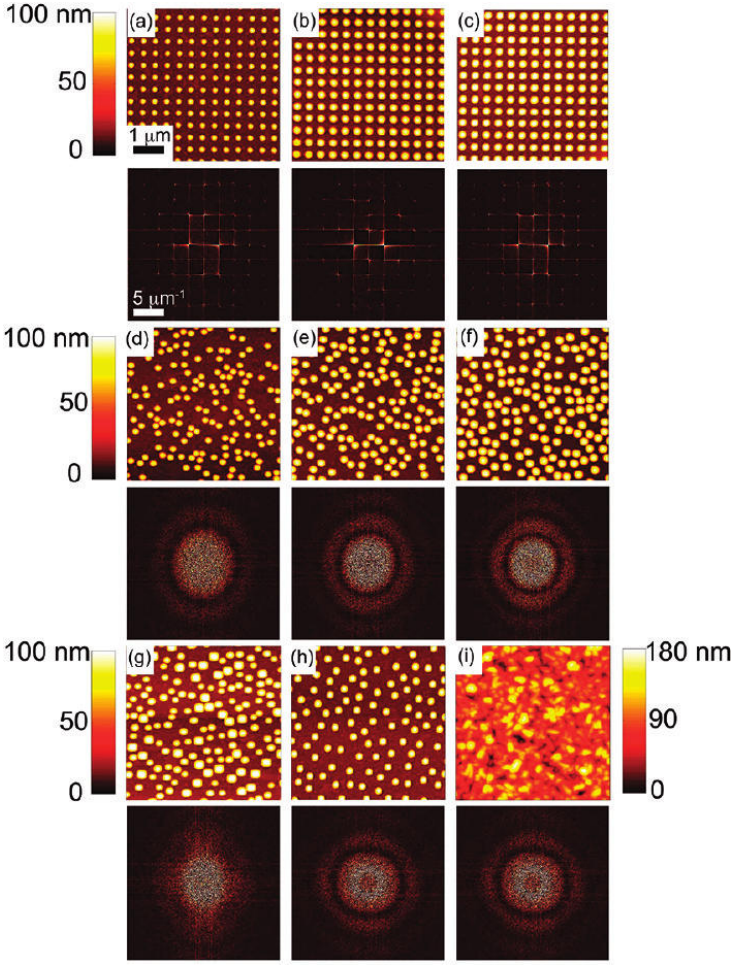

Figure 3.1: Metal nanopatterns used as light trapping surfaces. Four general classes of nanopatterns were fabricated on the substrate: **(a-c)** periodic arrays of nanoparticles with different diameters, **(b-g)** pseudorandom lattices of nanoparticles with controlled shape and packing density, **(h)** Penrose lattice of nanoparticles, and **(i)** nanoimprint replicated Asahi U-type glass. AFM images are taken of the Ag-coated silica sol-gel imprints; the corresponding Fourier transforms are shown below.

The 13 nanopatterns chosen fall into a few categories: flat, periodic (square lattices of 400 and 500 nm pitch), pseudorandom (with controlled nanoparticle size), quasicrystal (Penrose pattern), and randomly textured (Asahi replica). Both the Asahi reference and the designed nanopattern imprinted silica sol-gel surfaces are overcoated with Ag via sputtering to form the metallic back contact. The designed individual nanostructures consist of rounded plasmonic hemiellipsoidal nanostructures after Ag coating. Figure 3.1 shows AFM images of representatives of the Ag-coated patterns, along with their two-dimensional Fourier transforms. The nanoparticle sizes and shape are seen to be uniform across the substrate. Three sizes of nanoparticles were used in separate patterns, denoted small, medium, and large, corresponding to 200, 290, and 310 nm diameter, respectively. For the pseudorandom patterns, each pattern was uniquely generated with the constraints that the Ag particles do not touch after overcoating, and that the packing fraction is the same as for the 400 nm periodic pattern. The three different pseudorandom patterns differ in the diameter of the nanoparticles, which in turn sets a minimum separation between particles due to the nonoverlapping constraint. A more detailed discussion of the pattern-generation procedure is included in the Supporting Information (Section 3.5). As discussed later, the rounded metal nanostructures are advantageous, as they avoid the high parasitic absorption associated with sharp metallic features and they allow for conformal growth of the a-Si:H to produce both front and back textures. The diameters and pitch of the periodic nanopatterns were chosen based on electromagnetic simulations that account for the conformal deposition of all the cell layers over the patterns. The top indium tin oxide (ITO) surface of the cell shows a pattern of nanodomes as a result of the conformal depositions over the Ag back contact, and the best performance is predicted for Ag diameters and pitches such that the ITO nanostructures are at maximum packing density without overlap, as illustrated schematically in Figure 3.2a.

Cells were deposited over identical substrates with three different intrinsic layer thicknesses: 90, 115, and 150 nm. The cells consist of 100 nm of Ag coating the patterned silica sol-gel, 130 nm of ZnO:Al deposited by sputtering, n-i-p a-Si:H of varying i-layer thickness, 80 nm of ITO, and evaporated Au finger contacts. Device cross sections were made by a CO_2 laser along the backside of the cells, which lead to controlled splitting of the samples leading to clean cross sections. The cut samples were then imaged with scanning electron microscopy. Figure 3.2b shows a cross section through the cell illustrating the conformal nature of the growth. The top surface structure was also verified using AFM.

3.3 Results

Figure 3.2c shows current-voltage measurements on the cells with 90 nm intrinsic layers for some selected cell patterns. Device characterization was performed using a dual source WACOM solar simulator under one sun illumination

(AM1.5, 100 mW/cm^2). A table summarizing the results for each pattern for this thickness is shown in Figure 3.2d with the additional thicknesses and patterns described in Supporting Information Tables 3.1, 3.2, and 3.3. Over 1000 cells were measured in total for this study, and the tabulated data reports the highest efficiency measured for each pattern at each deposition run, with the average value of three cells on the substrate shown in parentheses. We estimate the error in the solar simulator to be ±3%, the variation in J_{sc} at 7%, the V_{oc} 3%, and the fill factor 5%.

(a)

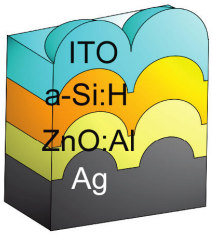

(b)

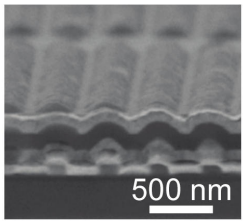

(c)

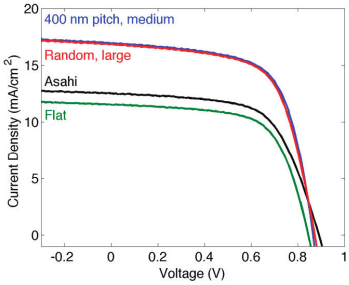

(d)

Pattern	Eff.(%)	J_{sc} (mA/cm^2)	V_{oc} (V)	FF
400/Medium	9.60 (*8.16*)	16.94 (*15.22*)	0.864 (*0.86*)	0.66 (*0.62*)
500/Medium	8.77 (*7.48*)	15.37 (*14.51*)	0.889 (*0.86*)	0.64 (*0.60*)
Random/Large	9.44 (*8.09*)	16.84 (*14.41*)	0.872 (*0.86*)	0.64 (*0.65*)
Random/Medium	9.35 (*7.73*)	16.18 (*14.82*)	0.888 (*0.87*)	0.65 (*0.58*)
Random/Small	7.27 (*6.58*)	14.22 (*12.76*)	0.835 (*0.84*)	0.61 (*0.62*)
Penrose	9.26 (*8.36*)	16.72 (*15.08*)	0.864 (*0.87*)	0.64 (*0.64*)
Flat	6.32 (*6.28*)	11.52 (*11.42*)	0.845 (*0.85*)	0.65 (*0.65*)
Asahi	6.94 (*6.69*)	12.52 (*12.93*)	0.890 (*0.83*)	0.62 (*0.62*)

Figure 3.2: Current-voltage characteristics of nanopatterned cells. The cells are conformally deposited over the patterned substrate, as shown schematically in **(a)** and in SEM cross section (5°angle) in **(b)**. The maximum particle diameter in the backpattern was chosen so that nanostructures in the ITO top layer would touch without overlap. **(c)** Current density-voltage measurements for the best-efficiency cells on the substrate with 90 nm intrinsic layers. The optimized periodic pattern and the pseudorandom pattern have efficiencies of 9.6 and 9.4%, respectively. **(d)** Electrical characteristics of highest-efficiency cells with average values shown in parentheses.

Several important trends are observed from comparison of the nanopatterns. The cells of 400 nm pitch have higher J_{sc} than those with 500 nm pitch. Cells

with large and medium diameter nanoparticles show higher currents than those with small nanoparticles. The highest efficiency (9.4–9.6%) for the thinnest ultrathin layers is observed for the 400 nm pitch pattern with medium particles and the random pattern with large particles. These two patterns consistently perform well at other intrinsic layer thicknesses. These efficiencies are among the highest measured for nanostructured a-Si:H solar cells and are especially notable given the very small (90 nm) intrinsic layer thickness.

External quantum efficiency (EQE) measurements for representative cells with a 90 nm intrinsic a-Si/H layer are shown in Figure 3.3a, and results for full-field three-dimensional electromagnetic simulations for similar structures in Figure 3.3b. EQE measurements were performed using monochromatic light from a Xenon lamp with one sun light bias applied. All of the textured and nanopatterned devices show enhanced photocurrent on the red side of the spectrum. Notably the photocurrent of the 400 nm pitch cell is also enhanced on the blue side of the spectrum [43, 48, 49, 65]. On the red side of the band, there are several sharp peaks in the periodic nanopatterns that are correlated with pitch. It was previously shown by Ferry et al. these features are due to waveguide modes with high overlap with the a-Si:H. In these cells, the ZnO:Al layer acts not only as a diffusion buffer layer between a-Si:H and Ag but also optically separates the a-Si:H waveguide modes from the lossy surface plasmon polariton modes on the metallic interface [46, 66].

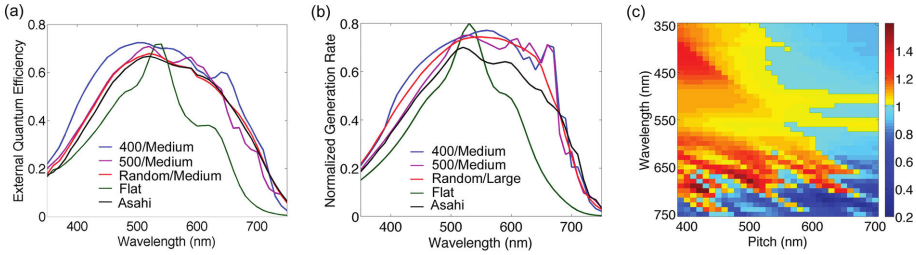

Figure 3.3: External quantum efficiency measurements and simulations. **(a)** External quantum efficiency measurements for several different patterns with 90 nm intrinsic layer thickness. **(b)** Simulated absorption for the same nanopatterns as in **(a)**. **(c)** Electromagnetic simulations of absorption enhancement as a function of pitch for cells with 115 nm intrinsic layer thickness. The color scale indicates the absorption enhancement compared to a simulated Asahi cell of the same thickness.

We also note that the value of J_{sc} obtained from integrating the EQE spectra against the AM1.5 solar spectrum is lower than the values reported in Figure 3.2d. This is a well-known issue in measuring solar cells and may be due to many different effects. In general, spectral mismatch between the EQE source and the solar simulator can cause a discrepancy between the two measurements, underestimating the current from the EQE spectra. Also, the EQE spectra shown are representative of the different patterns rather than the best devices

and were measured before additional annealing steps that improved the cell performance. Furthermore, these cells are sensitive to the angle of incidence of illumination, and perform better at off-normal incidence (discussed later in the text). The solar simulator, used for the IV-measurements, has a slight angular distribution, which will give different values for the current.

The experimental trends correspond well with those predicted from simulation, including the strong enhancement in the blue portion of the spectrum. The simulation details are given in the Supporting Information (Chapter 3.5). Given that the electromagnetic simulation technique accounts only for optical absorption and not carrier collection, the observed increase on the blue side is likely due to light trapping and not differences in the p-layer thickness or deposition. Figure 3.3c shows the calculated absorption enhancement as a function of pitch from 400–700 nm for periodic arrays with d_{Ag} = 300 nm and d_{ITO} = 400 nm (thus limiting the pitch to 400 nm to avoid overlapping nanodomes). The color scale shows the absorption enhancement relative to a simulated Asahi cell. On the red side of the spectrum, we observe branches due to coupling to waveguide modes as discussed previously with the resonant peaks shifting with pitch. On the blue side of the spectrum, there is a broad range of absorption enhancement that cuts off sharply at wavelengths shorter than the pitch.

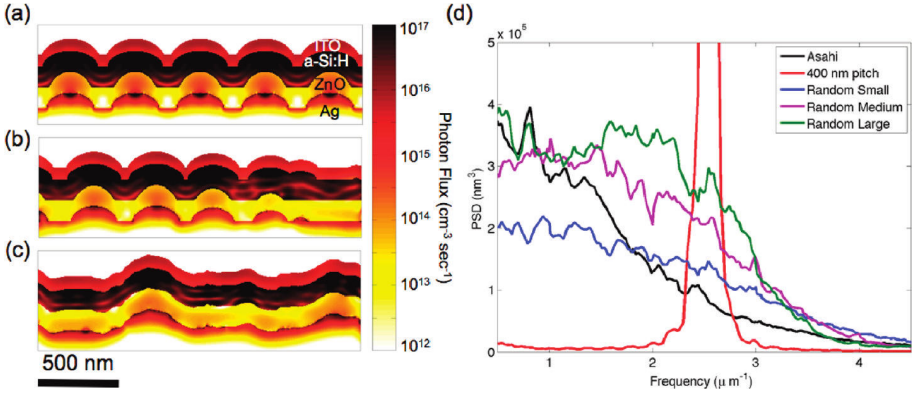

Figure 3.4: Pseudorandom and randomly textured patterns. **(a)** Photon flux in all layers of the solar cell calculated from electromagnetic simulation for cells with a 400 nm pitch periodic array, **(b)** simulation for pseudorandom particle array, **(c)** simulation for Asahi U-type texture. **(d)** One-dimensional power spectral density calculations based on AFM data from Figure 3.1.The 400 nm pitch and pseudorandom patterns with large particles have the highest power through the range of spatial frequencies required for coupling to waveguide modes in the a-Si/H in the 600–700 nm spectral band.

At wavelengths where the absorption length in a-Si:H is shorter than the scatterer separation, the absorption is mostly due to localized modes. Figure 3.4a-c shows photon flux, defined by $\Phi(\lambda) = \frac{1}{2\hbar}\epsilon''|E|^2$, cross sections from simulation for the periodic and pseudorandom patterns at λ = 500 nm.

The absorption is largely confined over each scatterer, as can be seen by the similarities in the absorption over the a-Si/H. Of course only the absorption in the a-Si/H contributes to photocurrent, but the images in Figure 3.4a-c also show the losses in the other layers, indicating that the ITO is a significant source of parasitic absorption. Figure 3.4a-c also illustrates the importance of nanostructure curvature. Plasmonic nanostructures with high frequency shapes (i.e., sharp points) are highly absorbing, leading to parasitic absorption in the metal layer (Figure 3.4c). In contrast, both the periodic and pseudorandom designed nanoarrays control the nanoparticle shape to include only rounded, curved scatterers (Figure 3.4a,b).

When the absorption length in a-Si:H is longer than the separation between particles (for $\lambda > 600$ nm) the arrangement of the nanoparticles becomes more important and the incident sunlight will couple to propagating modes of the device. In the periodic case coupling only occurs for wavelengths where the pattern bridges the wavevector mismatch between incoming light and waveguide modes, leading to the photocurrent peaks in the EQE spectrum of Figure 3.3a. Similarly, the designed pseudorandom nanopatterns result in efficient coupling to waveguide modes, but now over a broader spectral range, leading to a smooth EQE spectrum.

To quantitatively understand the connection between the nanopatterns and the observed strong photocurrent enhancement, in particular for the pseudorandom patterns, we calculated the power spectral density (PSD) [67] of the patterned back contacts from the AFM data shown in Figure 3.1. The results are shown in Figure 3.4d. The periodic, 400 nm pitch pattern, unsurprisingly, has a very sharp band centered at 2.5 $\mu m^{-}1$ with a bandwidth due to the finite size of the AFM scan. The Asahi and pseudorandom nanopatterns are much broader and flatter in spatial frequency.

To realize coupling to waveguide modes over the broadest possible solar spectral range requires a pattern with flat PSD through the range of spatial frequencies required to couple to the waveguide modes of the a-Si:H and at the same time minimal scattering power in the nondesirable spectral ranges. Within this framework, we can now explain the observed trends in photocurrent and deduce essential design rules. First, we observe that the pseudorandom patterns have higher scattering power than the Asahi texture through the range of optical frequencies required (Figure 3.4d). Indeed, the cells with engineered random patterns show much better cell performance than the Asahi cells (Figures 3.2, 3.3). Second, the large nanoparticles have higher scattering power than the smaller nanoparticles, consistent with the better light trapping observed for larger particles in both the periodic and pseudorandom arrays. Third, the periodic array is too narrowband to act as an isotropic light trapping surface.

While the PSD argument explains many of the observations of light trapping on the red side of the spectrum, it does not explain the strong photocurrent enhancement on the blue side of the spectrum. Since the absorption length of a-Si/H is under 100 nm in the λ = 400–500 nm range, the enhanced photocurrent

on the blue side must be due to the nanostructuring on the top interface. From simulation, we attribute this to the ITO/a-Si:H hemispherical nanostructures acting as weakly coupled Mie resonators, such that incident sunlight is resonantly absorbed in the hemisphere [68] and forward scattered into the a-Si:H region. The effective interaction cross section of these scatterers is 3–4 times their geometrical area over a broad UV/blue spectral range and thus leads to enhanced incoupling of light at these wavelengths, for which light would otherwise be strongly reflected. This enhancement in the UV/blue is consistent with the simulation results shows in Figure 3.3c and the 400 nm pitch was chosen a priori from these simulations at it showed the highest solar spectrum integrated absorption.

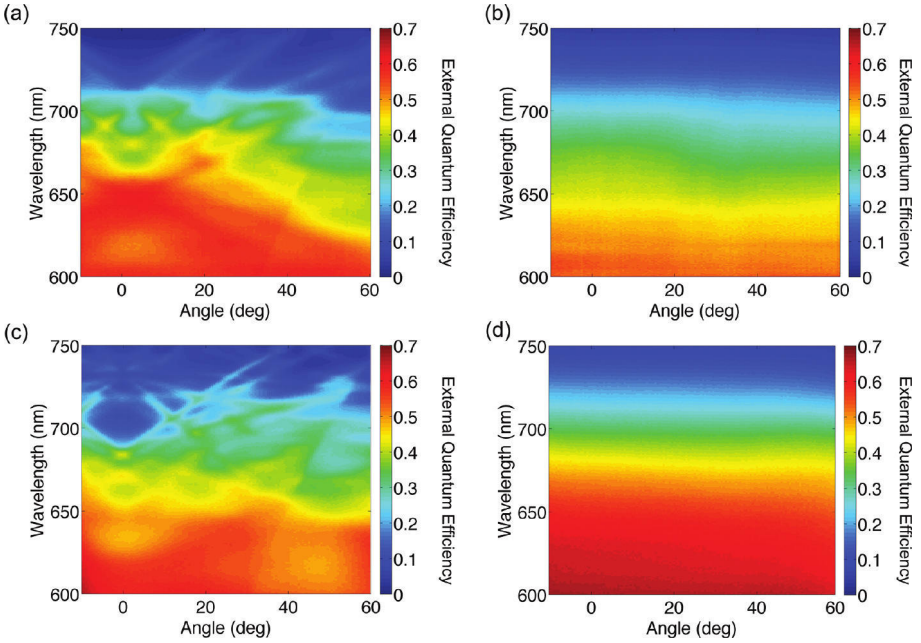

Figure 3.5: Experimental measurements of angle-resolved photocurrent on red side of spectrum. **(a)** A 400 nm pitch pattern on 90 nm cell. **(b)** Pseudorandom pattern with varying particle sizes on 90 nm thick cell. **(c)** A 400 nm pitch pattern on cell with 150 nm thickness. **(d)** Pseudorandom pattern with large particles on 150 nm thick cell. The periodically patterned cells show signatures of coupling to waveguide modes, while the pseudorandom nanopatterns show isotropic angular response.

Finally, we measured the angle-resolved EQE for the nanopatterned cells. Data are shown for 400 nm pitch and pseudorandom cells with a 90 nm (Figure 3.5a,b) and 150 nm (Figure 3.5c,d) intrinsic a-Si:H layer. The periodic cells show signatures of waveguide modes in the semiconductor, which shift with changing angle of incidence. We observe a higher number of mode branches

in Figure 3.5c than in Figure 3.5a, due to the higher mode density in the thicker a-Si:H layer. In contrast, the engineered random nanopatterns show an isotropic response with angle (Figure 3.5b,d). To achieve isotropic light trapping, a range of spatial frequencies must be present in the pattern to efficiently couple all angles into the localized and waveguide modes of the cell.

3.4 Conclusion

In summary, systematic study and design of pseudorandom arrays of resonantly scattering nanoparticles allow for both an understanding of the ideal random patterns for broadband, isotropic angular response, and the realization of high efficiency devices in extraordinarily thin semiconductor regions. Key to the design is an integrated understanding of spatial frequencies and curvature of nanoscale scatterers that form plasmonic backreflectors coupling to waveguide modes and weakly coupled surface Mie scatterers coupling to localized surface modes. While the diameters and pitch of the front and back surface patterns in this study were designed with a one-step, conformal deposition process in mind, it is possible that decoupling the pattern formation at the two interfaces will lead to higher overall efficiencies, extending the applicability to nonconformal semiconductor depositions. While focused here on a-Si:H, the principles presented here are potentially applicable to other solar cell materials systems.

3.5 Supplementary information

3.5.1 Generation of the pseudo-random patterns

Each pseudo-random pattern was first generated over a 100 μm x 100 μm area. The center points of the pattern were chosen randomly and assigned a diameter. For example, the 'random, medium' pattern was generated assuming a diameter of 250 nm Ag nanoparticles. Center points were chosen with a minimum separation of the diameter of the particle, constraining the pattern so that the Ag particles do not overlap. Points were chosen until the number of valid points was equal to the number of points contained in the same area with a 400 nm pitch of particles. The 'random, small' pattern assumed a diameter of 200 nm, and the 'random, large' pattern of 300 nm. The array was then stitched together to form a 6 mm × 6 mm pattern, with care taken on the edges of the stitching boundary to ensure that the same non-overlapping conditions and packing fractions held. The 'random, varying' pattern was generated using a mixture of the three different diameters, with each particle assigned a diameter before placement to check the overlap conditions.

3.5.2 Tables of best measured JV data for each pattern

Each patterned region on the master substrate was 6 mm × 6 mm in area. After deposition of the a-Si:H layer, an array of 4 mm × 4 mm squares of ITO was sputtered through a contact mask, and finger contacts were evaporated over the ITO using a second contact mask. The cell active area used for determining J_{sc} (0.13 cm^2) is the area of the ITO contact (0.16 cm^2) less the area of the Au contact grid, and was verified by optical microscopy.

While several copies of each cell pattern were made, the best efficiency values are tabulated here in addition to the average values in parentheses. Where patterns are missing, all of the cells of that pattern on the substrate were shunted. An analysis of the growth statistics is beyond the scope of this thesis.

Pattern	Eff.(%)	J_{sc} (mA/cm^2)	V_{oc} (V)	FF
400/Large	9.35 (8.68)	16.24 (15.97)	0.920 (0.87)	0.63 (0.63)
400/Medium	9.60 (8.16)	16.94 (15.22)	0.864 (0.86)	0.66 (0.62)
400/Small	8.87 (8.27)	16.10 (15.75)	0.865 (0.85)	0.64 (0.61)
500/Large	8.72 (8.47)	15.85 (15.13)	0.870 (0.88)	0.63 (0.64)
500/Medium	8.77 (7.48)	15.37 (14.51)	0.889 (0.86)	0.64 (0.60)
500/Small	8.66 (7.65)	14.60 (13.30)	0.897 (0.88)	0.66 (0.65)
Random/Large	9.44 (8.09)	16.84 (14.41)	0.872 (0.86)	0.64 (0.65)
Random/Medium	9.35 (7.73)	16.18 (14.82)	0.888 (0.87)	0.65 (0.58)
Random/Small	7.27 (6.58)	14.22 (12.76)	0.835 (0.84)	0.61 (0.62)
Random/Varying	8.88 (8.21)	16.68 (15.62)	0.855 (0.86)	0.62 (0.61)
Penrose	9.26 (8.36)	16.72 (15.08)	0.864 (0.87)	0.64 (0.64)
Flat	6.32 (6.28)	11.52 (11.42)	0.845 (0.85)	0.65 (0.65)
Asahi	6.94 (6.69)	12.52 (12.93)	0.890 (0.83)	0.62 (0.62)

Table 3.1: JV measurements on cells with 90 nm intrinsic layer thickness

3.5.3 EQE data for other thicknesses and repeatability

EQE measurements on the other thickness cells are shown in Figure 3.6. The 400 nm pitch cells in the 115 nm and 150 nm intrinsic layer thickness cells show blue side enhancement, the periodic cells show sharp features from the waveguide modes, and the pseudo-random patterns show a smooth response. Figure 3.6c shows the average EQE for the same pattern (400 nm pitch with large particles) on the three different thicknesses. The close overlap on the blue side of the spectrum indicate that the absorption here is independent of thickness (and limited by collection and parasitic ITO absorption). This is consistent with attributing blue side photocurrent enhancements to the top nanostructures.

Figure 3.7 shows the repeatability of the EQE data for different cells on the 115 nm thick cell substrate. Each trace is a different cell, and the colors match

Pattern	Eff.(%)	J_{sc} (mA/cm^2)	V_{oc} (V)	FF
400/Large	9.37 (8.16)	15.71 (15.59)	0.912 (0.85)	0.65 (0.61)
400/Small	5.91 (5.72)	13.66 (12.31)	0.833 (0.84)	0.52 (0.56)
500/Large	7.54 (6.82)	14.31 (13.56)	0.862 (0.82)	0.61 (0.61)
500/Medium	5.88 (5.82)	12.92 (12.58)	0.789 (0.78)	0.58 (0.59)
500/Small	5.75 (5.63)	12.26 (12.42)	0.782 (0.77)	0.60 (0.57)
Random/Large	7.49 (6.53)	14.93 (13.93)	0.834 (0.79)	0.60 (0.59)
Random/Medium	6.47 (5.09)	13.53 (13.47)	0.787 (0.75)	0.61 (0.50)
Random/Small	6.23 (5.89)	10.95 (11.68)	0.890 (0.84)	0.63 (0.60)
Random/Varying	8.06 (7.29)	15.90 (14.25)	0.832 (0.84)	0.61 (0.61)
Penrose	7.64 (7.57)	15.57 (15.53)	0.812 (0.81)	0.60 (0.60)
Flat	3.62 (3.47)	9.770 (9.06)	0.737 (0.74)	0.50 (0.52)

Table 3.2: JV measurements on cells with 115 nm intrinsic layer thickness

Pattern	Eff.(%)	J_{sc} (mA/cm^2)	V_{oc} (V)	FF
400/Large	7.38 (7.16)	14.94 (14.88)	0.755 (0.76)	0.65 (0.63)
400/Medium	9.48 (7.76)	16.57 (15.81)	0.854 (0.79)	0.67 (0.61)
400/Small	8.26 (7.28)	15.54 (14.66)	0.818 (0.80)	0.65 (0.62)
500/Large	8.44 (7.66)	15.54 (15.48)	0.829 (0.80)	0.66 (0.62)
500/Medium	7.99 (7.52)	16.22 (15.72)	0.797 (0.79)	0.62 (0.60)
500/Small	6.55 (6.27)	13.95 (13.75)	0.733 (0.74)	0.64 (0.61)
Random/Large	8.17 (7.94)	16.53 (16.08)	0.797 (0.80)	0.62 (0.62)
Random/Medium	7.42 (6.46)	15.99 (14.57)	0.787 (0.76)	0.59 (0.59)
Random/Small	6.90 (6.54)	14.68 (13.68)	0.764 (0.76)	0.61 (0.63)
Random/Varying	8.02 (6.65)	15.47 (14.48)	0.809 (0.77)	0.64 (0.59)
Penrose	7.44 (6.76)	15.69 (14.95)	0.783 (0.74)	0.60 (0.61)
Asahi	7.61 (7.43)	14.13 (13.96)	0.808 (0.81)	0.67 (0.66)

Table 3.3: JV measurements on cells with 150 nm intrinsic layer thickness

to different patterns. The peaks on the red side of the spectrum are clearly correlated with pitch, and the variations between cell measurements are small.

3.5.4 Analysis of the Penrose pattern

EQE measurements for the Penrose pattern are shown in Figure 3.8, with the simulated points overlaid. The Penrose tiling is not periodic, but has long-range order. The particles are the same size as the medium nanoparticles. The EQE spectrum appears to be an intermediate case between the periodic arrays and the pseudo-random arrays, with a few (repeatable) shoulders in the spectrum but much broader response than the periodic cells. Figure 3.9

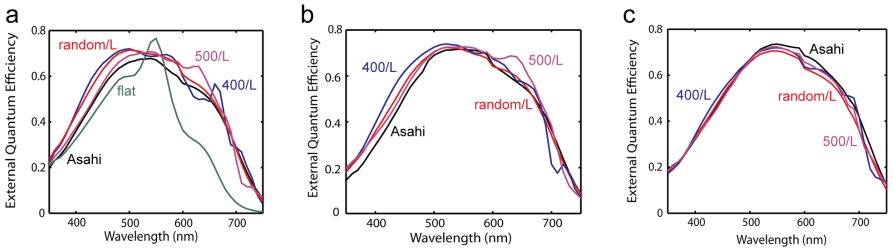

Figure 3.6: EQE data on representative cells from other deposition runs. **(a)** 115 nm intrinsic regions.**(b)** 150 nm intrinsic regions. **(c)** 400 nm pitch nanopatterns with medium particles from each deposition run.

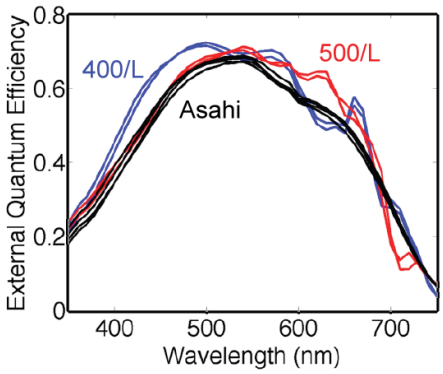

Figure 3.7: Repeatability of EQE data on cells with 115 nm thick intrinsic regions. Each color trace is a different device on the substrate.

shows the PSD spectrum for the Penrose pattern, generated from the AFM data, compared to a few of the other patterns. The Penrose cell has higher PSD than the Asahi pattern, is comparable to the random, medium pattern, and is lower than the random, large pattern. Notably, the pattern shows reduced PSD in the undesirable low frequency range. Unlike the other patterns discussed, the Penrose pattern does not have the same packing fraction; the scatterers are less dense than the pseudo-random or 400 nm pitch patterns. For the pseudo-random patterns, modification of the diameter and pitch resulted in a significantly higher PSD. Given this, we expect the PSD for the Penrose patterns could be tuned by modifying the diameter and spacing between the scatterers.

3.5.5 Details of simulation layout

Electromagnetic simulations were performed using Lumerical finite-difference time-domain software, with home written post-processing code. The refractive index of each layer was taken from ellipsometric measurements, with Ag

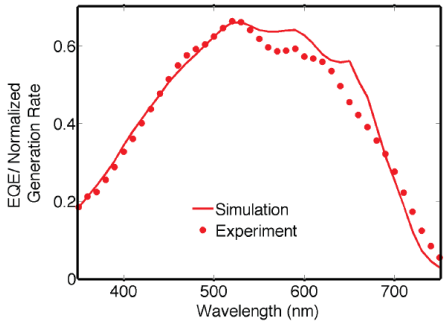

Figure 3.8: EQE spectrum for Penrose cell on 90 nm substrate, with overlaid simulation.

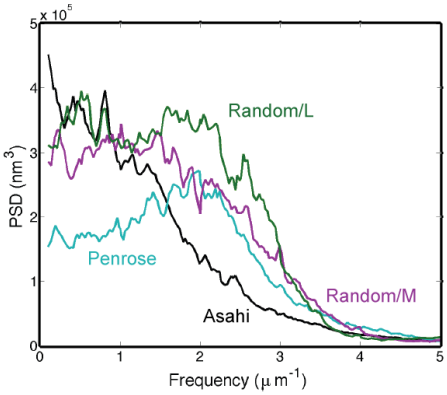

Figure 3.9: PSD spectrum for Penrose pattern compared to other pseudo-random patterns.

modeled by a Lorentz-Drude model. The simulations are performed at single wavelengths across the solar spectrum, and an index monitor map is used to separately calculate absorption in each of the layers, with only absorption in the a-Si:H contributing to the overall photocurrent. The simulations of Asahi texture were performed by feeding measured AFM data directly into the simulation, with a sufficiently large area to minimize boundary effects from the periodic edges. Simulations of the periodically nanopatterned cells assumed periodic boundary conditions, and approximated the aspect ratios and structures measured from cross sections. Simulations of pseudo-random patterns assumed the overcoating parameters of the periodic cells, with the simulation size of the Asahi textures.

4

Mode coupling by resonant surface scatterers in thin-film silicon solar cells

We demonstrate effective mode coupling by light scattering from periodic Ag nanoparticle arrays printed on top of a completed thin-film a-Si:H solar cell. Current-voltage measurements show a photocurrent enhancement of 10% compared to a flat reference cell with a standard antireflection coating. External quantum efficiency measurements for the nanopatterned cells show clear infrared photocurrent enhancement peaks, corresponding to coupling to discrete waveguide modes in the a-Si:H layer. The data are in good agreement with three-dimensional finite element simulations, which are used to further optimize the design. We show that broadband photocurrent enhancement can be obtained over the 450–750 nm spectral range. We find that using Al instead of Ag scattering patterns can further improve the cell's blue-response, by shifting the Fano effect to wavelengths below 400 nm. We show that arrays of TiO_2 particles at the front of ultra-thin a-Si:H cells result in efficient light trapping and a substantial antireflection effect and show absorption enhancements up to 46%. The use of TiO_2 scattering patterns leads to substantially lower absorption losses in the particles compared to Ag patterns.

4.1 Introduction

Thin-film solar cells offer the potential of high photovoltaic conversion efficiency combined with low fabrication costs and the possibility of a mechanically flexible design. The major disadvantage of thin-film cells over their thick counterparts is the relatively poor absorption of light, in particular in the infrared part of the solar spectrum. To overcome this problem, light trapping is required, in which light scattering structures are integrated within the solar cell to trap the light in multiple ways: The scattering leads to an angular redistribution of the light; in this way the path length of a single pass is enhanced and light at angles above the critical angle it is trapped by total internal reflection. Furthermore parallel momentum obtained in the scattering process can be used to couple to in-plane waveguide modes [20–22].

Metal nanoparticle arrays have been proposed as efficient light coupling and trapping coatings in thin-film solar cells. Metal nanoparticles are known to have high scattering cross sections near their plasmon resonance wavelength [25, 69], which can be tuned by varying the dielectric environment, and particle size or shape. Two main geometries have been considered. In the first, metal nanostructures are embedded in the metal back contact of the solar cell. The nanoparticle array then scatters light that is poorly absorbed in its first pass through the active layer of the cell into in-plane waveguide modes of the cell, thereby enhancing the light trapping [42, 44, 46]. In the second geometry, metal nanoparticles are placed at the front-surface of the cell. In that case they serve a dual purpose: they enhance the coupling of light into the cell by reducing reflection from the cell (anti-reflection effect) and they can enhance the path length in the cell (light trapping) [70–74].

So far, the anti-reflection effect, which is due to the preferential forward scattering from the plasmonic resonances, has been studied in detail [75, 76]. The light trapping effect for plasmonic surface coatings however, has not been well investigated. Here, we study the application of a Ag nanoparticle array on top of a completed solar cell that includes a dielectric antireflection coating. We find that the Ag nanoparticles scatter light into distinct waveguide modes of the solar cell, clearly enhancing the infrared response of the solar cell. Near-field enhancement does not play a role here, since the particles are separated from the cell by a 80 nm ITO layer. Numerical simulations show that the effect can be further enhanced by optimizing the Ag array geometry. Using numerical simulations we also study light trapping patterns consisting of Al nanoparticles and of TiO_2 nanoparticles. Our work is applicable to other solar cell materials and designs as well.

4.2 Methods

Thin-film hydrogenated amorphous silicon (a-Si:H) solar cells were used in this study. The fabrication of the solar cells was carried out as described by Soppe et al. [77]. Silica glass substrates were first sputter-coated with a 200 nm Ag layer followed by 80 nm ZnO buffer layer. The a-Si:H, with an intrinsic layer thickness of 350 nm, is grown in a *n-i-p* sequence using plasma enhanced chemical vapor deposition. 4×4 mm^2 pads of 80-nm-thick indium-tin-oxide (ITO) were then sputter-coated on top through a contact mask, to define the cell areas. The ITO serves as an antireflection coating as well. Finally, U-shaped Ag contacts are sputtered on top of the ITO, using a contact mask. The inset in Figure 4.1 shows a schematic cross section of the solar cell.

Metal nanoparticle arrays were printed on top of the completed cell using Substrate Conformal Imprint Lithography (SCIL). This technique enables inexpensive high-fidelity nanopatterning on large-area samples and is compatible with standard solar cell manufacturing techniques. SCIL uses a bilayer rubber stamp composed of a thin high-Young's-modulus polydimethylsiloxane (PDMS) layer that holds the nanostructures, laminated to a thick low-modulus-PDMS layer that gives the stamp flexibility [39].

In the imprint process, a layer of polymethylmethacrylate (PMMA) followed by a layer of silica-based sol-gel are spin-coated on the solar cell. Next, the rubber stamp is used to print an array of holes in the sol-gel. Anisotropic reactive ion etching (RIE) with a gas mixture of CHF_3 and Ar is then used to remove the thin residual sol-gel layer on the bottom of the holes. Subsequently, the holes are transferred into the PMMA using O_2 reactive ion etching. A 120 nm thick layer of Ag is then thermally evaporated on the sample. Finally, lift-off of the PMMA layer is performed in acetone so that an array of Ag particles remains. The inset of Figure 4.1 shows an SEM image of the particle array on the solar cell. The square array has a pitch of 500 nm and the particles have a radius and height of 120 nm. This image shows that metal nanoparticles can be accurately printed on top of a completed a-Si:H solar cell.

4.3 Results

Figure 4.1 shows the current-voltage (*I-V*) curves for both the patterned (red) and the reference cell (blue), which has the same device geometry as the patterned cell, but without nanoparticles. *I-V* curves are measured with a Wacom solar simulator under 1 sun illumination. Both cells have an open circuit voltage V_{oc} = 810 mV; the fill factors are also similar: FF = 0.60 and FF = 0.61 for the patterned and reference cells, respectively. This indicates that the SCIL imprint process is well compatible with solar cell manufacturing and does not lead to additional non-radiative recombination or cell shunting. The short-circuit current densities are J_{sc} = 13.7 mA/cm^2 and J_{sc} = 12.5 mA/cm^2, for the

patterned and reference cells respectively. The enhanced light coupling by the metal nanoparticle array thus leads to a 10% photocurrent enhancement. Note that this enhancement is observed beyond a reference cell that had an optimized ITO anti-reflection coating. Most other studies on metal nanoparticle enhanced light coupling do not use a cell with optimized anti-reflection coating as reference [78–81].

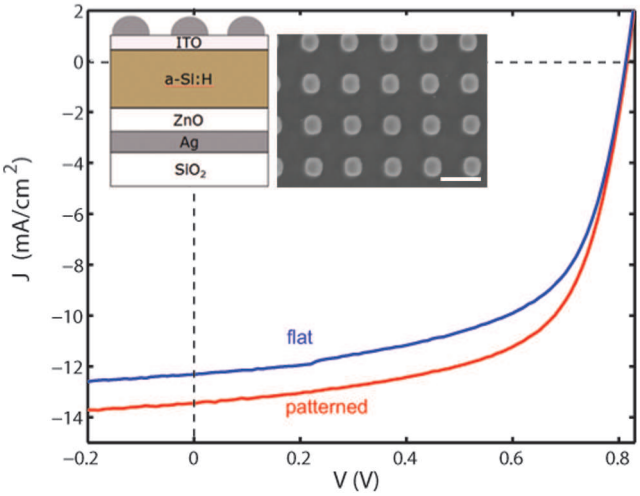

Figure 4.1: *I-V* curve for a Ag nanopatterned a-Si:H solar cell (500 nm pitch, 120 nm height, 120 nm radius, red) and a flat reference cell (blue). The insets show a schematic cross section of the layer structure and a top-view SEM image of the particle array (scale bar 500 nm).

Figure 4.2 shows external quantum efficiency (EQE) measurements of cells with (red) and without (blue) the Ag nanoparticle array. The EQE measurements were carried out on a commercial spectral response set-up by Optosolar (SR300) using a 250 W xenon lamp. Data are taken in 10 and 20 nm wavelength intervals for the patterned and reference cells respectively. The peaks observed in the $\lambda = 600$–800 nm spectral band are highly reproducible. For the flat cell, the spectral response is a smooth function of wavelength with the exception of the peak at $\lambda = 650$ nm, which is attributed to a Fabry-Perot effect in the a-Si:H layer. In contrast, the patterned cell shows multiple peaks in the near-infrared, at $\lambda = 660$ nm, $\lambda = 690$ nm, and $\lambda = 730$ nm. These are clear signatures of coupling to the waveguide modes as will be discussed below. While the metal nanoparticle array thus clearly enhances the spectral response in the infrared, it causes a reduced response in the blue spectral range, when compared to the reference. This is attributed to Ohmic dissipation in the metal particle on resonance and increased reflection below the particle resonance. The latter is due to the Fano effect: the destructive interference between the directly trans-

mitted beam and the forward scattered light at wavelengths below the plasmon resonance [42, 71, 72, 82].

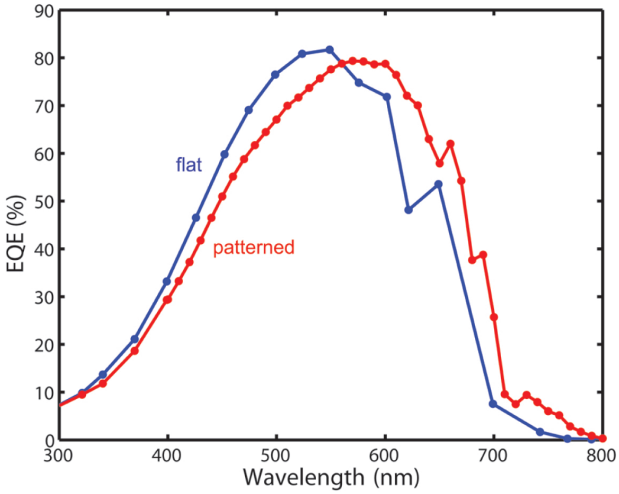

Figure 4.2: External quantum efficiency spectra for the patterned (red) and flat reference cell (blue).

Due to its high refractive index (n = 5.5–3.9 in the 350–800 nm spectral range) light is very well confined in the a-Si:H waveguide layer. Figure 4.3 shows the calculated dispersion relations for the lowest-order waveguide modes in the a-Si:H layer, taking into account all layers in the solar cell. In the wavelength range where light trapping is important ($\lambda > 550$ nm) the layer structure supports ten modes; five transverse electric (TE) and five transverse magnetic (TM) modes. The black diagonal line shows the light line in air. In this wavelength range the propagation length of the modes, defined by $L_p = \frac{1}{2\kappa}$, with κ the imaginary part of the mode's wavevector, is between 50 nm and 1 µm. All modes are located to the right of the light line, meaning that they are purely bound and cannot couple to free space radiation (light trapping). The vertical lines indicate the in-plane momentum provided by the grating orders as a result of the periodic nature of the Ag particle array. At wavelengths where the modes cross these grating lines, coupling is possible for light incident at normal incidence. The uncertainty in the modal wavevector due to absorption in the a-Si:H layer causes momentum matching to occur over a broader spectral range (not shown here).

Next, we compare the measured EQE peaks for the nanopatterned sample with the dispersion calculations. The horizontal lines in Figure 4.3 reflect the experimentally observed EQE peak wavelengths for the particle array from Figure 4.2. Clearly, the three observed peaks each correspond to distinct intersections of the dispersion curves with the grating vectors. The peak in EQE at

λ = 670 nm corresponds to [0,1] grating order coupling to the TM_4 mode, the [1,1] grating order coupling to the TE_4 mode, the [2,2] grating order coupling to the TM_1 mode, and the [0,3] grating order coupling to the TE_0 and TM_0 modes. The peaks at λ = 690 nm corresponds to the [1,2] grating order coupling to the TM_2 mode and the [0,3] grating order coupling to the TE_0 and TM_0 modes. Finally, the peak at λ = 730 nm corresponds to the [0,1] grating-order coupling to the TE_4 mode, the [0,2] grating order coupling to the TM_2 mode, and the [1,2] grating order coupling to the TE_2 mode. Note that not all crossings between modes and grating orders appear as clear peaks in the EQE measurement. We attribute this to the limited bandwidth of the measurement and, for shorter wavelengths, the fact that light is strongly absorbed in the a-Si:H, so that the effect of light trapping is smaller. Furthermore the coupling efficiency, which depends on the grating order, the field profile of the waveguide mode and the properties of the individual scatterer at each wavelength, is different for each crossing.

Three-dimensional finite-difference time-domain (FDTD) simulations, performed using Lumerical FDTD software, were used to model the absorption in the *i*-layer of the a-Si:H, taking into account the full layer structure. A unit cell with one cylindrical Ag particle is used in combination with periodic boundary conditions in x and y direction to simulate a periodic array. At the top and bottom of the simulation volume perfectly matched layers are used. Figure 4.4a shows the fraction of incident light that is absorbed in the intrinsic a-Si:H layer as a function of wavelength (continuous lines). Simulations are shown for a flat solar cell with 80 nm ITO (blue); the experimentally studied solar cell with a 500-nm-pitch array with 120-nm-radius and 120-nm-high particles (red). The simulations reflect the experimental trends in Figure 4.2 very well, with an absorption peak observed in the wavelength range λ = 550–600 nm, corresponding to the EQE peak in Figure 4.3. The coupling to waveguide modes for the patterned cell is clearly observed in the red part of the spectrum, leading to enhanced absorption in the a-Si:H layer. Peaks similar to the EQE peaks in Figure 4.2 are observed in the λ = 650–750 nm spectral range. The simulation also shows reduced absorption at wavelengths below λ = 600 nm, corresponding to the reduced EQE in Figure 4.3. Figure 4.4 shows that a purely optical model, neglecting wavelength-dependent carrier collection rates, can well predict trends in EQE.

Considering the good agreement between the FDTD simulations and the EQE measurements, we use FDTD simulations to further optimize the Ag nanoparticle array geometry. By reducing the particle diameter, the resonance blueshifts, which also leads to a blueshift of the destructive Fano interference at wavelengths below the resonance. The green continuous line in Figure 4.4a shows the absorption spectrum for a 450-nm pitch array with 80-nm-radius and 100-nm-high Ag particles. This array shows a clearly enhanced blue response compared to the experimental array and the flat cell while maintaining a high red response. Note that the peaks in the red have shifted as a consequence of changing the array pitch (and thus the in-plane momentum provided by the

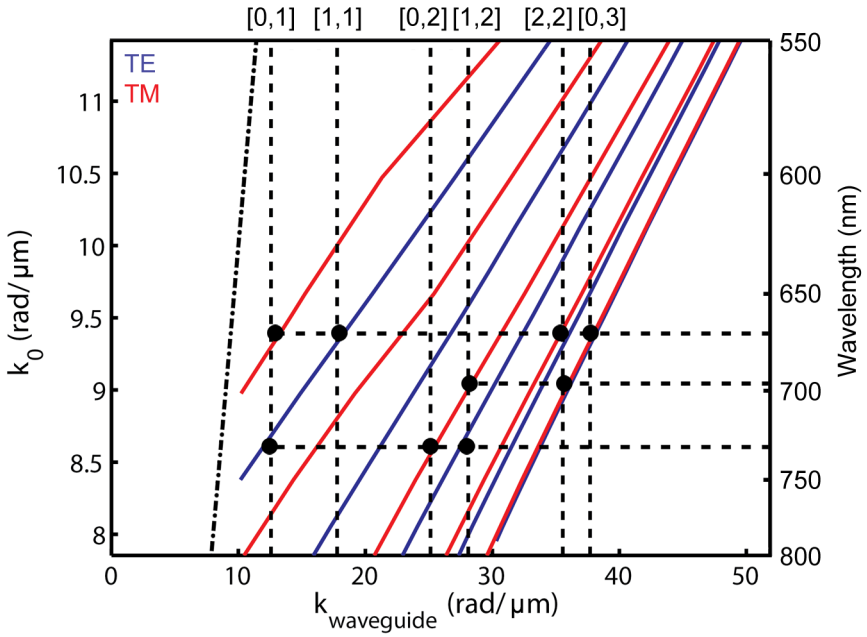

Figure 4.3: Dispersion relations for the TE (blue) and TM (red) waveguide modes in the 350-nm a-Si:H layer. The black dashed-dotted line is the light line in air. The vertical black dashed lines are the grating orders provided by the experimental particle array which has a pitch of 500 nm. At wavelengths where these lines cross the waveguide modes, light incident at normal incidence can couple to waveguide modes. The three horizontal black dashed lines show the incident wavelengths at which peaks appear in the EQE measurement of Figure 4.2.

grating orders). The dashed lines in Figure 4.4a show the calculated absorption in the metal nanoparticles. As can be seen, the particle plasmon resonance, which occurs at $\lambda = 530$ nm for the experimental sample, has shifted to $\lambda = 460$ nm for the optimized array.

Finally, Figure 4.4b shows the simulated reflectance for the flat (blue), experimental (red) and optimized (green) geometry. Using a nanoparticle array the reflectance is clearly reduced in the (infra-)red spectral range, due to the enhanced light trapping. Indeed, clear minima in reflection are observed at wavelengths where mode coupling occurs. For the experimental sample, reflectance in the blue spectral range is higher than for the flat sample, in agreement with the Fano interference argument mentioned above. The optimized array, however, has a reflection well below that of the flat sample over the entire spectral range from λ = 350–670 nm. In particular from λ = 410–670 nm, where the solar spectrum is intense, the reflection is well below 10%. The minima in reflection at $\lambda = 500$ and $\lambda = 450$ nm correspond to the Rayleigh anomalies for the 500 nm

and 450 nm pitch geometries, respectively.

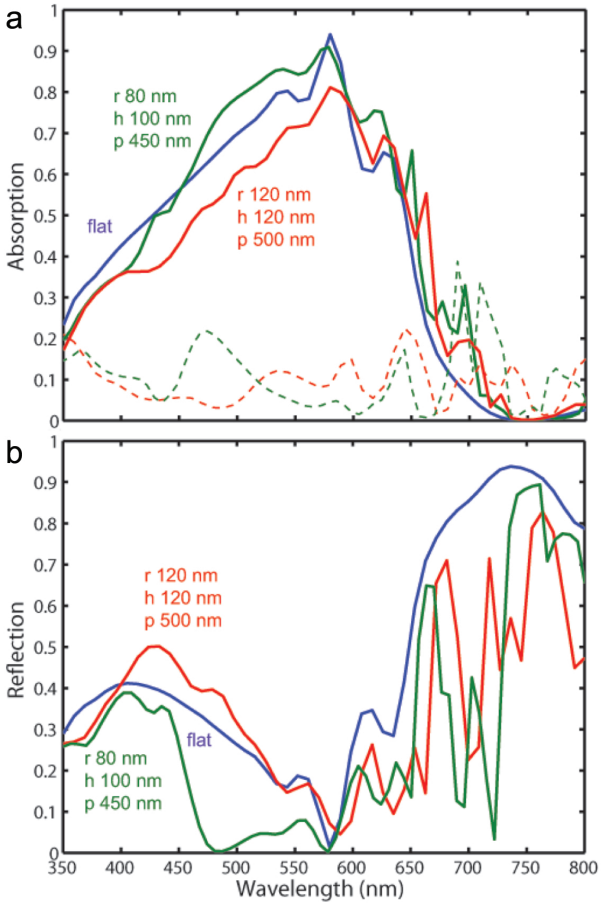

Figure 4.4: **(a)** Simulated absorption in the a-Si:H i-layer (continuous lines) and in the Ag nanoparticles (dashed lines). **(b)** Simulated reflection from the layer geometry. Data are shown for the experimental nanopatterned cell geometry (red), the flat reference cell (blue) and an optimized design (green).

4.4 Al versus Ag nanoparticles

As we have seen in Figure 4.4, to enhance both the red- and blue-response of these cells using Ag nanoparticles, the particles should not be too large. The best results are obtained with 450 nm pitch, 80 nm radius and 100 nm height. Making the particles larger results in a redshift of the particle resonance, which shifts the undesired Fano effect to wavelengths at which the solar spectrum

has higher intensity. Compared to Ag nanoparticles, Al nanoparticles have their plasmon resonance at lower wavelengths, which is due to the higher bulk plasma frequency of Al. Figure 4.5a shows the FDTD-simulated scattering cross sections for single Al and Ag cylinders on top of an ITO substrate. The scattering cross section spectrum for an Ag particle with radius 80 nm (green) shows two peaks: the first peak at a wavelength of 460 nm corresponds to the quadrupole resonance, and the second peak at 800 nm corresponds to the dipole resonance [76]. Increasing the particle radius to 100 nm (cyan) results in an overall larger scattering cross section, consistent with the larger geometrical cross section of the scatterer. The quadrupole resonance redshifts to 490 nm. This would lead to a Fano effect just below 490 nm, and hence a reduced blue-response. Furthermore, for the 100 nm Ag particle the dipole resonance shifts to a wavelength of 1000 nm, which is above the band gap for a-Si:H. Compared to the scattering spectra for Ag particles, the spectra for Al particles are blue shifted. For both particle sizes the quadrupole resonance is below 400 nm. The dip and peak at larger wavelengths that are observed clearly in the spectra of the Ag particles, are not very distinct in the scattering spectra of the Al particles. This is due an interband transition in Al around 800 nm, which causes a peak in absorption [83]. Overall, the Al particle with 100 nm radius has a large scattering cross section, and a quadrupole resonance below 400 nm. This is beneficial for light trapping patterns, since the Fano effect now shifts to wavelengths were the solar spectrum has low intensity.

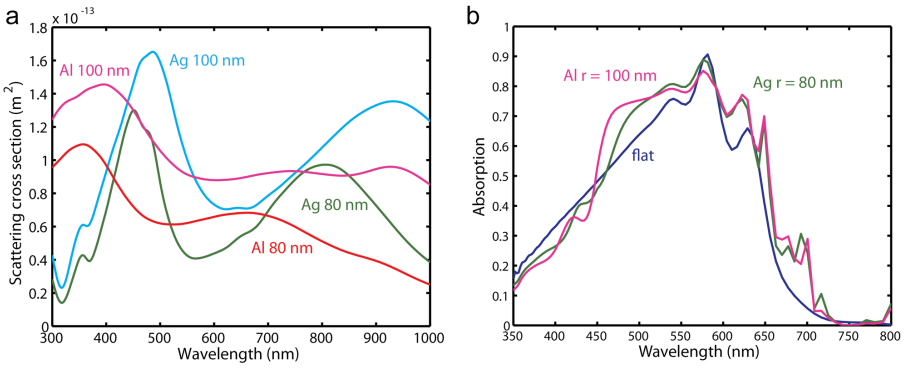

Figure 4.5: **(a)** Scattering cross sections for Ag particles with radius 80 nm (green) and 100 nm (cyan) and Al particles with radius 80 nm (red) and 100 nm (magenta) on ITO. All particles have a height of 100 nm. **(b)** Simulated absorption spectra for the same cell geometries as in Figure 4.4. Data are shown for a flat cell (blue) and cells with a periodic array of Al nanoparticles with radius 100 nm (magenta) and Ag nanoparticles with radius 80 nm. Both patterned geometries have an array pitch of 450 nm and particle height of 100 nm.

Figure 4.5d shows the FDTD simulated absorption in the same device geometry as Figure 4.4 with Ag particles with radius 80 nm (green) and Al nanopar-

ticles with radius 100 nm (magenta). Both arrays have a pitch of 450 nm and contain particles with a height of 100 nm. The Al particles perform substantially better than the Ag particles at wavelengths between 440 nm and 520 nm. At wavelengths below 400 nm the Al particles result in lower absorption than the Ag particles, which is due to the Fano effect. Some small differences in red response are observed when comparing the Al and Ag particle. We attribute this to their different scattering and absorption properties.

4.5 TiO_2 scattering patterns

Whereas metal nanoparticles efficiently scatter the light, they also absorb a substantial fraction of the incident spectrum. Instead, arrays of dielectric scatterers could be used at the front-side of the cell to achieve a photocurrent enhancement. Analogous to the plasmon resonance of metal particles, wavelength-sized dielectric particles exhibit geometrical resonances [25]. TiO_2 is a suitable material for these patterns, since it has a relatively high refractive index (2.2–2.5), and low absorption losses in the visible. Figure 4.6 shows the normalized scattering cross section for single TiO_2 cylinders with a height of 200 nm on ITO for particles with different radii. The scattering cross section for the particle with a radius of 100 nm (blue) shows a small peak at 320 nm, followed by a dip and a very broad peak between 400 and 800 nm. The maximum value for the normalized scattering cross section is 7.5. This shows that TiO_2 particles on ITO very efficiently scatter the light. Increasing the particle radius (green, red) results in a redshift of the spectra, and also in more complex scattering spectra. Larger particle radii result in larger scattering cross sections in the red spectral range, in which light trapping is required.

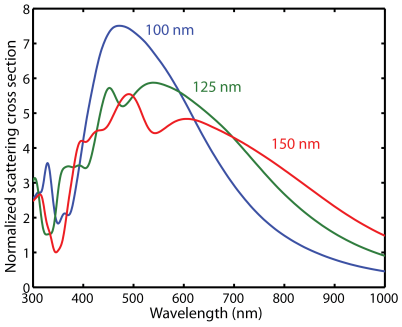

Figure 4.6: Normalized scattering cross section spectra for TiO_2 single cylinders on ITO with height 100 nm and radius 100 nm (blue), 125 nm (green), and 150 nm (red).

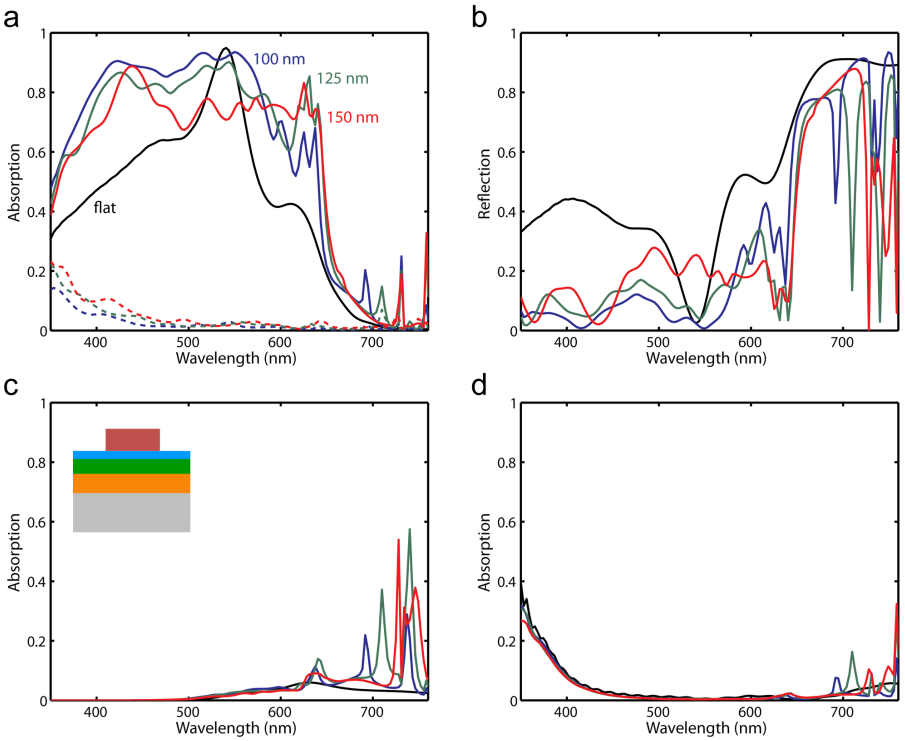

Figure 4.7: FDTD simulated absorption in the **(a)** a-Si:H layer, **(c)** Ag layer, and **(d)** ITO layer, and **(b)** reflection of a 145 nm a-Si:H solar cell with and without arrays of TiO_2 particles on top. Data are shown for a flat cell with 80 nm ITO (black) and cells with periodic arrays of TiO_2 particles on 40 nm ITO with height 200 nm, pitch 500 nm, and radius 100 nm (blue), 125 nm (green), and 150 nm (red). The inset shows a schematic cross section of the cell geometry, consisting of Ag (grey), AZO (orange), a-Si:H (green) and ITO (blue).

Figure 4.7 shows the FDTD simulated absorption in ultra-thin (145 nm) a-Si:H solar cells with periodic arrays of TiO_2 cylinders with different radii on top compared to unpatterned cells. The inset in Figure 4.7c shows a schematic cross section of the cell geometry, which consists of 200 nm Ag (grey), 130 nm AZO (orange), 145 nm a-Si:H (green), 40 nm ITO (blue), and TiO_2 particles (purple). The reference contains the standard ITO thickness of 80 nm. Figure 4.7a shows the absorption in the a-Si:H layer (continuous lines) and in the nanoparticles (dashed lines). The flat cell (black) has a very poor red-response, due to the small thicknesses of the absorber layer. Patterning the cell with periodic arrays of TiO_2 nanoparticles (green, blue red) leads to a broadband enhancement in absorption. A substantial anti-reflection effect is observed in the blue-spectral range, due to preferential scattering into the high-refractive index layer. This anti-reflection effect is dependent on the particle radius; in this spectral range

the 100 nm radius (blue) particle gives the largest enhancement. Distinct peaks are observed in the red-spectral range, which we attribute to waveguide mode coupling. The wavelengths of most of these peaks do not depend on the particle radius, while they do depend on the array pitch. The height of the peaks does depend on the particle radius. The wavelength of the peak around 700 nm that is observed for the 100 nm (blue) and 125 nm (green) particles depends on the particle radius; a redshift is observed with increasing particle radius. At wavelengths between 460 and 560 nm, the largest particles (150 nm) result in substantially lower absorption than the other particle sizes. Overall, the particle with 125 nm radius gives the largest integrated absorption enhancement. Absorption in the nanoparticles (dashed lines) is low and occurs mostly at wavelengths below 500 nm. Averaged over the AM1.5 spectrum, the absorption in the particles is 2–3%.

Figure 4.7b shows the simulated reflection for the same cell types. The patterned cells (blue, green, red) show a substantially lower reflection than the flat cell (black), both in the blue and red spectral range. The features observed in the absorption spectra (Figure 4.7a) for the different cell types are also present in the reflection spectra. At wavelengths between 680 nm and 760 nm sharp peaks are observed in absorption in the a-Si:H layer (Figure 4.7a); the reflection spectra show strong dips in this spectral range. The reflection for the geometry with the 150 nm radius particle (red) even goes to 0 at a wavelength of 730 nm. Nevertheless, all peaks in the absorption in the aSi:H layer (Figure 4.7a) are below 40% in this spectral range in which the a-Si:H layer weakly absorbs. At wavelengths where the sharp dips in reflection occur, peaks are also observed in absorption in the Ag (Figure 4.7c), ITO (Figure 4.7d) and AZO (not shown) layers. Particularly in the Ag layer absorption losses are high in this spectral range; peaks in absorption go up to 60%. Absorption losses in the ITO layer (Figure 4.7d) are largest at wavelengths below 450 nm and are only slightly enhanced upon patterning the cell. A taller peak occurs in the ITO-absorption spectrum at a wavelength of 760 nm for the 150 nm radius particle and amounts to 35% absorption.

Figure 4.8a shows the FDTD-simulated absorption in patterned cells with different ITO thicknesses compared to a flat cell with 80 nm ITO, which is the standard thickness of the ITO antireflection coating on a flat cell. All particle arrays have a pitch of 500 nm, particle radius of 125 nm, and height of 125 nm. Increasing the ITO thicknesses from 20 nm (cyan) to 80 nm (magenta) results in a redshift of the features in the red part of the absorption spectrum. The peaks between 730 and 760 nm are small for the geometries with 60 nm and 80 nm ITO. With the thicker ITO layers, the scatterers are further away from the waveguide, and the mode-coupling becomes less efficient. Furthermore the dip at wavelengths between 580 nm and 600 nm increases with increasing ITO thickness. Also in the blue spectral range the absorption spectra are highly dependent on the thickness of the ITO layer. Overall, an ITO layer with a thickness of 40 nm gives the largest absorption enhancement.

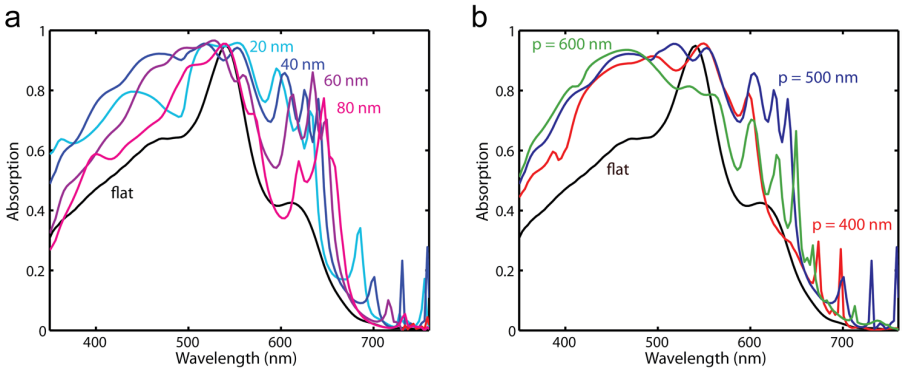

Figure 4.8: FDTD-simulated absorption in the a-Si:H layer for cells patterned with TiO_2 particles for **(a)** different ITO thicknesses and **(b)** different array pitches. The patterned cells have a particle radius and height of 125 nm. Data in **(a)** are shown for patterned cells with an array pitch of 500 nm and an ITO thickness of 20 nm (cyan), 40 nm (blue), 60 nm (purple), and 80 nm (magenta) and a flat cell with 80 nm ITO (black). Data in **(b)** are shown for cells with TiO_2 particles on 40 nm ITO and an array pitch of 400 nm (red), 500 nm (blue) and 600 nm (green) and a flat cell with 80 nm ITO (black).

Figure 4.8b shows the FDTD-simulated absorption in patterned cells for different array pitches. The particles have a radius of 125 nm, height of 125 nm and are on top of 40 nm ITO. The blue response shows some dependence on the array pitch. The mode-coupling in the red spectral range is highly dependent on the array pitch. The pattern with 500 nm pitch has the best red-response, which is mostly due to the broad peak between 600 and 670 nm. Overall, a pitch of 500 nm results in the largest absorption enhancement.

We further optimized the array geometry by varying the particle radius between 100 nm and 200 nm, height between 125 nm and 200 nm, pitch between 400 nm and 600 nm, and ITO thickness between 10 nm and 80 nm, exploring the full 4D parameter space. We found that the optimum geometry is the geometry shown in Figure 4.8a and b (blue). Averaged over the AM1.5 spectrum, the absorption enhancement amounts to 46%.

To further study the influence of the array configuration, we compare simulations of cells patterned with random and periodic particle arrays. Figure 4.9 compares the absorption in the a-Si:H layer of a periodically (red) and a randomly (cyan) patterned cell. The patterns both have particles with radius 125 nm, height 200 nm, and have an (average) array pitch of 500 nm. The random array was generated by placing particles in a $2 \times 2\ \mu m^2$ unit cell at x, y positions determined using a random number generator, with the restriction that particles are not allowed to overlap. Periodic boundary conditions were used in the simulation in x and y direction and also overlap over the periodic boundaries was not allowed. The inset in Figure 4.9 shows the used random array configuration.

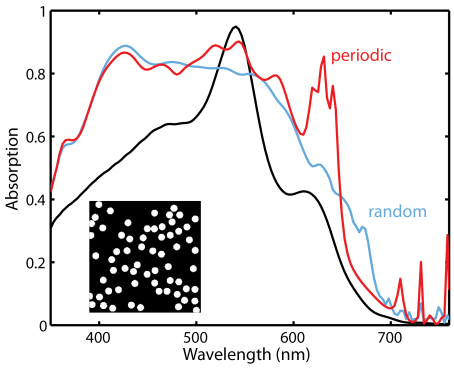

Figure 4.9: FDTD-simulated absorption in the a-Si:H layer of a flat (black), periodically patterned (red), and randomly patterned (cyan) cell. The inset shows the random array configuration in a 2×2 μm^2 unit cell.

Comparing the simulated absorption for the random (cyan) and the periodic (red) particle array shows they have a similar blue-response. This indicates that the antireflection effect mostly depends on the properties of the single scatter and the particle density rather than on the spatial frequencies in the scattering patterns. The red response however, is very different for the two different patterns. Whereas the periodic array shows very sharp peaks, the random pattern shows a broad enhancement without the sharp peaks. This is due to the difference in the spatial frequency distribution of these patterns. The periodic pattern only contains the spatial frequencies matching the array pitch and higher orders of this, and the random pattern contains a broad distribution of spatial frequencies at which mode-coupling is possible. Overall, for this light trapping geometry, the optimized periodic light trapping pattern outperforms the random pattern.

4.6 Conclusion

In conclusion, we fabricated a periodic array of Ag nanoparticles on top of a completed a-Si:H solar cell using substrate conformal imprint lithography. The addition of nanoparticles resulted in a 10% photocurrent enhancement with respect to the flat cell with a standard ITO antireflection coating. By comparing external quantum efficiency spectra and modal dispersion calculations, we demonstrate coupling of light scattered from the nanoparticles to distinct TE and TM waveguide modes in the a-Si:H, through second- and third-order grating coupling. The mode coupling is corroborated by three-dimensional FDTD simulations which show that further optimization of the array geometry can simultaneously optimize the red and blue response of the cell, leading to a broadband photocurrent enhancement. We find that the blue-response of the cell could be further enhanced when arrays of Al particles are used instead of

Ag particles, since this shifts the Fano effect to wavelengths below 400 nm. By patterning ultra-thin a-Si:H cells with arrays of TiO_2 particles, we show an absorption enhancement of 46% with respect to a flat cell. The patterned cell shows efficient light trapping as well as a substantial antireflection effect. By comparing periodic and random arrays with the same particle size and density we show that the antireflection effect mostly depends on the properties of the single scatterer, whereas the light trapping is strongly dependent on the spatial frequencies in the scattering pattern. Both Ag and TiO_2 nanoparticles efficiently scatter the light, but the advantage of using TiO_2 particles is that optical losses in the particles are only around 2% integrated over the solar spectrum, whereas optical losses in Ag nanoparticles are typically 10–15%.

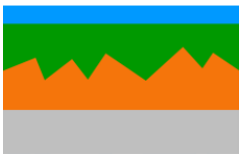

5

Dielectric backscattering patterns for light trapping in thin-film Si solar cells

We experimentally compare the light trapping efficiency of dielectric and metallic backscattering patterns in thin-film a-Si:H solar cells. We compare devices with randomly patterned Ag back contacts that are covered with either flat or patterned aluminum-doped ZnO (AZO) buffer layers and find the nanostructure at the AZO/a-Si:H interface is key to achieve efficient light trapping. Simulations show that purely dielectric scattering patterns with flat Ag and a patterned AZO/a-Si:H interface can outperform geometries in which the Ag is also patterned. The scattering from the dielectric patterns is due to geometrical Mie resonances in the AZO nanostructures. The optimized dielectric geometries avoid parasitic Ohmic losses due to plasmon resonances in the Ag, and open the way to a large number of new light trapping designs based on purely dielectric resonant light scattering.

5.1 Introduction

Thin-film solar cells, with absorber layer thicknesses ranging from a few hundred nanometers to a few microns, combine the advantages of relatively low fabrication cost with the possibility to realize mechanically flexible devices. However, the small absorber layer thickness leads to poor absorption of the infrared part of the solar spectrum, in particular in solar cells based on amorphous

and microcrystalline silicon thin-films due to the unfavourable charge carrier mobilities and lifetimes in these materials. To solve this problem, light trapping is required, in which nanostructures incorporated in the solar cell are designed to scatter the light and thereby enhance the optical path length. Many different periodic and random scattering geometries have been proposed in order to achieve efficient light trapping over a broad spectral range [20, 42, 44–48, 50–52, 71, 74, 84–92]. Several device designs make use of the efficient scattering properties of metallic nanoparticles, which have large scattering cross sections at their plasmon resonance [46, 71, 74, 84, 86–92].

Recently, it was shown that dielectric nanostructures on top of a solar cell can lead to strongly enhanced light incoupling due to forward scattering through resonantly excited Mie modes in the nanoparticles [23, 84]. Similar to plasmonic nanostructures, these dielectric surface nanostructures are very efficient resonant scatterers with scattering cross sections exceeding their geometrical cross sections [23, 25]. Moreover, dielectric scattering structures show much lower parasitic absorption than metallic nanostructures [91].

Many research groups have now demonstrated efficient broadband light trapping in thin-film devices grown on top of structured metal back contacts [46, 84, 91, 92]. In the case of thin-film Si solar cells, the metallic back contact is always separated from the absorber layer by an aluminium doped ZnO (AZO) layer, to avoid metal diffusion into the Si. Such a geometry is shown in Fig. 5.1a, which shows a cross-section made using focused ion beam (FIB) milling. Here, a randomly patterned glass substrate is covered with a thin Ag layer, on top of which subsequent layers of AZO, a-Si:H and indium-tin-oxide (ITO) are deposited. Due to conformal growth of the AZO layer on top the structured back contact, the AZO layer also contains the nanostructures. The solar cell is thus composed of random scattering patterns at both the Ag/AZO and the AZO/a-Si:H interface.

A natural question now arises if the light trapping in these solar cells is due to scattering from plasmon resonances in the Ag or from Mie resonances in the AZO nanostructures. Deciphering the effect of both scattering structures is important for a large number of thin-film solar cell designs. In this chapter we systematically study the influence of the structured AZO layer on light trapping in thin-film Si solar cells grown on top of a structured metal back contact.

We experimentally compare thin-film a-Si:H devices with structured Ag and either structured or flat AZO layers. We show that flattening the AZO buffer layer is detrimental for light trapping, demonstrating the key importance of dielectric scattering for light trapping even in plasmonic geometries. We study both random and periodic structures and demonstrate examples of purely dielectric scattering patterns.

5.2 Sample fabrication

The solar cell fabrication was performed as described by Soppe et al. [77]. Flat glass substrates and Asahi U-type substrates were sputter-coated with a 200 nm Ag layer and an AZO buffer layer. An a-Si:H layer (350 nm *i*-layer) was then grown using plasma-enhanced chemical vapour deposition (PECVD) in *n-i-p* configuration. To define the different cell areas 4×4 mm pads of ITO were sputtered on top of the a-Si:H layer using a contact mask. Finally U-shaped Ag contacts were sputtered on top through a contact mask.

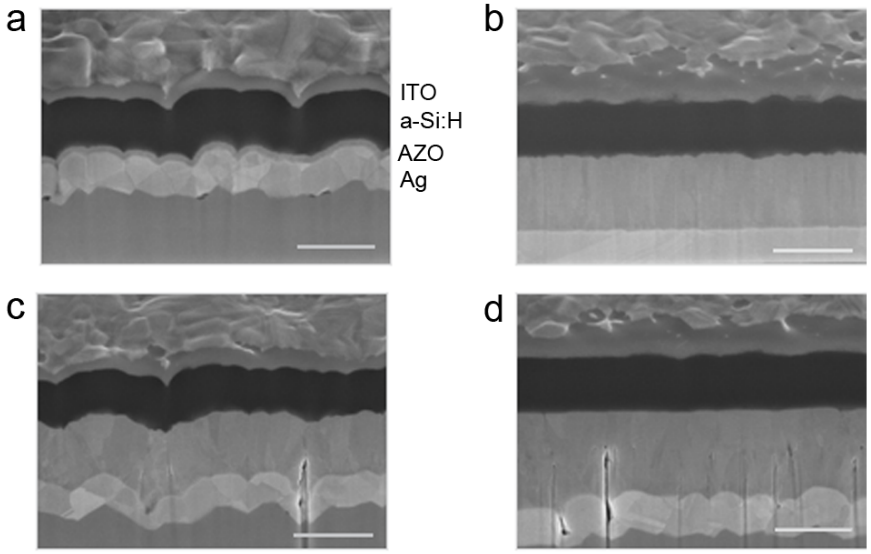

Figure 5.1: FIB cross sections of the different cell types: **(a)** Reference a-Si:H solar cell, composed of an Asahi U-type substrate covered with 200 nm Ag, 80 nm AZO, 350 nm a-Si:H and ITO. **(b-d)** Solar cells grown on top of: **(b)** a flat substrate, **(c)** Asahi substrate with 500 nm AZO, and **(d)** Asahi substrate with polished AZO. Scale bars: 500 nm.

Figure 5.1 shows cross sections, made using focused ion beam (FIB) milling, of the different types of cell geometries that were compared. Next to the 'standard' geometry shown in Fig. 5.1a, three complementary geometries were made. One cell type was grown on top of a flat glass substrate and has an AZO thickness of approximately 500 nm (Fig. 5.1b). One cell type was grown on top of an Asahi U-type substrate and also has a 500 nm AZO layer (Fig. 5.1c). This results in roughness in both the Ag/AZO layer and the AZO/a-Si:H interface. And one cell type was made by depositing AZO onto Asahi U-type substrate and then polishing the AZO surface using chemical mechanical polishing with colloidal SiO_2 slurry. This resulted in a sample with structured Ag/AZO interface and a flat AZO/a-Si:H interface (Fig. 5.1d). The use of a rather thick (500 nm) AZO

layer enabled polishing without exposing the Ag. A total of 24 cells were made of each type, so that electrical cell parameters could be averaged in the analysis. AFM data of Ag coated Asahi U-type substrates are shown in ref. [84].

5.3 Experimental results

Figure 5.2 shows current-voltage (I-V) measurements for the four different types of cells; curves are shown for single cells. I-V curves were measured under one-sun illumination using a WACOM solar simulator. Table 5.1 summarizes the average open circuit voltage (V_{oc}) and fill factor (FF) of the different cell types. From these measurements, no significant difference in V_{oc} and FF can be observed between the different types of cells, indicating similar electrical quality of the different device types. The curves were normalized to the current obtained from external quantum efficiency measurements at short circuit to exclude inaccuracies in the determination of the surface area of the cells. The flat cell (black) shows a photocurrent of J_{sc} = 10.7 mA/cm^2. The Asahi cells show significantly higher photocurrent. We find J_{sc} = 12.5 and 12.4 mA/cm^2 for the cells with 80 and 500 nm AZO, respectively (green, blue). The Asahi cell with polished AZO however (red), has a substantially lower photocurrent, than the normal Asahi cells: J_{sc} = 10.9 mA/cm^2. This indicates that the dielectric nanostructure at the AZO/a-Si:H interface is crucial for efficient light trapping.

Sample	V_{oc}(mV)	FF
Flat substrate	905 ± 7	0.68 ± 0.04
Asahi thin AZO	898 ± 15	0.66 ± 0.04
Asahi thick AZO	895 ± 16	0.64 ± 0.04
Asahi polished AZO	907 ± 12	0.69 ± 0.07

Table 5.1: Electrical properties of the four types of solar cells.

Figure 5.3a shows external quantum efficiency (EQE) measurements on the four different types of cells; measurements are shown for single cells. The EQE measurements were performed on a commercial spectral response set-up by Optosolar (SR300) using a 250 W xenon lamp equipped with a Jobin Yvon iHR320 monochromator. The diameter of the beam on the sample surface was 1 mm. The setup was calibrated with a crystalline silicon reference solar cell and the measurements were carried out with a spectral resolution of 10 nm.

The EQE for the flat solar cell (black) decreases rapidly above 550 nm, because of poor light absorption in this spectral range. The Asahi cells with structured AZO/a-Si:H interface (blue and green) show a significantly enhanced red-response with respect to the flat cell. This indicates that light trapping occurs due to the scattering nanostructures. In contrast, the Asahi cell with polished AZO shows barely any enhancement with respect to the flat cell. This shows

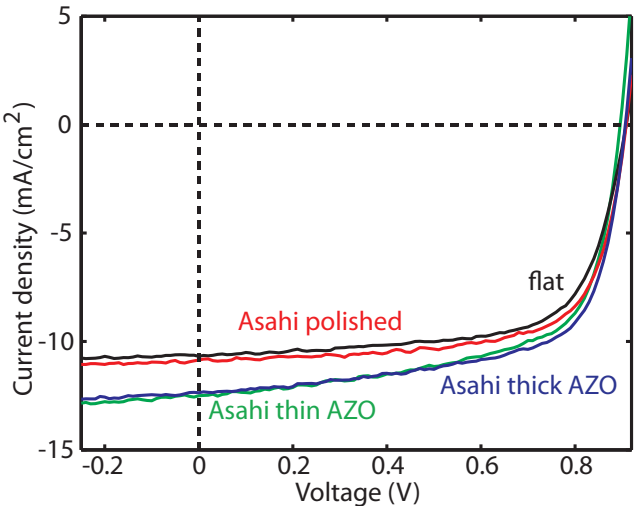

Figure 5.2: *I-V* curves for a-Si:H cells made on flat substrate (black), Asahi substrate with 500 nm AZO (blue), Asahi substrate with 80 nm AZO (green), and Asahi substrate with polished AZO (red).

that only structuring the Ag layer does not lead to any significant light trapping in this device geometry; i.e. the AZO/a-Si:H interface needs to be structured as well. All different types of cells show a similar highly reproducible blue response, indicating that roughness on the top, present because of conformal growth, does not play a role in the light management in these cells.

5.4 Simulations

Three-dimensional finite-difference time-domain (FDTD) simulations, performed using Lumerical software, were used to model the absorption in the a-Si:H layer. The simulations took into account the full layer structure: 200 nm Ag, 80/500 nm AZO, 350 nm a-Si:H, and 80 nm ITO. The Asahi roughness was incorporated by measuring the surface topography using atomic force microscopy (AFM) on an Asahi substrate that was sputter-coated with 200 nm Ag. The AFM data were then imported in the simulation to represent to topography of the Ag surface. In the case of the non-polished Asahi cells, the roughness of the AZO layer was assumed to be the same as the measured roughness of the Ag layer. Considering the similarity in the measured blue-response for the different types of cells with the flat and patterned AZO layers, the top of the a-Si:H layer and the ITO layer were assumed to be flat in the simulations. Periodic boundaries were used in x and y direction and a unit cell size of 2×2 μm^2 was used. No effects of periodicity were observed for this

size. A uniform mesh of 5 nm was used over the whole simulation volume. Perfectly matched layers were used at the top and bottom of the simulation volume. Three-dimensional absorption and refractive index monitors were used to determine the absorption per unit volume.

$$P_{\text{abs}} = \frac{1}{2}\omega\epsilon''|E|^2$$

where ω is the frequency, ϵ'' the imaginary part of the permittivity, and E is the electric field.

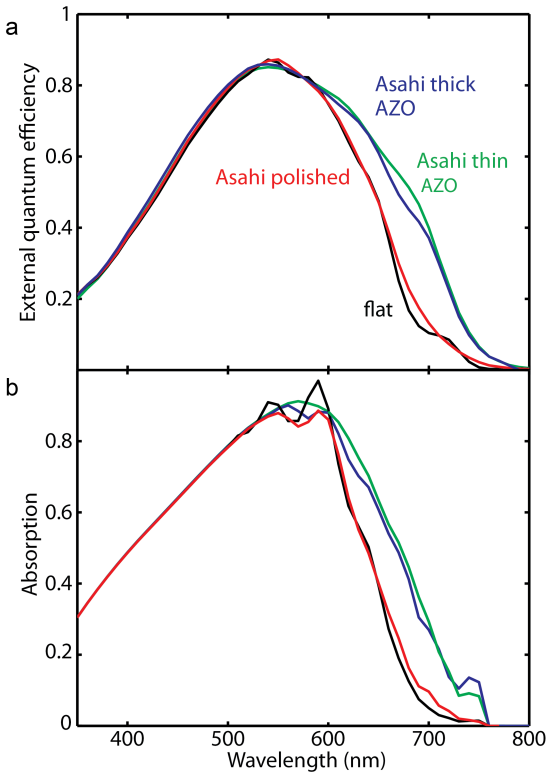

Figure 5.3: **(a)**External quantum efficiency measurements on solar cells on a flat substrate (black), Asahi substrates with 80 nm rough AZO (green), 500 nm rough AZO (blue), and 500 nm polished AZO (red). **(b)** Simulated absorption in the a-Si:H layer of the same cell types (line colours correspond to those in (a)).

Figure 5.3b shows the simulated fraction of incident light that is absorbed in the a-Si:H layer as a function of wavelength for the different types of cells. The simulations show very similar trends to the measured EQE data. The Asahi cells with patterned AZO (green and blue) show a significant absorption enhancement with respect to the flat cell (black) in the wavelength range above 600 nm,

whereas the sample with polished AZO (red) does not. We found that making the Ag rough results in significantly higher parasitic absorption. Whereas with flat Ag, the absorption in the Ag stays below 5% over the 350–800 nm wavelength range, the absorption in the rough Ag layer is up to 50% at wavelengths above 700 nm. Considering the good agreement between our FDTD simulations and EQE measurements, we used the FDTD simulations to study the influence of the AZO layer thickness on the absorption for devices with rough Ag and polished AZO.

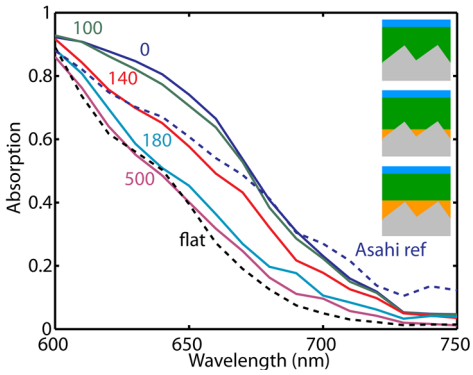

Figure 5.4: Simulated absorption in the a-Si:H layer of a solar cell without roughness (black dashed, 'flat'), with Asahi roughness in the Ag and AZO layer (blue, dashed, 'Asahi ref.'), and with Asahi roughness in the Ag and flat AZO (continuous) with a thickness of 0 nm (blue), 100 nm (green), 140 nm (red), 180 nm (light blue), and 500 nm (purple). The insets show cartoons of the different geometries with flat AZO (grey: Ag; orange: AZO; green: a-Si:H); no AZO (top), AZO thinner than Ag roughness (center), AZO thicker than Ag roughness (bottom).

Figure 5.4 shows the simulated absorption in the a-Si:H layer for different thicknesses of a flat AZO layer that is on top of the rough Ag. Data for a flat cell (black, dashed) and an Asahi cell with rough AZO (blue, dashed) are also shown as reference. When there is no AZO present (blue continuous, 0 nm), the rough Ag is directly in contact with the a-Si:H layer (first inset). As can be seen in the figure, this leads to efficient light trapping. At wavelengths between 600 and 680 nm, the absorption in the a-Si:H layer is even higher than for the Asahi reference (blue dashed), in which both the Ag and the AZO are rough. For the cell with flat AZO/a-Si:H interface the following trend is observed. When the AZO thickness increases to 100 nm (green), the AZO starts to fill up the valleys in the rough Ag (second inset); the areal fraction of Ag that is in direct contact with the a-Si:H rear interface is still high (72%). In this case, absorption in the a-Si:H slightly decreases with respect to the case where there is no AZO present. With 140 nm AZO (red), the fraction of Ag at the a-Si:H rear interface is only 27%, and absorption has decreased significantly. Further increasing the AZO

thickness to 180 nm (light blue), leads to reduced light trapping. At an AZO layer thickness of 500 nm (purple), only very slight light trapping is observed. The data in Fig. 5.4 show that roughness at the a-Si:H rear interface is required for efficient light trapping in this solar cell geometry.

To further investigate the loss and light trapping processes in the various geometries we have performed FDTD simulations on periodically patterned nanostructures. Such geometries are readily made using large-area inexpensive soft imprint techniques as we have demonstrated earlier [84]. Square arrays of hemispheres with a radius of 150 nm were used, using a 400 nm × 400 nm unit cell. Figure 5.5a shows the simulated absorption in the active layer of a-Si:H cells on top of periodic arrays of hemispheres in only the Ag (blue), both Ag and AZO (green) and only in the AZO (red), compared to a flat cell (black). These geometries are schematically depicted in Fig. 5.5b.

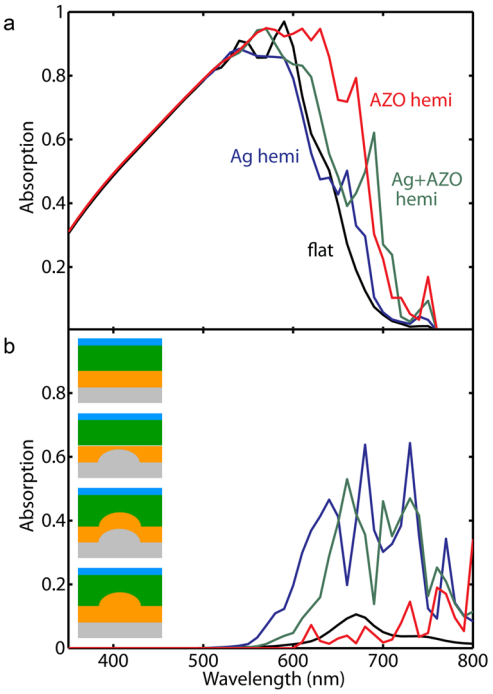

Figure 5.5: **(a)** Simulated absorption in the a-Si:H layer of solar cells with only flat layers (black), periodically structured Ag and flat AZO (blue, 'Ag hemi'), periodically structured Ag and AZO (green, 'Ag+AZO hemi'), flat Ag and periodically structured AZO (red, 'AZO hemi'). The insets show (from top to bottom): flat cell, cell with Ag hemispheres, cell with Ag and AZO hemispheres, cell with AZO hemispheres and flat Ag. **(b)** Simulated absorption in the Ag layer.

Figure 5.5a shows the simulated fraction of light absorbed in the a-Si:H layer

for the four geometries. The device with structured Ag and flat AZO shows poor light trapping. At wavelengths above 650 nm there is only a small enhancement in absorption with respect to the flat cell, while at wavelengths below 650 nm the Ag pattern results in a reduced absorption. When both the Ag and the AZO layer are periodically structured, a substantial amount of light trapping is observed. The device with flat Ag and patterned AZO shows even higher absorption than the cell with structured Ag and structured AZO. To study this further, we have simulated the fraction of light that is absorbed in the Ag for the different device structures (Fig. 5.5b). For structured Ag (blue and green) absorption in the Ag is significantly higher than for geometries with flat Ag (black and red), due to resonant scattering by the plasmonic nanostructures. The data in Fig. 5.5 show that light trapping using purely dielectric scattering patterns can be better than with combined dielectric-metallic scattering patterns, since it leads to lower parasitic absorption in the metal.

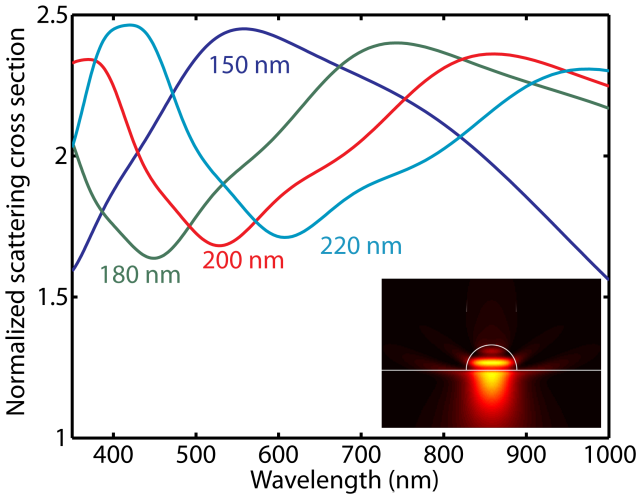

Figure 5.6: Simulated normalized scattering cross sections for AZO hemispheres on a non-absorbing AZO, inside non-absorbing a-Si:H, for radii of 150 nm (blue), 180 nm (green), 200 nm (red), 220 nm (light blue). The inside shows a cross section of the field intensity.

To study the scattering mechanism from the patterned AZO/a-Si:H interface, we consider the geometrical Mie resonances in the resonant cavities at the interface. Figure 5.6 shows the simulated normalized scattering cross sections, defined as the ratio between the scattering cross section and the geometrical cross section, for a geometry composed of an AZO substrate with a single AZO hemisphere embedded in a-Si:H layer (see inset in Fig. 5.6). Data are shown for hemisphere radii in the range 150–220 nm. A 2 μm × 2 μm simulation box was used with perfectly matched layers on all boundaries. A total-field-scattered-

field source was used to directly calculate the scattered power by means of frequency-domain transmission monitors positioned in the scattered field region. To allow propagation of the scattered field to the monitors, absorption in the a-Si:H layer and the AZO substrate were neglected (i.e. the imaginary parts of the refractive index were set to zero). The normalized scattering cross section for the hemisphere with 150 nm radius (blue, same size as in Fig. 5.5), shows a broad peak centred around 560 nm. The normalized scattering cross section exceeds unity over the entire 350–1000 nm spectral band, indicating strong interaction with the incident light. The inset shows the electric field intensity in the geometry with a 150 nm hemisphere, demonstrating the light is resonantly confined in the particle, with clear extension of the trapped resonant mode into the AZO and a-Si:H layers. We ascribe the large bandwidth of the resonance to the high loss rate associated with the enhanced leakage radiation to the AZO and a-Si:H layers. Figure 5.6 shows that when the particle radius is increased, the resonance shifts to higher wavelengths; further confirming the resonant Mie nature of the scattering mechanism. For the larger particles a second (higher-order) Mie resonance appears, in correspondence with the analytical Mie formulas for spherical particles. Simulated absorption for the full device geometry shows a strong size dependence; particles with a radius below 100 nm resulted in poor absorption enhancement. This indicates that geometrical resonances play an important role in the scattering process.

5.5 Conclusion

We have systematically compared dielectric and metallic scattering patterns for light trapping in thin Ag/AZO/a-Si:H solar cells. We experimentally demonstrate that geometries with patterned AZO buffer layers lead to substantially better light trapping than geometries with only patterned Ag. Simulations show that, if the AZO layer fills up the valleys of the rough Ag, this result is mostly independent of the AZO thickness and that structuring the AZO/a-Si:H interface is crucial for light trapping. We show that purely dielectric scattering patterns can outperform geometries in which the Ag is also structured by reducing the parasitic absorption that arises from plasmon resonances in nanostructured Ag. The light trapping with dielectric scattering patterns relies on geometrical resonances in the AZO nanostructures. Our work opens the way to a large number of new light trapping designs based on dielectric resonant light scattering.

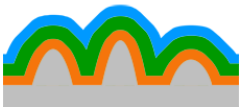

6

Efficient nanorod-based amorphous silicon solar cells with advanced light trapping

In this chapter we present a simple, low-cost and scalable approach for the fabrication of efficient nanorod-based solar cells. Templates with arrays of self-assembled ZnO nanorods with tunable morphology are synthesized by chemical bath deposition. The nanorod templates are conformally coated with hydrogenated amorphous silicon (a-Si:H) light absorber layers of 100 nm and 200 nm thickness. An initial efficiency of up to 8.4% is achieved. External quantum efficiency (EQE) measurements on the nanorod cells show a substantial photocurrent enhancement both in the red and the blue part of the solar spectrum. Three-dimensional finite-difference time-domain simulations agree well with the EQE measurements. Front surface patterns enhance the light incoupling in the blue while rear side patterns lead to enhanced light trapping in the red. The red response in the nanorod cells is limited by absorption in the patterned Ag back contact. We develop a further advanced design with patterned front and flat rear side, which will show even higher efficiency. Many of the findings in this work can serve to provide insights for further optimization of nanostructures for thin-film solar cells in a broad range of materials.

6.1 Introduction

Thin-film silicon is an attractive candidate in the photovoltaic (PV) market because of versatile deposition procedures, low manufacturing cost, and potential applications in flexible form. Among all the possible material structures of silicon, hydrogenated amorphous silicon (a-Si:H) is a very interesting material for single junction solar cells, as a top cell material for multiple junction solar cells such as the well-known 'Micromorph' concept [93, 94], and for a-Si:H/c-Si heterojunction cells with commercially viable efficiencies of >20% [95, 96]. However, a-Si:H in thin-film solar cells suffers from a high defect density which leads to a high recombination rate. Bulk recombination is mitigated by using thinner devices, which has also added advantages of increasing fabrication throughput and reducing light induced degradation. On the other hand, cells have to be thick enough in order to efficiently absorb the near-bandgap part of the solar spectrum. Therefore light-trapping schemes that increase optical absorption are crucial. Light scattering in thin-film solar cells is traditionally achieved by the usage of a textured transparent conductive oxide (TCO) layer, such as commercially available SnO_2:F with a randomly textured surface [97], or textured doped ZnO fabricated either by sputtering followed by a post-deposition hydrochloric acid etching [54, 98, 99] or by low pressure chemical vapor deposition [100]. The textured TCO layer scatters incident light into off-normal angles to increase the light propagation path in the absorber layer. Recently radial junction solar cells based on elongated nanostructures such as nanowires [40, 101, 102], nanorods [103–105], nanopillars [43, 106–108], nanodomes [42], and nanopyramid [109] have attracted intense attention.

At the present stage there are several challenges to the application of elongated nanostructures in solar cells [110]. One main challenge is the fabrication of large-area nanostructure arrays with controllable morphology in a cost-effective and high-throughput way. Methods such as reactive ion etching (RIE) and nanoimprint lithography that are used for the fabrication of well-defined patterns are difficult to scale up for large-area commercialization due to sample size limitations, and relatively high costs. Another main challenge is that the efficiency and the yield of these innovative solar cells based on elongated nanostructures so far are significantly lower than that for their conventional counterparts. To reach high efficiency, the very rough nanostructures must be conformally coated with device-quality absorber material, which requires smooth features. In contrast, a substrate with steep features is favorable for light scattering. So far, it has been difficult to reconcile these opposing requirements.

In previous work Kuang et al. reported the application of ZnO nanorods (NRs) prepared by a lithography-free, low-cost, and scalable approach to fabricate ultrathin a-Si:H nanostructured three-dimensional (nano-3D) solar cells [105, 111]. The nano-3D cells demonstrated a substantially enhanced photocurrent compared to flat devices as well as to randomly textured devices

with similar or even larger absorber layer thickness because of efficient light trapping. However, the nano-3D cells showed a significant reduction in open circuit voltage (V_{oc}), fill factor (FF), and yield. It was found that inhomogeneous coating of the applied layers on the nanorods, especially on the side walls, leads to the generation of voids or porous regions which are detrimental to the electrical properties. Incomplete coating of the NRs leads to shunting of the front and back contacts, which is detrimental to the FF. In this work, we have improved the morphology of the ZnO nanorod arrays by tuning the growth condition and optimized the configuration for solar cells. The new system reaches a good balance between the optical and electrical performance. We demonstrate efficient light trapping, indicated by the short-circuit current density (J_{sc}), and similar V_{oc} and FF as cells deposited on planar substrates. We measure the absorption, reflection and external quantum efficiency (EQE) spectra of the nanostructured cells and compare these to three-dimensional finite-difference time-domain (3D FDTD) simulations that are used to study the light trapping process in more detail.

6.2 Experimental

6.2.1 ZnO nanorod synthesis

Prior to the growth of ZnO NRs, a flat ZnO thin-film seed layer was deposited onto glass (Corning Eagle XG) at room temperature via radio frequency (RF) magnetron sputtering from a ceramic ZnO target. Zinc acetate dehydrate ($Zn(CH_3COO)_2{\cdot}2H_2O$, Sigma-Aldrich) with an equal molar ratio of hexamethylenetetramine (HMT, Sigma-Aldrich) was dissolved in de-ionized water to obtain a precursor solution, followed by magnetron stirring for ~15 minutes at room temperature. Synthesis of ZnO nanorods on the pre-coated glass was carried out at 80°C during a certain time, holding the seed layer side facing down in the precursor solution. The as-grown ZnO nanorods were characterized with scanning electron microscopy (SEM).

6.2.2 Solar cell fabrication and characterization

A ~200 nm thick silver layer was first deposited over the NR arrays via thermal evaporation, followed by a ~80 nm thick ZnO:Al (AZO) layer made by RF magnetron sputtering from a ZnO:2wt.%Al_2O_3 target. Deposition of an n_1-n_2-i-p (bottom to top) layer stack (nominal thickness: n_1: ~5 nm (μc-Si:H), n_2: ~25 nm (a-Si:H), i: ~100 or 200 nm (a-Si:H), p: ~15 nm (μc-Si:H)) was carried out by plasma-enhanced chemical vapor deposition (PECVD) using a radio frequency of 13.56 MHz in a multi-chamber deposition system. The deposition rate for the intrinsic layer was around 0.2 nm/s. SiH_4 was utilized for deposition of the a-Si:H n- and i-layers, while a SiH_4/H_2 mixture was employed for deposition of the μc-Si:H n- and p-layers. $B(CH_3)_3$ and PH_3 gases were additionally introduced

for p- and n-doping, respectively. The n-i-p stack on the NR arrays was sputter-coated with 4×4 mm^2 squares of indium tin oxide (ITO) (80 nm thick). Gold top-grid contacts were evaporated onto the square ITO pads, leaving an active cell area of 0.13 cm^2 for each cell. Planar solar cells on Corning Eagle XG glass were fabricated as reference, simultaneously with the structured ones. Current density-voltage (J-V) measurements were performed using a Wacom dual-beam solar simulator calibrated to the AM1.5G spectrum (100 mW/cm^2). To avoid carrier collection from outside the cell area, J-V measurements were performed with a thin stainless steel shadow mask with a 4×4 mm^2 opening. The EQE under short circuit condition was also investigated using a lamp in combination with a monochromator. Reflection and transmission spectra of the completed cells were measured by a Perkin Elmer Lambda 2S double-beam spectrophotometer equipped with an integrating sphere.

6.2.3 Finite-difference time-domain simulations

Three-dimensional finite-difference time-domain (FDTD) simulations, performed using Lumerical FDTD software, were used to model the absorption in the solar cells. The full device stack, consisting of 200 nm Ag, 80 nm ZnO, 100 or 200 nm intrinsic a-Si:H and 80 nm ITO in thickness, was used in the modeling. The thin n- and p-layers were neglected in the simulations. The roughness of the back of the device was implemented in the simulation by directly importing the surface topography of the Ag coated NR substrate measured by atomic force microscopy (AFM). The roughness profile at the AZO/a-Si:H interface was assumed to be the same as that at the Ag/AZO interface. AFM scans show that the topography at the ITO/air interface was significantly smoother compared to that of the Ag-coated NR substrates. In the simulations the surface profile (ITO/air interface) was generated by taking the AFM topography of the Ag coated substrate as a starting point and smoothing it by using a combination of image dilation and Gaussian blur in Matlab. Table 6.1 shows the root mean square (RMS) roughness of the AFM measured topography for the Ag-coated NR substrate and for the full NR/Ag/ZnO/a-Si:H/ITO layer stack. AFM topographies were measured over a 10×10 μm^2 area at five different positions on the sample. The RMS roughness of the top profiles that were generated by smoothing the measured Ag profiles is also shown in Table 6.1. The roughness profile at the a-Si:H/ITO interface was assumed to be the same as that at the ITO/air interface. In the simulations, a unit cell size of 2×2 μm^2 was used in combination with periodic boundary conditions. No effects of periodicity were observed for this size (no significant difference in absorption was observed when the simulation volume was increased to 2.2×2.2 μm^2). At the top and bottom of the simulation volume perfectly matched layers were used as boundary conditions. A uniform mesh of 5 nm was used over the whole 3D simulation volume.

	Ag coated NR substrate	Full stack (100 nm a-Si:H)	Full stack (200 nm a-Si:H)
Measured (nm)	81.3±1.8	58.2±5.2	47.6±2.7
Generated (nm)	–	56	49

Table 6.1: RMS roughness of the measured AFM surface profiles for the Ag-coated NR substrate and for the full NR/Ag/ZnO:Al/a-Si:H/ITO layer stack (100 nm and 200 nm a-Si:H), and of the smoothed profiles generated from the experimental roughness of the Ag coated NR substrate.

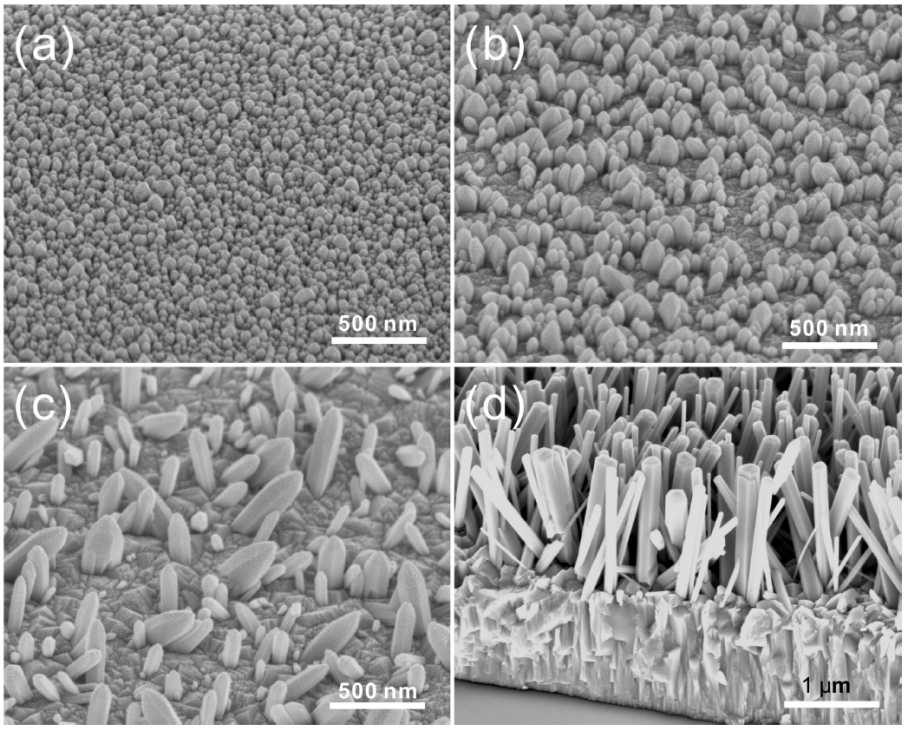

Figure 6.1: SEM images (sample 45° tilted) showing the ZnO NRs prepared by chemical bath deposition. ZnO seed layers with several thicknesses were used: **(a)** 100 nm, **(b)** 500 nm, **(c)** 1000 nm, **(d)** 1000 nm. The precursor concentration and growth time for **(a-c)** are 0.5 mm and 1 h, while for **(d)** these are 10 mm and 3 hours. The growth temperature for all samples is 80°C.

6.3 Results and Discussions

Figure 6.1 shows SEM images of the ZnO nanorods grown on the ZnO seed layers with thicknesses of 100 nm (a), 500 nm (b), and 1000 nm (c). For the thinner seed layer a larger site density of smaller NRs is obtained. For the 500 nm and

1000 nm thick seed layers, well-developed crystalline NRs are obtained. We attribute the difference in NR site density to the difference in grain size at the top surface of the seed layers. A smaller grain size of the seed layer leads to a larger site density of nucleation sites and thus a higher site density of NRs with smaller diameter. The sputtered ZnO seed layer is a polycrystalline material with a preferential c-axis orientation as determined by X-ray diffraction (not shown), favoring the vertical growth of ZnO NRs. During the sputtering process the first few layers of ZnO on glass contain tiny crystallites which act as seeds for subsequent crystal growth. Indeed the grain size in the ZnO thin-film, as calculated from the full width of half maximum of the (002) peak in X-ray diffraction spectra (not shown), shows a steady increase with film thickness. Figure 6.1c and d compare the morphology of NRs obtained at different precursor concentrations and growth time for the same seed layer thickness. When a combination of relatively high precursor concentration and long growth time is used (Figure 6.1d), a high site density of NRs with high aspect ratio is obtained, which is attributed to the larger availability of precursor molecules.

For applications in solar cells, the nanostructures in Figure 6.1a are too small for efficient light scattering while the structures in Figure 6.1d are too dense for subsequent layers to fill the space between the NRs. NR arrays shown in Figure 6.1c provide a good trade-off between high aspect ratio features for light trapping and smooth enough features for a conformal coating by the device stack. This NR array is used for the devices studied in the rest of the chapter.

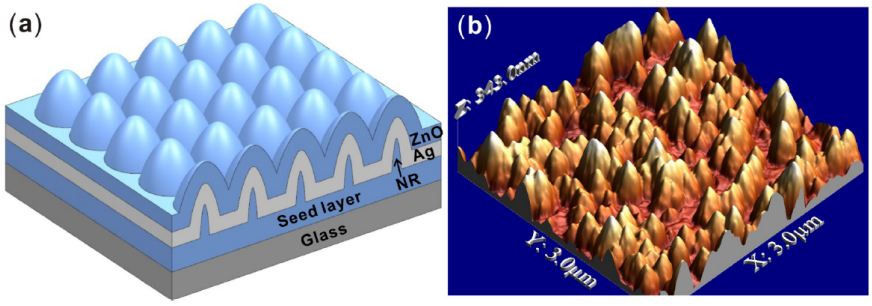

Figure 6.2: Schematic diagram **(a)** and AFM topography **(b)** of the substrate with a structure of ZnO NRs/Ag/ZnO:Al.

Figure 6.2a shows a schematic diagram of the nanorod-based substrate. While in our experiments glass is employed as the mechanical carrier, metal foil or plastic could also be coated with a ZnO seed layer for the growth of NRs to fabricate flexible solar cells. Controlling the Ag thickness is essential to control the feature size of the NR core-shell structures, which is crucial to realize conformal growth of subsequent layers. Figure 6.2b depicts an AFM image of a substrate composed of an NR array with a 200 nm thick Ag layer and an

80 nm thick ZnO:Al layer. Multiple-scale features are visible due to the random chemical growth process for the NRs. The dispersion in feature size results in a broad distribution of spatial frequencies in the scattering surface, which enables a broad spectral response [84, 112]. Aside from acting as a buffer layer for Ag interdiffusion into the a-Si:H, the ZnO:Al layer displaces the propagating modes in the a-Si:H absorber layer from the metal back contact, which reduces the absorption in the Ag layer [66]. Finally, the rounded ZnO:Al features on top of the NRs can act as dielectric scatterers [23, 113].

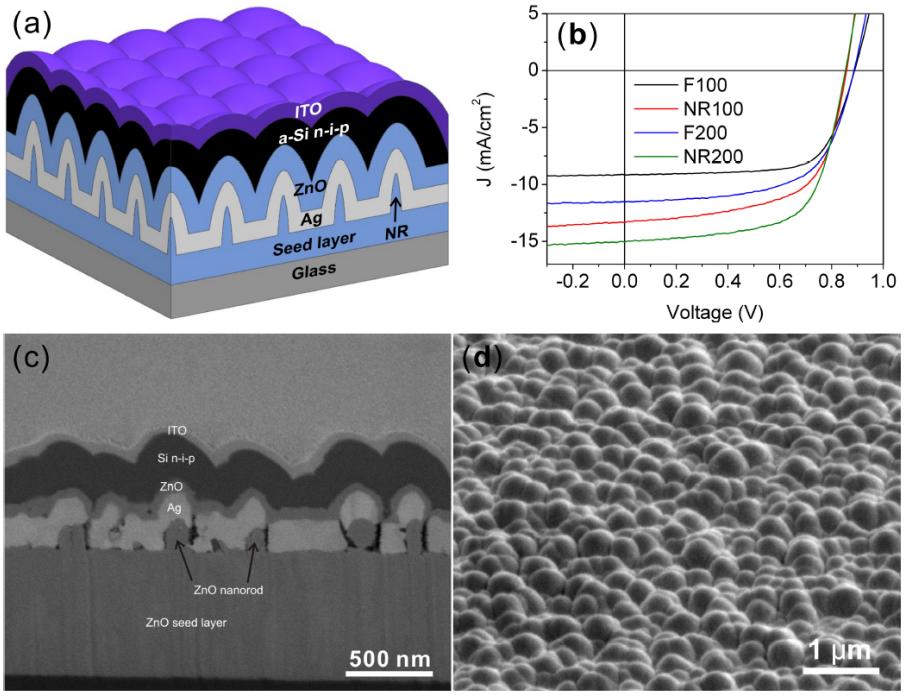

Figure 6.3: Nanorod-based a-Si:H solar cells. **(a)** A schematic of the design. **(b)** J-V results of the flat (F100 and F200) and the NR cells (NR100 and NR200) with 100 nm or 200 nm thick a-Si:H absorber layers. **(c)** Cross-sectional view and **(d)** tilted (52°) top view SEM images of the completed NR cell with a 200 nm thick i-layer (NR200).

A schematic of the full NR solar cell geometry is shown in Figure 6.3a. The J-V measurements for the best cell of each type are plotted in Figure 6.3b. Cell characteristics are listed in Table 6.2. The average performance with standard deviation for the top-ten out of 42 cells with a 200 nm thick i-layer is presented in Table 6.3, for both the NR and the flat cells. The NR cells show substantially higher efficiencies than the flat reference cells. As expected, the performance

gain is in the photocurrent. The relative short-circuit photocurrent enhancements for the NR cells with respect to their flat counterparts are 46% and 30% for 100 nm and 200 nm active layer thicknesses, respectively. Strikingly, the 100 nm thick NR cell, with an efficiency of 7.1%, outperforms the 200 nm thick flat cell, which has an efficiency of 6.4%. The best efficiency of 8.4% is achieved for the 200 nm thick NR cell, corresponding to an absolute efficiency gain of 2% with respect to its flat reference. The photocurrent gain demonstrates that the NR geometry significantly improves light trapping in the thin-film solar cells. The NR cells show a ~30 mV reduction in V_{oc}, with respect to the flat cells. We attribute this to the increased substrate roughness. In the present case the steep valleys between individual NRs can lead to voids and cracks in the active layer due to a shadow effect during PECVD process. In addition, in the NR cells the charge carriers experience a larger junction collection area per projected area than in the planar geometry [114]. The significantly enlarged interface/volume ratio in the NR system can also lead to an increased dark current. The deterioration in V_{oc} in solar cells built on elongated nanostructures has also been reported by several other groups [42, 108, 114–117]. The reduction in V_{oc} in the NR cells obtained here is significantly less than that in earlier work by Kuang et al. on NR cells with less homogeneous coverage of the active layer [105, 111]. Nanostructured cells with comparable V_{oc} as planar or randomly textured counterparts have been fabricated by other researchers [43, 46, 115], indicating there is further room for improvement for the present nanorod geometry.

Cell type	J_{sc} mA/cm^2	V_{oc} mV	FF %	Eff. %
F100	9.1	888.6	70.4	5.7
NR100	13.3	857.4	62.3	7.1
F200	11.5	886.6	62.7	6.4
NR200	15.0	853.5	65.3	8.4

Table 6.2: Characteristics of a-Si:H solar cells on NR substrates and on flat substrates, with intrinsic layer thicknesses of 100 nm and 200 nm.

Cell type	J_{sc} mA/cm^2	V_{oc} mV	FF %	Eff. %
F200	11.4±0.22	887±3	62±1	6.28±0.17
NR200	15.1±0.35	856±7	63±1	8.17±0.13

Table 6.3: Average of J-V parameters of the top-ten cells with 200 nm thick i-layer on the flat and the NR substrates.

Figure 6.3c and d show SEM images of a cross section made by focused ion

beam milling and a top view of the completed NR cell with a 200 nm thick a-Si:H i-layer. In Figure 6.3c several voids are visible between the NRs and the Ag layer. However, these defects do not propagate into the upper layers. This is in agreement with the hypothesis that the Ag and the ZnO layers smoothen the NR profile enough for growth of a high-quality absorber layer. Conformal deposition of the subsequent layers results in a corrugated top surface of the device. The corrugated surface exhibits geometrical resonances and helps to preferentially scatter incident light into the high-index absorber layer [23, 84]. Also the graded effective refractive index can enhance the incoupling of the incident light [118].

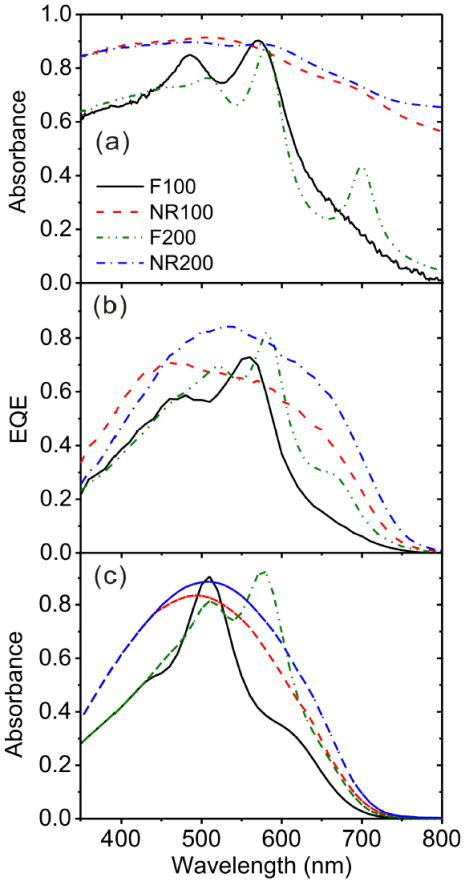

Figure 6.4: Light trapping in the a-Si:H nanorod solar cells and the flat references with 100 nm and 200 nm thick i-layers. **(a)** Measured total absorption spectra, **(b)** measured external quantum efficiency spectra, and **(c)** simulated absorption spectra for the absorber layer.

Figure 6.4a shows the absorption spectra of the whole layer stack determined from reflection and transmission measurements in an integrating sphere. The

NR cells show a broadband absorption enhancement compared to their flat counterparts. The EQE for light at normal incidence in the 350–800 nm spectral range is plotted in Figure 6.4b. The flat cells (F100 and F200) poorly absorb the red and infrared part of the spectrum and therefore the EQE is low in this spectral range. The NR cells (NR100 and NR200) demonstrate a broadband photocurrent enhancement and do not show the Fabry-Perot oscillations that are present in the EQE of the flat cells. In the red part of the spectrum there is a substantial photocurrent enhancement of up to 192% for the NR100 cell and 83% for the NR200 cell with respect to the flat reference cells (at ~650 nm). A strongly enhanced EQE is also observed for short wavelengths up to 500 nm, corresponding to absorption in the top region of the devices. The photocurrent enhancement in this spectral range is attributed to an enhanced incoupling of light [23, 84]. This effect is due to geometrical (Mie) resonances of the corrugated ITO/a-Si:H surface; resonant scattering occurs preferentially into the high index absorber layer and leads to an antireflection effect [23]. The gradual change in refractive index due to the ITO hemispherical features could also contribute to this antireflection effect. Interestingly, below ~450 nm the NR100 cell shows a higher EQE than the NR200 cell. This difference is partially due to the larger surface roughness of the NR100 cell (see Table 6.1), leading to better light incoupling due to the resonant Mie scattering described above.

Figure 6.4c shows the FDTD-simulated absorption in the a-Si:H layer as a function of wavelength. Similar to the trends observed in the experimental EQE spectra, both NR cells show an enhanced red and blue response compared to their flat counterparts. Unlike the EQE data, the simulated absorption curves for the two NR cells with different absorber layer thickness show a similar blue response, since the surface profiles are very similar (see Table 6.1). Indeed, the measured absorption spectra in Figure 6.4a are very similar in the blue spectral range for the two NR cells. The difference in EQE in the blue spectral range is thus attributed to reduced carrier collection for the thicker cells.

Figure 6.5a–d shows the simulated spectra of the absorption in individual layers for the four different cell geometries as well as the reflection spectra of the devices. Several interesting trends can be observed. First of all, the absorption spectra in the intrinsic layer are quite different for the two flat cells, due to the difference in Fabry-Perot modes for the two thicknesses. These flat cells also show large reflection due to poor light trapping in the infrared. Second, the NR cells show a broadband enhanced absorption in the intrinsic layer, with the highest absorption for the thick layer, as expected. In the NR cells the reflectivity is strongly reduced over the entire spectral range, compared to the flat cells. At the same time, absorption in the Ag is substantially larger than for the flat cells for wavelengths larger than 500 nm. Third, for all cell types absorption in the ITO is a significant loss factor at wavelengths below 500 nm. This loss is slightly higher in the NR cells, which is inherent to the resonant behavior of the dielectric structures at the top. Figure 6.5e shows the simulated electric field intensity in the different layers for incident plane waves at 670

and 720 nm wavelengths. Due to the random geometry of the layer stack a complex field distribution is observed. Strong optical hotspots are observed at the ZnO/Ag interface, consistent with the enhanced absorption in the Ag layer. Some hotspots are also observed at the ITO/air interface at positions that depend on wavelength. This demonstrates that the random nature of the pattern, with different feature sizes and hence resonances at different wavelengths, leads to a broad spectral response enhancement.

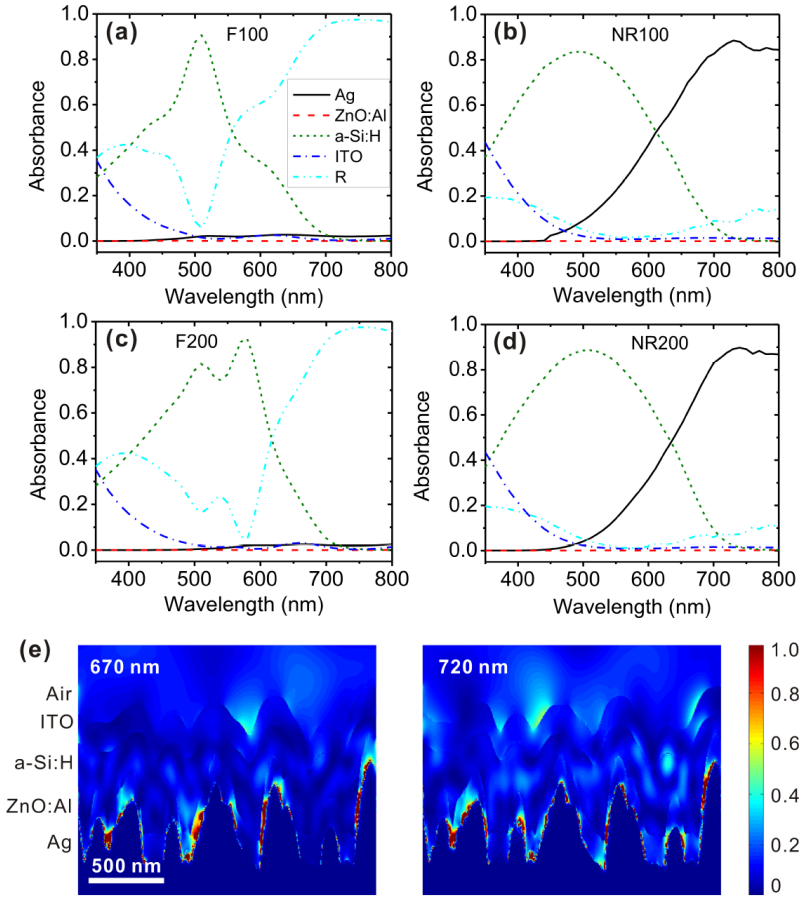

Figure 6.5: FDTD simulations of the absorption spectra of individual layers for the flat **(a, c)** and the NR **(b, d)** cells with 100 and 200 nm intrinsic layer thicknesses; reflectivity (R) is also shown. **(e)** Cross sections of the electric field intensity at 670 nm and 720 nm for an incident plane wave for the NR200 cell. Field intensities are normalized to the incident field (color scale bar). The different layers are indicated at the left schematic. The scale bars are 500 nm.

To investigate the light scattering contribution of the different textured interfaces to the optical performance of the devices, solar cells with several config-

urations are characterized with 3D FDTD simulations. Figure 6.6a shows the studied five geometries:

- flat: all interfaces flat
- NR: all interfaces textured
- flat front: textured Ag/AZO and AZO/a-Si:H interfaces and flat a-Si:H/ITO and ITO/air interfaces
- flat back: textured a-Si:H/ITO and ITO/air interfaces and flat Ag/AZO and AZO/a-Si:H interfaces
- flat Ag: textured AZO/a-Si:H, a-Si:H/ITO, and ITO/air interfaces and flat Ag/AZO interface

The roughness used at the different interfaces is the same as in the simulations of the NR200 cell, while the a-Si:H thickness used is 350 nm to enable for a constant volume of the different layers in all the geometries.

Figure 6.6b shows the simulated absorption in the a-Si:H layer for the different cell geometries. Comparing the spectra for the flat (black) and the NR (red) cells, the same trends are observed as described above for the F100/F200 and NR100/NR200 cells: both blue- and red-response are enhanced in the NR cell. The effect of light trapping in the infrared is relatively small in Figure 6.6b because of the large a-Si:H thickness (350 nm). Flattening the front surface of the NR cell (green) reduces the absorption in the a-Si:H in the blue, confirming the importance of surface roughness for light incoupling in the blue spectral region. For this geometry also a reduced red response is observed, indicating that light scattering from the surface topography leads to enhanced light trapping. The flat back geometry, in which only the front surfaces are textured, shows the same blue-response as the NR geometry, consistent with their similar surface topography. Surprisingly, its red response is significantly better than for the NR cell, demonstrating that texturing only the front interfaces can lead to efficient light trapping. The flat Ag geometry (magenta), in which all interfaces except for the Ag/AZO interface are textured, shows the overall highest absorption. Again, it has a similar blue-response as the NR geometry, but the red response is even larger than for the flat back geometry, showing that texturing the AZO/a-Si:H interface significantly contributes to light trapping. Comparing this geometry to the NR geometry (red) demonstrates that, similar to what is found is Chapter 5 and 7, a rough Ag/AZO interface is not essential for light trapping and flattening this interface can even improve the red-response.

Figure 6.6c depicts the simulated absorption in the Ag layer for the different geometries. Similar to the trends observed for the NR100/NR200 cells described above, the NR cell (red) shows substantially enhanced absorption losses in the Ag layer compared to the flat cell (black). The flat front cell (green) shows somewhat lower absorption in the Ag than the standard NR cell, but the difference in absorption between these two geometries that both have a textured Ag/AZO interface is small. The flat back cell (blue) and flat Ag cell (magenta), which both have flat Ag/AZO interfaces, show substantially lower absorption loss in the Ag layer that the geometries with patterned Ag/AZO interfaces. This explains

their significantly better red-response than the standard NR geometry. The flat Ag geometry, in which the AZO/a-Si:H interface is textured, shows somewhat higher absorption in the Ag layer than the flat front geometry.

Figure 6.6d shows the simulated reflection for the five different geometries. The geometries with flat ITO/air and a-Si:H/ITO interfaces, flat (black) and flat front (green), show significantly higher absorption in the blue spectral range than the geometries with textured front interfaces, NR (red), flat back (blue) and flat Ag (magenta). This is consistent with the trends in the simulated absorption in the blue spectral range. All cell geometries show different reflection in the red spectral range. In this spectral range, the flat cell (black) shows the highest reflection, and the NR cell (red) shows the lowest reflection. Between 600 and 800 nm, the flat front geometry (green) shows higher reflection than the NR geometry and a dip between 740 and 800 nm, which reflects the trend observed in absorption in the Ag layer (Figure 6.6c). The flat back (blue) and flat Ag (magenta) geometries show higher reflection in the red spectral range than the NR geometry. Comparing these two geometries with a flat Ag/AZO interface shows that the flat Ag geometry shows significantly lower reflection in this spectral range than the flat back geometry, consistent with its better red/response observed in Figure 6.6b.

Overall, the purely dielectric light trapping geometry, in which all interfaces except the Ag/AZO interface are textured, gives the best optical performance. In order to fabricate this geometry, a flat glass substrate could be sputter coated with Ag, followed by a thin sputtered layer of AZO, to protect the Ag layer. Subsequently, the nanorods can be grown on top of this layer. In the standard NR geometry, the NR layer was at the back side of the Ag back contact and hence conductivity of this layer was not important. In this geometry with a flat Ag/AZO interface, the NR layer is in the electrically conductive part of the device. Therefore, not only the NR morphology should be tuned, but also the conductivity of this layer should be optimized. Covering the nanorods, which are on top of a conductive AZO layer, with a sputtered layer of AZO could make a conductive textured ZnO substrate if conformal coating of the NR array can be obtained. The thin AZO coating also leads to a smoother morphology, which is required for the growth of the active layer. If required, further improvement of the conductivity could be obtained by growing Al-doped nanorods. Some research has been done on growing Al doped ZnO nanostructures from solution by simply adding Al salt to the precursor solution [119]. Further research would be required to study the influence of Al doping on the NR morphology and conductivity. The fabrication of the active layer and front contact is similar to the protocol used for these layers in the standard NR geometry.

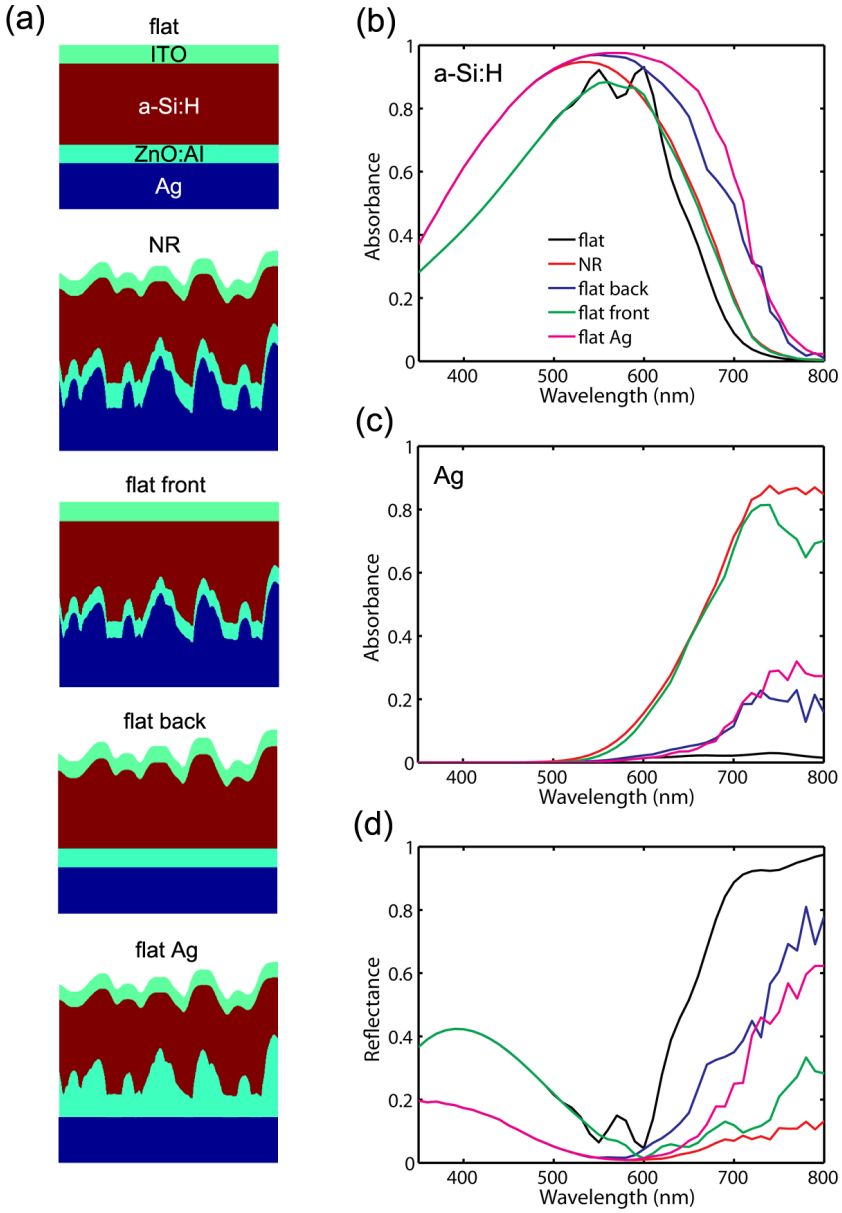

Figure 6.6: Contribution of the rear- and the front-side pattern to light trapping in a-Si:H solar cells. **(a)** Schematic cross sections of the structures used for modeling. Simulated absorption spectra **(b)** in the a-Si:H layer and **(c)** in the Ag layer. **(d)** Simulated reflection spectra of the devices. The volume of the a-Si:H absorber layer is kept constant in all the geometries and is equivalent to that of a 350 nm flat intrinsic layer.

6.4 Conclusion

In summary, we present an efficient nanostructured thin-film a-Si:H solar cell based on a ZnO nanorod template. A ZnO nanorod array is obtained by a simple and inexpensive chemical bath deposition process at low temperature (80°C) and the morphology is tuned by seed layer thickness, reactant concentration, and growth time. An initial efficiency up to 8.4% is achieved for the nanorod-based cells with a 200 nm thick a-Si:H absorber layer, compared to 6.4% for a flat device with a similar absorber layer thickness. EQE measurements on the NR cells show a broad enhancement with respect to the flat cells over almost the entire 350–800 nm spectral range. Corrugation at the top of the NR devices leads to an enhanced blue-response and light trapping is observed in the red part of the spectrum. 3D FDTD simulations are in good agreement with the experimental EQE measurements and show complex field profiles inside the cell. Reflection is significantly reduced for the NR cells, but absorption in the patterned Ag layer is relatively high. The simulations show that for devices with a flat Ag/ZnO:Al interface and textured AZO/a-Si:H, a-Si:H/ITO, and ITO/air interfaces, light trapping is further enhanced due to a reduced absorption in the Ag layer. We also present a strategy for the fabrication of this purely dielectric light trapping geometry. The nanorod growth approach presented in this work does not involve complex manufacturing procedures or equipment requirements. This inexpensive design opens up a new platform for novel efficient cell design that can be made at low cost. With proper back contact material the nanorod substrate is applicable for a variety of PV systems based on e.g. multi-junction thin-film Si, CdTe, and $CuIn_xGa_{1-x}Se_2$.

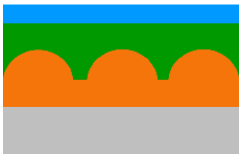

7

Periodic dielectric back patterns for efficient light trapping in thin-film Si solar cells

In this chapter we demonstrate broadband light trapping in thin-film hydrogenated a-Si (a-Si:H) solar cells grown on top of dielectric periodic scattering patterns, consisting of patterned Al-doped ZnO (AZO). This light trapping geometry relies on geometrical (Mie) resonances. External quantum efficiency (EQE) measurements show that the purely dielectric scattering pattern outperforms reference cells made on top of Asahi-U type substrates over the entire 550–800 nm spectral range. Current-voltage measurements show that the device on a purely dielectric scattering pattern has similar electrical properties as the reference cell grown on Asahi-U type glass. FDTD simulations are in good agreement with the EQE measurements and show that the purely dielectric scattering pattern outperforms a combined dielectric-metallic scattering pattern, in which plasmonic resonances also contribute to the light trapping. Using FDTD simulations on single scatterers, we show that dielectric resonances occur both in the AZO particles and in the bottom part of the active layer, which is patterned by growing on the scattering pattern. We find that the size of these a-Si:H scatterers is crucial for efficient light trapping.

7.1 Introduction

Thin-film solar cells combine the advantages of low material consumption and the possibility of mechanically flexible devices. A major problem in all thin-film solar cells is the incomplete absorption of the near-bandgap light. In order to let a device satisfy the opposing requirements of being optically thick and electrically thin, efficient light trapping is required [21, 22]. Many different light trapping geometries have been studied, including randomly textured TCOs, and random and periodic arrays of nanocones, nanodomes, nanorods, and nanoparticles [42, 47, 52, 64, 85, 89, 120–124].

Metal nanoparticles have been studied extensively in light trapping geometries since they exhibit plasmon resonances, which leads to large scattering cross sections [20]. Recently, also wavelength-sized dielectric nanoparticles have gained interest for applications in light trapping. Dielectric particles exhibit geometrical (Mie) resonances in which the light is confined inside the nanoparticle [25]. Similar to metallic nanoparticles, at resonance they have large scattering cross sections, exceeding their geometrical cross sections. Whereas including metallic nanoparticles in solar cells also leads to substantial Ohmic losses, dielectric particles typically show low absorption loss. Efficient scattering without having significant absorption losses in the scatterers could be achieved by making dielectric nanoparticles part of the junction [23, 125], or by using dielectric particles with large scattering cross sections and small absorption cross sections. Nanoparticles with relatively high refractive index and low losses in the visible part of the spectrum could be used at the front of the device, for this e.g. TiO_2 (with n=2.2–2.5) could be used. The other option is to use scatterers with a low refractive index inside an environment with a high refractive index (void resonators) [126]. For light trapping scatterers with large-bandwidth resonances are required in order to achieve broadband photocurrent enhancements. Even though the void resonators in general have broader resonances than particle resonators, also cylindrical particle resonators on top of a substrate exhibit broadband resonances [23, 126]. In this chapter we will consider void resonators at the rear side of the absorber layer. The scatterers could be integrated into the device by fabricating them onto the layer that is deposited previous to the absorber layer and then subsequently growing the absorber layer on top. Materials that satisfy the requirements of having a low refractive index and low absorption coefficient are amongst others, SiO_2, LiF, and AZO. For the choice of material in this geometry it is important that the scatterers do not deteriorate the growth process of the absorber layer.

Many groups have studied light trapping in hydrogenated a-Si (a-Si:H) and μc-Si:H cells grown on top of patterned metal back patterns [92, 127, 128]. In this type of cell the absorber layer is separated from the metal scattering pattern by an AZO buffer layer, which prevents diffusion of Ag into the absorber layer. Due to conformal growth this AZO layer is patterned as well. In chapter 4 we have shown that patterning the AZO buffer layer is indispensable for efficient

light trapping. In this chapter we experimentally demonstrate light trapping in solar cells with purely dielectric scattering patterns, in which we only pattern the AZO layer and make the metal back contact completely flat. In this way we make a dielectric scattering pattern that consists of a material that is naturally present in the device. We present a detailed study of the scattering mechanism of the purely dielectric scattering patterns. We study the scattering of single AZO particles and also of the a-Si:H 'particles' that are enclosed by four AZO particles when the particle diameter approaches the array pitch.

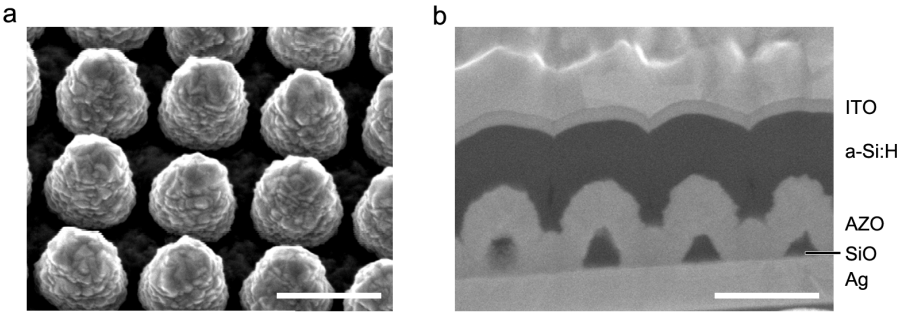

Figure 7.1: SEM images of **(a)** AZO scattering pattern, and **(b)** cross section of the full device made using FIB milling. Scale bars: 500 nm.

7.2 Sample fabrication

Figure 7.1a shows an SEM image of the dielectric scattering pattern, consisting of a periodic array of AZO scatterers. To fabricate these structures, flat glass substrates were sputter-coated with 600 nm Ag, followed by 20 nm AZO, to protect the Ag back contact during fabrication of the nanoparticles. Substrate conformal imprint lithography was used to make the nanoparticle array, since it facilitates high fidelity, large area patterning. A bilayer PDMS stamp was molded onto a master pattern that was made using electron-beam lithography. The glass/Ag/AZO stack was spincoated with PMMA and sol-gel and SCIL was used to make a periodic array of holes in the sol-gel. Reactive ion etching was used to transfer the holes to the PMMA layer. 200 nm SiO was thermally evaporated onto the samples and the PMMA/sol-gel mask was removed, by dissolving the PMMA layer in acetone. The SiO particles were then sputter-coated by 300 nm AZO in order to make a periodically patterned AZO layer. Figure 7.1b shows a SEM image of a cross section of the completed device, made using focused ion-beam (FIB) milling. It shows an a-Si:H layer grown on top of the dielectric scattering pattern. The refractive index contrast between the SiO particles and the AZO is very small; n=1.7 for SiO and n=1.9 for AZO, so the SiO particles will not cause significant scattering. The a-Si:H layer (350 nm i-

layer) was grown in n-i-p configuration using plasma-enhanced chemical vapor deposition as described by Soppe et al. [77]. To define the different cell areas 4×4 mm^2 pads of ITO were sputtered on top of the a-Si:H layer using a contact mask. Finally U-shaped Ag contacts were sputtered on top through a contact mask. In parallel, reference samples without nanoparticles were fabricated on flat glass and Asahi-U type glass.

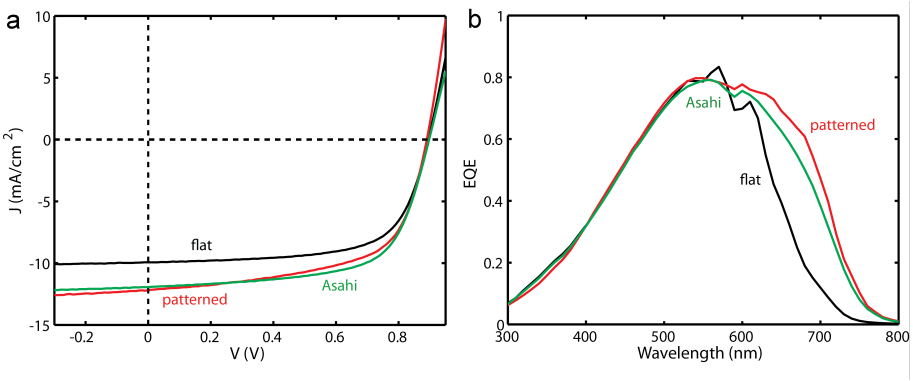

Figure 7.2: (a) IV measurements on flat cell (black), cell with periodic dielectric back pattern (red), and Asahi cell (green). **(b)** shows EQE measurements on the same cells.

7.3 Results

Figure 7.2a shows current voltage measurements for a periodically patterned cell (red), cell on Asahi-U type glass (green), and a flat cell (black). I-V curves were measured under one-sun illumination using a WACOM solar simulator. It can be observed that all three types show similar open circuit voltage (V_{oc}). The patterned cell shows a slight reduction in fill factor (FF). Overall it can be observed that the tall AZO particles do not significantly deteriorate the electrical quality of the device. Current densities were normalized by the values obtained from external quantum efficiency (EQE) measurements to exclude inaccuracies in the determination of the surface area. The Asahi and periodically patterned cell show a substantially larger short circuit current density (J_{sc}) than the flat cell, which indicates improved light absorption.

Figure 7.2b shows the external quantum efficiency measurements on the three different types of cells; measurements are shown for single cells. The EQE measurements were performed on a commercial spectral response set-up (Optosolar SR300) using a 250 W xenon lamp equipped with a monochromator (Jobin Yvon iHR320). The setup was calibrated with a crystalline silicon reference solar cell and the measurements were carried out with a spectral resolution

of 10 nm. All three types of cells show a similar highly reproducible blue-response, indicating that roughness at the front-side of the device, caused by conformal growth, does not play a role in light absorption. At wavelengths above 570 nm the EQE of the flat cell (black) decreases rapidly due to poor absorption of these wavelengths in the thin absorber layers. The Asahi cell (green) shows a significant enhancement in this spectral region, due to light trapping. The cell with purely dielectric periodic scattering patterns (red) shows a red response that is substantially higher than that for the Asahi cell, showing that scattering geometries with flat metal can result in efficient light trapping.

Three-dimensional finite-difference-in-time-domain (FDTD) simulations were performed to study the light trapping in more detail. The full thin-film stack was simulated in a unit cell with a single particle in combination with periodic boundary conditions in x and y direction. At the top and bottom of the simulation box perfectly matched layers (PMLs) were used to absorb the light leaving the simulation volume. A mesh size of 5 nm was used for the entire layer stack. Figure 7.3a shows the simulated absorption as a function of wavelength in the active layer of the patterned (red) and flat (black) cells. Similar to the EQE measurements, the simulation shows a substantial absorption enhancement for the patterned cell compared to the flat cell. Additionally, the simulation shows sharp peaks in the absorption of the patterned cell at wavelengths between 650 nm and 750 nm. We find that the positions of these peaks depend on the array pitch and we attribute them to waveguide mode coupling, which occurs at wavelengths were the parallel momentum provided by the periodic array matches the k-vector of one of the waveguide modes. In the external quantum efficiency measurements, the sharp peaks are not present, which can be explained by the irregular shape of the AZO particles (Figure 7.1a) and the large bandwidth of the monochromator (10 nm). Figure 7.3a also shows the simulated absorption spectra for a 200 nm thick AZO layer (purple). In this case a further enhanced red response is observed.

In chapter 2 we have studied a light trapping geometry that is quite similar to the geometry that we study in this chapter. In the geometry studied in chapter 2, the absorber layer is also grown on top of a patterned AZO layer. However in that geometry the metal is patterned as well, which leads to a contribution of plasmon resonances to the light trapping. To compare the purely dielectric scattering pattern we study in this chapter to the plasmonic geometry of chapter 2 in the simulation we replace the SiO particle, which has no significant refractive index contrast with the AZO layer, with an Ag particle. Figure 7.3b compares the two geometries. Compared to the flat cell (black), the geometry with patterned metal still shows an enhanced red-response, but the absorption is substantially lower than for the cell with the purely dielectric scattering pattern (purple). The light trapping geometry in chapter 2 consisted of 100 nm tall Ag hemispheres, instead of 200 nm tall Ag cylinders.

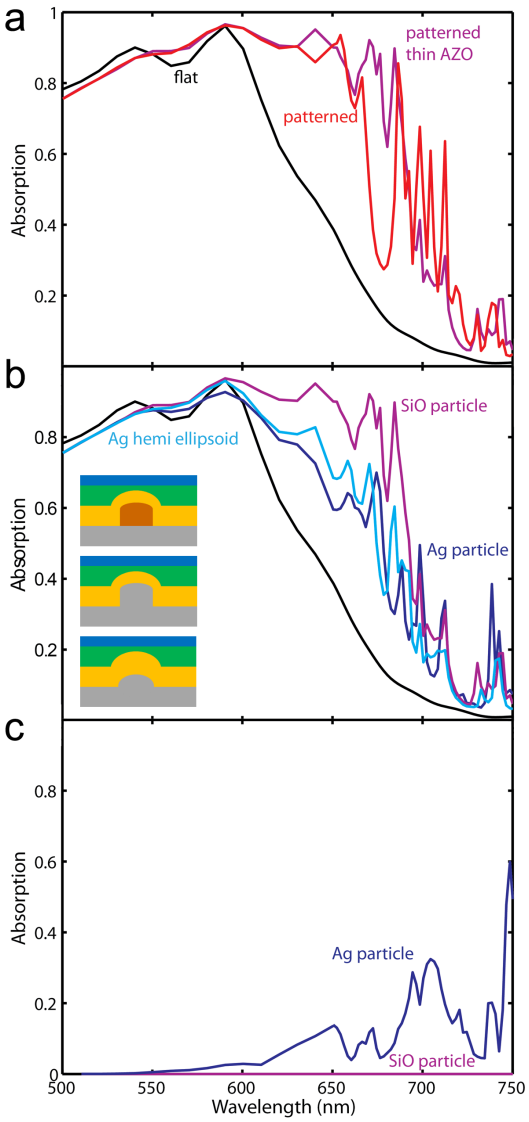

Figure 7.3: Simulated absorption in the a-Si:H layer for different device geometries: **(a)** flat cell (black), periodic dielectric scattering pattern as in experiment (red) and with 200 nm AZO (purple), **(b)** flat cell (black), periodic dielectric scattering pattern (purple; geometry similar to purple in (a), top inset shows schematic cross section), combined metallic-and-dielectric scattering pattern with Ag cylinders (blue; middle inset shows schematic cross section) and hemispheres (cyan; bottom inset shows schematic cross section). **(c)** Simulated absorption in the nanoparticle for the geometries with SiO cylinders (purple) and Ag cylinders (blue).

To improve the comparison with the geometry in chapter 2, we change the height and shape of the Ag particle to make it similar to the Ag particles in chapter 2; we change the particle into a hemi-ellipsoid with a diameter of 300 nm, a height of 100 nm, while maintaining the size and shape of the AZO particle (cyan). Note that in an experimental configuration the use of a shorter Ag particle would also result in a shorter AZO particle, since the shape of the AZO particle is determined by conformal growth on top of the Ag particle. The Ag hemi-ellipsoid leads to slightly better light trapping than the tall Ag cylinder, but still it performs significantly worse than the purely dielectric scattering pattern. Figure 7.3c shows the simulated absorption in the nanoparticle in the geometry with a SiO cylinder (purple) and Ag cylinder (blue). Whereas absorption in the SiO particle is negligible, absorption in the Ag particle is large, starting at wavelengths above 570 nm. This explains why in this spectral range the purely dielectric scattering pattern outperforms the geometry with patterned metal.

To understand the physical mechanism of the dielectric scattering patterns we simulate the scattering cross section for a single scatterer at the AZO/a-Si:H interface. For this we use FDTD simulations with a total-field-scattered-field source and a box of power monitors around the source. PMLs are used at all boundaries. The refractive indices of the a-Si:H layer and the AZO layer were approximated as n=4 and n=2 respectively, with no imaginary parts. The a-Si:H layer and the AZO layer were made infinitely thick by extending them into the PMLs. Figure 7.4a shows the normalized scattering cross section, defined as the scattering cross section normalized to the geometrical cross section, for AZO hemi-ellipsoids with a height of 200 nm and radii of 175 nm, 200 nm, and 225 nm. A broad peak is observed. We attribute the large bandwidth of the peak to radiation into the AZO and a-Si:H layers. Over the full 400–1000 nm spectral range the normalized scattering cross section is larger than 1, indicating strong interaction with the incident light. For increasing particle radius the peak shifts to slightly larger wavelengths, consistent with the resonant (Mie) nature of the scatterer.

In the array geometry the particle diameter is close to the array pitch (pitch=500 nm, radius=220 nm). This causes the AZO particles to enclose a 'Si cross', which potentially also acts as a resonant scatter. Figure 7.4b shows the normalized scattering cross section for a single 'Si cross' enclosed by four AZO particles for AZO particle radii of 175 nm, 200 nm, and 225 nm and a constant array pitch of 500 nm. Thus a smaller AZO particle radius corresponds to a larger 'Si cross'. To exclude a contribution of the AZO particles to the scattering cross section, the particles are connected at the point of minimum spacing between them and extended into the PML boundaries of the simulation volume. Figure 7.4b schematically shows a side and a top view of the simulated geometry.

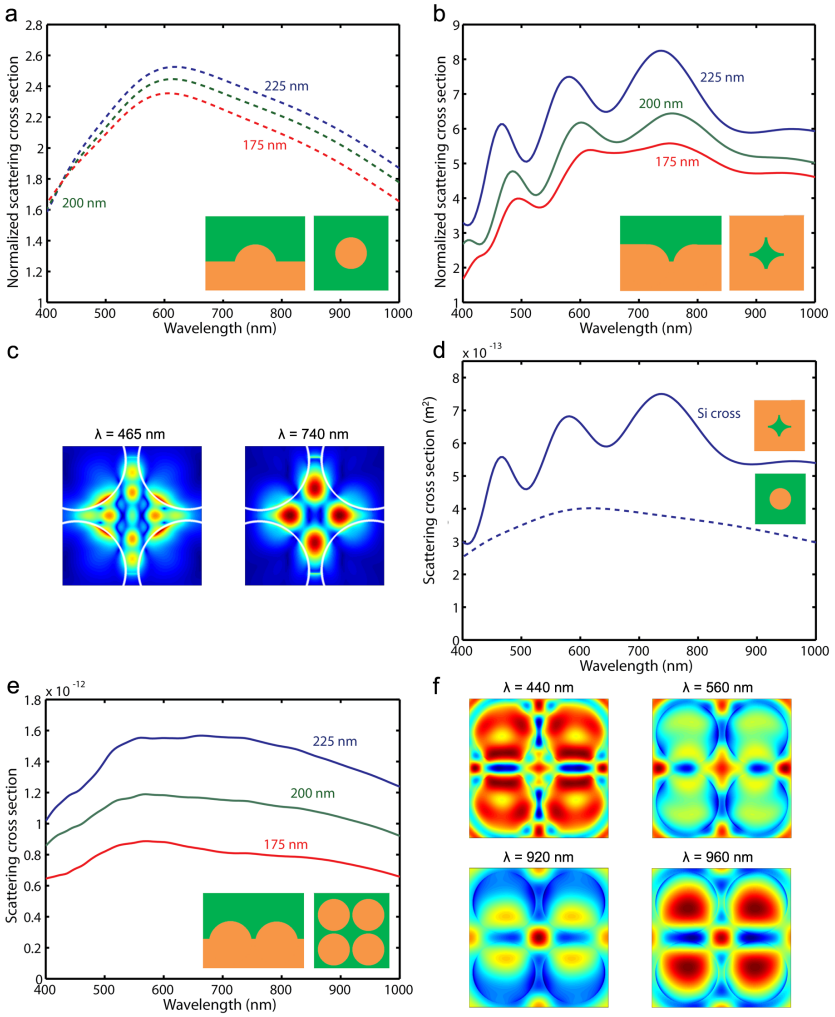

Figure 7.4: Simulated normalized scattering cross section of **(a)** single AZO particles at the AZO-a-Si:H interface with radius 175 nm (red), 200 nm (green), and 225 nm (blue). **(b)** Single Si cross enclosed by AZO scatters extended into PML boundaries in an array geometry with 500 nm pitch. Insets in (a) and (b) show left: schematic xz-view, right: schematic top view. **(c)** XY cross sections of the electric field intensity at the peaks in (b) for wavelengths 465 nm (left) and 740 nm (right). The white circles indicate the positions of the AZO particles. **(d)** Absolute scattering cross section for the Si cross (continuous) and AZO particle (dashed). **(e)** Scattering cross sections for a geometry consisting of 4 AZO particles and 1 Si cross. Left inset: schematic xz-view, right inset: schematic top view. **(f)** XY-cross sections of the electric field intensity at wavelengths of 440 nm, 560 nm, 920 nm, and 960 nm

For this geometry, the normalized scattering cross section shows three distinct peaks. The peaks red shift with decreasing radius of the AZO particle, which corresponds to increasing size of the Si cross, consistent with the behavior of a geometrical resonance. Figure 7.4c shows xy-cross sections of the electric field intensity 1 nm above the interface between the AZO substrate and the a-Si:H layer for the geometry with r=225 nm. The field distributions correspond to the peaks in the scattering spectrum at 465 nm and 740 nm. They both show that the field is resonantly confined in the Si cross, further confirming the presence of geometrical resonances inside the Si cross. To compare the relative contributions of the Si cross and the AZO hemi-ellipsoid to the total scattering in the array geometry, absolute scattering cross sections have to be compared. Figure 7.4d compares the absolute scattering cross section for the AZO particle and the Si cross for an array geometry with 500 nm pitch and 225 nm AZO particle radius. Both scatterers have scattering cross sections in the same order of magnitude, but the scattering cross section of the Si cross (continuous) exceeds the one for the AZO particle (dashed) over the entire spectral range. This indicates that both resonant scattering by the AZO particles and the Si crosses will play a role in the light trapping process.

Figure 7.4e shows the scattering cross section for a more complex geometry. In the previous geometry we extended the AZO scatterers into the PML boundaries, so that the only object that could resonantly scatter the light was the 'Si cross'. Here, we consider a geometry in which the Si cross as well as 4 finite-size AZO particles are present. The scattering cross section shows no distinct peaks. Figure 7.4f shows cross section of the electric field 1 nm above the a-Si:H/AZO interface for four different wavelengths for the geometry with AZO particles with r = 225 nm. Complicated field distributions are observed and, depending on the wavelength, the field is enhanced inside the nanoparticles or inside the Si cross. This further confirms that both types of resonant scatterers contribute to the light trapping process.

FDTD simulations were used to optimize the array geometry. Particle radius, height, and array pitch where varied and the absorption enhancement, defined by:

$$\frac{\int_{\lambda_{\min}}^{\lambda_{\max}} A_{\text{patterned}}(\lambda) AM1.5(\lambda) d\lambda}{\int_{\lambda_{\min}}^{\lambda_{\max}} A_{\text{flat}}(\lambda) AM1.5(\lambda) d\lambda}$$

with $\lambda_{\min}$ = 500 nm and $\lambda_{\max}$ = 750 nm. We find that near optimal absorption enhancement can be obtained with multiple combinations of particle radius and array pitch. Figure 7.5 shows the absorption enhancement as function of the cross area, which is defined as $P^2 - \pi \cdot r^2$ for different particle heights. The thickness of the AZO layer below the nanoparticles is 200 nm for all geometries. The arrow indicates the geometry simulated in Figure 7.3a. Cross areas between 1.1×10^5 nm^2 and 2.0×10^5 nm^2 give the largest absorption enhancement; enhancement factors near 40% are obtained in this range. For areas larger or

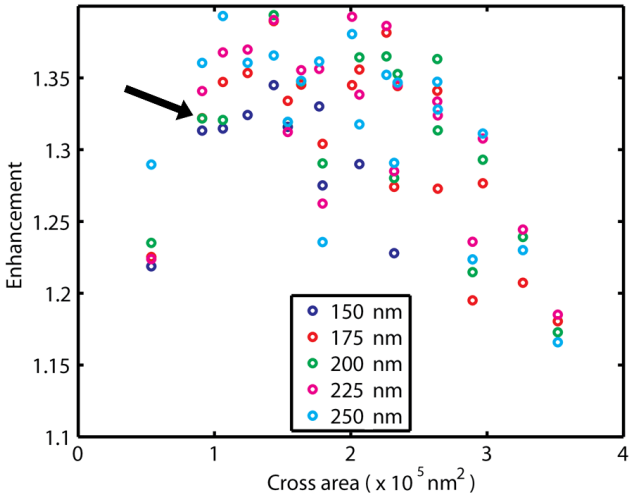

Figure 7.5: Absorption enhancement as a function of Si cross area for particle heights 150 nm (blue), 175 nm (red), 200 nm (green), 225 nm (magenta), 250 nm (cyan). The black arrow indicates the geometry simulated in Figure 7.3a.

smaller than these values the absorption enhancement is lower. This graph indicates that the optimum height depends on the array pitch and radius. This further confirms the contribution of the Si cross to the light trapping.

7.4 Conclusion

We have fabricated solar cells on purely dielectric scattering patterns, consisting of a periodic array of AZO particles at the AZO/a-Si:H interface. External quantum efficiency measurements show that these patterns lead to efficient light trapping and outperform reference cells grown on top Asahi-U type texture. IV measurements show that that the AZO back patterns do not significantly deteriorate the electrical properties of the cells. FDTD simulations are in good agreement with EQE measurements and show that the purely dielectric scattering pattern also outperforms a combined metal-dielectric scattering pattern, in which the Ag back contact is patterned as well. FDTD simulations on single scatterers show that both the AZO particles and the Si 'particles' enclosed by AZO particles in the array geometry are resonant scatterers, with similar scattering cross sections. The importance of these a-Si:H scatterers is further confirmed by investigating trends seen in the optimization of the array geometry. Whereas different AZO particle radii and array pitches lead to a near-optimum absorption enhancement, for the aSi scatterer the large enhancement is only obtained in a certain area range.

8

Light coupling and trapping in ultra-thin Cu(In,Ga)Se_2 solar cells using dielectric scattering patterns

We experimentally demonstrate photocurrent enhancement in ultra-thin CIGSe solar cells, with absorber layers of 460 nm, by using nanoscale dielectric light scattering patterns. We show that patterning the front side of the device with arrays of TiO_2 nanoparticles results in a small photocurrent enhancement in almost the entire 400–1200 nm spectral range due to enhanced light coupling into the cell. Three-dimensional FDTD simulations are in good agreement with the experimental external quantum efficiency measurements. Patterning the Mo/CIGSe back interface using SiO_2 nanoparticles leads to enhanced light trapping, increasing the efficiency from 11.0% for a flat cell to 12.4% for a patterned cell. FDTD simulations show that optimizing the array geometry could further improve light trapping. Including nanoparticles at the Mo/CIGSe interface leads to substantially reduced parasitic absorption in the Mo back contact for these thin solar cells. Parasitic absorption in the back contact can be further reduced by fabricating CIGSe cells on top of a SiO_2-patterned ITO back contact. Simulations demonstrate that these cells show the same spectrally averaged reflection and absorption in the CIGSe active layer as a Mo-based patterned cell, making them interesting candidates for the top cell in multi-junction devices.

8.1 Introduction

In previous chapters we have studied light trapping in thin-film amorphous Si solar cells. We found that using dielectric scattering patterns leads to very efficient light trapping while optical losses in the scatterers are small. In this chapter we use dielectric light trapping patterns in Cu(In,Ga)Se_2 (CIGSe) solar cells. CIGSe solar cells are promising thin-film candidates with efficiencies up to 20.8%, which exceeds the current multicrystalline Si record efficiency [5, 129]. Another interesting aspect of CIGSe cells is that by varying the Ga/(In+Ga) ratio from 0 to 1 the band gap can be varied between 1.0 and 1.7 eV [130], which opens possibilities for tandem devices. Currently, the standard thickness for CIGSe cells is 2–3 μm, but in view of In scarcity and to enhance throughput it is favorable to reduce the thickness of the absorber layer. However, growing ultra-thin absorber layers with high electronic quality is challenging and reducing the cell thickness below 1 μm leads to a large reduction in photocurrent. The reason for this is twofold. First, thinning down the absorber layer thicknesses below 1 μm leads to strongly enhanced recombination at the back contact [131]. The recombination can be reduced by increasing the [Ga]/([Ga]+[In]) ratio ([Ga]/[III]) towards the back contact ('back Ga grading'), leading to an effective electron reflector [131–136]. Second, reducing the active layer thickness below 1 μm leads to substantially reduced light absorption. Figure 8.1 shows the calculated attenuation length of the CIGSe material used in this chapter, which has a band gap near 1200 nm (1.0 eV). The optical constants were extracted from reflection and transmission measurements on single layers deposited on glass. This graph shows that reducing the absorber layer thickness to 1 μm leads to less than 1/e attenuation for all wavelengths above 1050 nm. Therefore thinning down the absorber layer makes efficient light trapping indispensable. So far, only a limited number of research groups have worked on light management in CIGSe cells [131, 137–139] and no experimental demonstration of light trapping in CIGSe cells has been published. Light trapping in ultra-thin CIGSe cells is challenging because of parasitic absorption in the Mo back contact. The absorption losses in the Mo back contact are a substantial loss factor in ultra-thin CIGSe cells. Depositing the metal back contact on textured glass, which is often done to achieve light trapping in thin-film Si cells, is not an option as it would lead to even higher absorption losses in the Mo. Replacing Mo with a different material remains challenging, due to the electronic quality of the contact and diffusion of the back contact material into the absorber layer. This also makes the use of metallic nanoparticles at the back contact for light trapping very difficult. It was found that W, Nb, and Ta could replace Mo as a back contact material without affecting the absorber growth, but these materials still lead to much higher parasitic absorption than, for instance, Ag and Al [140]. CIGSe cells can also be grown on ITO or ZnO back contacts. Using ITO or ZnO leads to substantially lower absorption in the back contact and is interesting for applications in multi-junction devices. It was shown that

a very thin $MoSe_2$ layer in between the ITO and the absorber layer, which facilitates carrier transport through tunneling, could lead to high quality devices by making a quasi-Ohmic contact [141].

In this chapter we use dielectric scattering patterns to enhance absorption in ultra-thin CIGSe cells with a layer thickness of only 460 nm. We study the influence of dielectric scatterers both at the front of the device and at the interface between the absorber layer and the back contact. Finally the light trapping patterns are applied to cells with ITO back contacts.

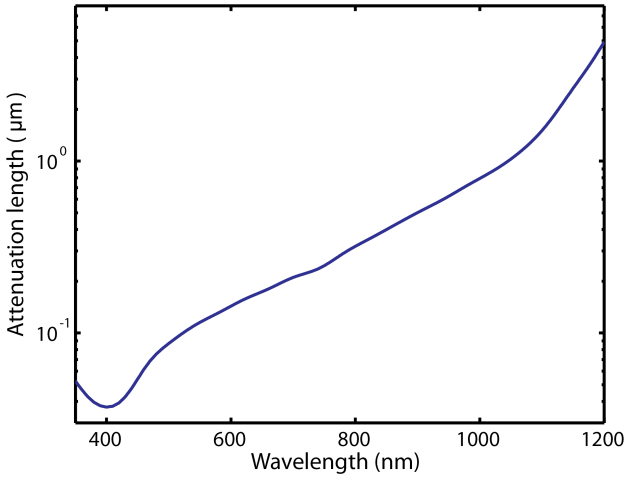

Figure 8.1: Calculated 1/e attenuation length as a function of wavelength of CIGSe absorber material.

8.2 Methods

CIGSe absorber layers with a thickness of only 460 nm were deposited by a three-stage co-evaporation process on Mo-coated soda-lime glass substrates [142]. The deposition was carried out at a substrate temperature of 440°C, since this was found to result in a high Ga/(In+Ga) grading, which leads to reduced recombination at the back contact as described in ref [143]. Subsequently a 50 nm CdS buffer layer was grown via chemical bath deposition in a solution with 1.1 M ammonia, 0.14 M thiourea and 0.002 M cadmium acetate. This was followed by magnetron sputtering of 130 nm i-ZnO and 240 nm AZO. Mechanical scribing was used to separate the cells into 0.5 cm^2 areas. Metal grids, consisting of 10 nm Ni and 1 μm Al, were evaporated on top. Substrate conformal imprint lithography (SCIL) was used to fabricate dielectric particles at the back and front side of the device. To pattern the front-side, the sample was coated with PMMA and sol-gel, and the sol-gel layer was patterned with an array of holes using SCIL, followed by e-beam evaporation of TiO_2

and lift off of the mask. To pattern the back side, SCIL was used to pattern a sol-gel layer on top of PMMA on the Mo coated substrate followed by e-beam evaporation of SiO_2 and lift off of the mask. The Mo layer with dielectric nanoparticles was then used as a substrate for deposition of the subsequent device layers.

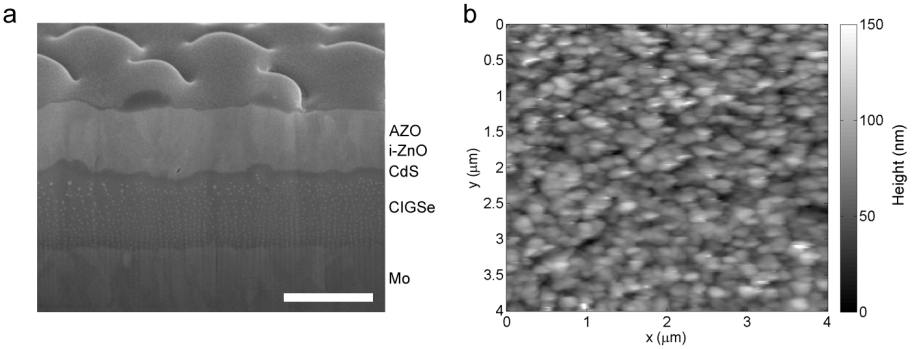

Figure 8.2: (a) SEM image of cross section of an unpatterned CIGSe solar cell, made by FIB milling. The scale bar indicates 500 nm. **(b)** AFM scan of CIGSe layer.

8.3 Results

Figure 8.2 shows an SEM image of a cross section made using focused ion beam (FIB) milling of an ultra-thin CIGSe cell. Some roughness is observed at the CIGSe top interface, which also propagates in the CdS layer and flattens out in the top layers. Figure 8.2b shows the topography of the CIGSe layer, measured by atomic force microscopy (AFM) before the CdS/i-ZnO/AZO stack was deposited. Figure 8.3a shows current-voltage (I-V) measurements for flat cells before printing nanoparticles on top (black) and the same cells after printing periodic arrays of TiO_2 particles on top (red). The square array geometry has a pitch of 500 nm, particle radius of 120 nm, and particle height of 120 nm. I-V measurements were done using a WACOM dual beam solar simulator under 1 sun illumination. Data for flat cells is averaged over 5 cells, and data for patterned cells is averaged over 4 cells. The higher slope at negative bias for the flat cells (black) indicates a lower parallel resistance for these cells. Figure 8.3b shows the electrical parameters extracted from the IV-measurements. Differences in open circuit voltage (V_{oc}) and fill factor (FF) are small between the different cell types. For both cell types V_{oc} and FF are somewhat low, indicating a suboptimal quality of the active layers. Overall, the patterning does not significantly influence the electrical parameters of the cell, indicating that SCIL printing is very well compatible with CIGSe solar cells. This could be further confirmed by redoing the experiments with optimal-quality devices.

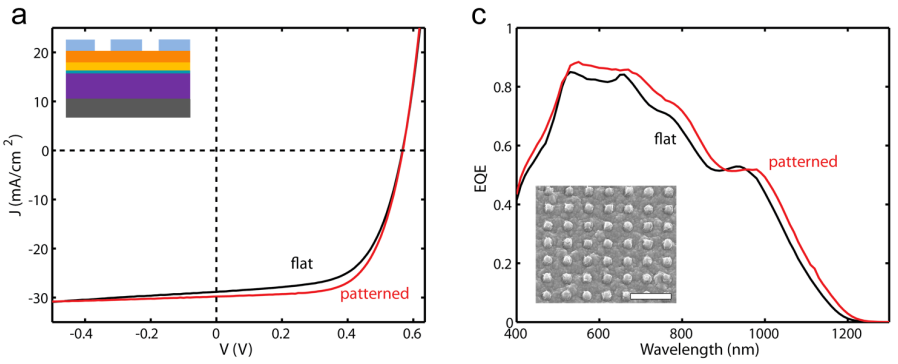

b

cell type	V_{oc} (mV)	J_{sc} (mA/cm^2)	FF (%)	efficiency (%)
flat	567	29.6	62.4	10.1
patterned	568	29.8	64.6	10.9

Figure 8.3: (a) IV-measurements for flat cells (black) and cells with a periodic array of TiO_2 particles on top (red). The inset schematically shows the cell geometries for the patterned cells, consisting of Mo (grey), CIGSe (purple), CdS (cyan), i-ZnO and AZO (orange), and TiO_2 particles (blue). **(b)** Extracted parameters from the IV-measurements. **(c)** EQE measurements for the flat (black) and patterned (red) cells in (a). The inset shows an SEM image of the patterned front surface. The scale bar indicates 1 µm.

Figure 8.3c shows external quantum efficiency (EQE) spectra measured for flat (black) and patterned (red) cells. The external quantum efficiency (EQE) was measured with a two-source illumination system, consisting of a Xe and halogen lamp. The EQE for the flat cell (black) shows oscillations at wavelengths above 500 nm that we attribute to Fabry Perot effects in the CdS/i-ZnO/AZO layer stack. Similarly, the main peak near 1000 nm is attributed to a Fabry-Perot interference in the CIGSe layer, since the absorption length exceeds the device thickness at that wavelength (see Figure 8.1). At wavelengths above 650 nm the EQE decreases rapidly due to poor absorption in the ultra-thin CIGSe layer. Compared to the flat cell, the patterned cell (red) shows an enhanced EQE in the 500–1200 nm spectral range, with the exception of a narrow wavelength band from 900–950 nm. The inset shows an SEM image of the TiO_2 particle array printed onto the completed solar cells.

Three-dimensional finite-difference time-domain (FDTD) simulations were used to study the optical performance of the devices in more detail. The complete thin-film stack was taken into account and the topography of the CIGSe/CdS interface as measured using AFM (Fig. 8.2b) was included by directly importing the AFM data in the simulations. The topography of the CdS/i-ZnO interface was assumed to be identical to that at the CIGSe/CdS interface with the height variations halved. The optical constants of all layers were extracted from trans-

mission and reflection measurements on single layers on glass substrates as described in [144, 145]. A 5 nm mesh was used over the entire simulation volume. Perfectly matched layers were used at the top and bottom of the simulation volume and periodic boundary conditions were used in x and y dimensions. Varying the box size of a cell without nanoparticles on top between 400 nm and 1 μm did not show significant differences in the simulated absorption, indicating that discontinuities at the boundaries do not significantly influence the results. Figure 8.4a shows the FDTD-simulated reflection and absorption spectra for the different layers of the device for flat cells (continuous lines) and patterned cells (dashed lines). The absorption spectrum for the flat cell shows Fabry Perot oscillations at wavelengths above 500 nm. Compared to the EQE measurements in Figure 8.3c, these oscillations are somewhat more pronounced, which we attribute to differences in roughness of the device between the experiment and the simulation and to the fact that the simulation assumes full collection of carriers generated in the active CIGSe layer, while in reality this may not be the case. Furthermore, compared to the experiment, the oscillations are slightly red-shifted in the simulation, which we attribute to differences in the layer thickness between the experiment and the simulation. In particular the CdS layer, which is deposited in a chemical bath, is susceptible to thickness deviations. In the simulations we set the thickness of the CdS layer to 50 nm, which was the desired thickness for this layer in the experiment. Similar to the trend in the EQE measurements, the patterned cell (red) shows an enhanced response over almost the entire wavelength range. Overall, the simulated absorption data agree well with the experimentally determined EQE data.

Figure 8.4a also shows that absorption in the TiO_2 nanoparticles, averaged over the AM1.5 spectrum, is below 1%. Absorption in the Mo back contact (magenta) is large at wavelengths where the device is not optically thick (> 800 nm). This poses a main limitation in the efficiency of ultra-thin CIGSe cells. Patterning the cell leads to a small increase in the absorption in the Mo layer. Absorption in the CdS (blue), AZO (cyan), and i-ZnO (orange) remain almost unchanged upon patterning the cell. The simulated absorption spectra show that patterning the cell mostly enhances the absorption in the CIGSe layer at wavelengths between 450 nm and 950 nm, whereas the enhancement is small at larger wavelengths, where absorption in the CIGSe layer is weaker. To distinguish between light trapping and anti-reflection effects of the nanoparticles, Figure 8.4b compares the simulated absorption in thin cells (continuous lines) to cells with an infinitely thick absorber layer (dashed lines). At wavelengths up to 570 nm, the absorption spectra for thin and thick flat cells are similar; the same is observed when comparing thin and thick patterned cells. At these wavelengths the CIGSe layer is still optically thick. At larger wavelengths, the absorption in the thin cells starts to deviate from the absorption in the thick cells. Both the thick and the thin flat cells show a dip at 700 nm, which is attributed to a Fabry Perot effect in the window layers and in both cases patterning the cells leads to a similar absorption enhancement. Overall, com-

paring results for thick and thin cells shows that the enhancement obtained by patterning a thick cell is very similar to the enhancement obtained when patterning a thin cell. This indicates that patterning mostly results in an anti-reflection effect, and that light trapping does not significantly contribute to the enhanced absorption in thin patterned cells. This antireflection effect is due to preferential forward scattering of the light by the nanoparticles, since the TCO layers below have a larger refractive index than air, as demonstrated earlier for Si wafers and thin-film amorphous Si solar cells [20, 23, 84].

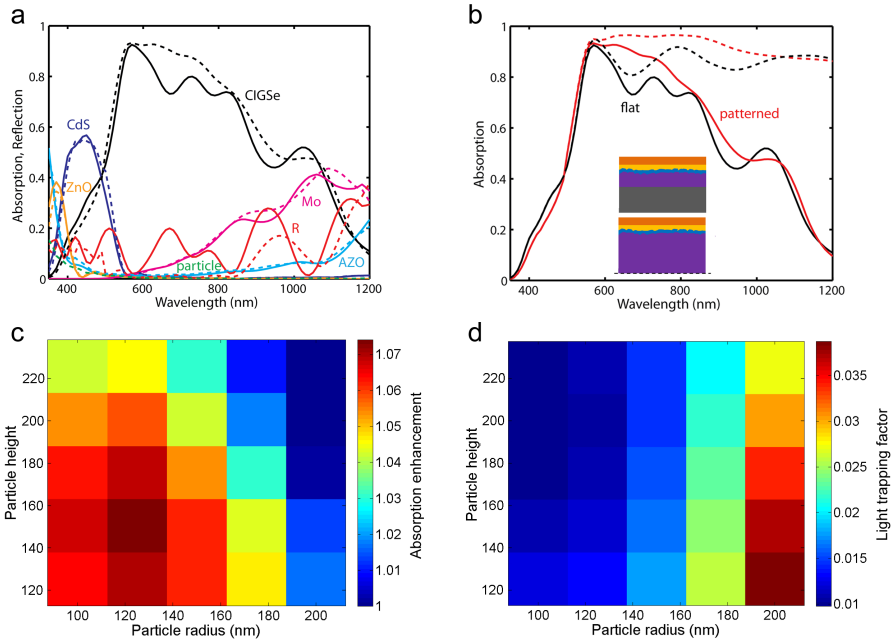

Figure 8.4: **(a)** Simulated absorption in Mo (magenta), CIGSe (black), CdS(blue), ZnO (orange), AZO (cyan), TiO_2 particles (green), and simulated reflection (red) for cells with TiO_2 particles (dashed) and flat cells (continuous). **(b)** Simulated absorption in CIGSe layer for flat (black) and patterned (red) thin cells (continuous lines) and infinitely thick cells (dashed lines). Insets show the cell geometries for the thin cell (top), consisting of Mo (grey), CIGSe (purple), CdS (cyan), i-ZnO and AZO (orange), and infinitely thick cell (bottom). The dashed line indicates the bottom PML boundary. **(c)** AM1.5 averaged absorption in patterned cells with different combinations of particle radius and height and an array pitch of 450 nm. **(d)** AM1.5 averaged light trapping for the same array geometries as in **(c)**.

FDTD simulations were used to optimize the array geometry for maximum AM1.5 averaged absorption enhancement in the CIGSe layer, defined by

$$\frac{\int_{\lambda_{\min}}^{\lambda_{\max}} A_{\mathrm{p}}(\lambda) AM1.5(\lambda) d\lambda}{\int_{\lambda_{\min}}^{\lambda_{\max}} A_{\mathrm{f}}(\lambda) AM1.5(\lambda) d\lambda}$$

with $AM1.5$ the solar spectral intensity in $\mathrm{Wm^{-2}nm^{-1}}$, A_{p} and A_{f} the absorption in the patterned and the flat cell, respectively, $\lambda_{\min}$ = 350 nm and $\lambda_{\max}$ = 1200 nm. To find the best geometry, a parameter sweep was done over the particle radius, height and the array pitch, using a square array geometry. Figure 8.4c shows the calculated absorption enhancement as a function of particle radius and height for an array pitch of 450 nm. It shows that the geometry with a particle radius of 125 nm and height of 150 nm results in the largest absorption enhancement. To study the contribution of light trapping as a function of array geometry, we compare the difference in enhancement between patterning a thin cell and patterning an infinitely thick cell with the same array geometry. Figure 8.4d shows the light trapping enhancement, defined by

$$\int_{\lambda_{\min}}^{\lambda_{\max}} \left[(A_{\mathrm{p,thin}} - A_{\mathrm{f,thin}}) - (A_{\mathrm{p,thick}} - A_{\mathrm{f,thick}}) \right] AM1.5(\lambda) d\lambda$$

with $A_{\mathrm{p,thin}}$ the absorption in a thin patterned cell, $A_{\mathrm{f,thin}}$ the absorption in a thin flat cell, $A_{\mathrm{p,thick}}$ the absorption in a thick patterned cell, and $A_{\mathrm{f,thick}}$ the absorption in a thick flat cell. Whereas the geometry with radius 125 nm and height 150 nm results in the largest overall absorption enhancement, shown in Figure 8.4c, light trapping in this geometry is poor. The light trapping increases for larger particl radii, but increasing the radius comes at the expense of the total absorption enhancement. This shows that for the geometries that result in a substantial absorption enhancement, light trapping only has a minor influence on the total absorption enhancement (Figure 8.4c), indicating that the enhancement is mostly due to an antireflection effect. We find the same trend as in Figure 8.4c and d for different array pitches in the range 400–650 nm.

To achieve light trapping in ultra-thin CIGSe cells, we fabricated arrays of SiO_2 nanoparticles at the Mo/CIGSe interface. Figure 8.5a shows an SEM image of a cross section of the device that was made by FIB milling. The particle array is observed on top of the Mo layer. The CIGSe layer was deposited on top of the particle array and conformally fills the gaps in between the particles, which should lead to good electrical contact. In the subsequent layer deposition the pattern caused by the particle array flattens out, but some corrugation is still observed at the front-side of the device.

Figure 8.5b shows the IV measurements for flat cells (back) and patterned cells (red). Data are averages of 6 cells. The patterned and unpatterned cells show similar overall shapes of the IV-curves while the patterned cells show a clear enhancement in J_{sc}. Figure 8.5c summarizes the electrical parameters for the different cell types. Patterning of the cells leads to an enhancement in V_{oc} from 583 mV to 592 mV and in J_{sc} from 28.6 $\mathrm{mA/cm^2}$ to 30.6 $\mathrm{mA/cm^2}$, the latter directly the result of the enhanced absorption of the incident light. A

slight enhancement in FF from 67.4% to 68.2% is obtained upon patterning the cells. Overall these data show that growing cells on top of SCIL printed SiO_2 particles on Mo does not significantly deteriorate the electrical properties of the device. The SiO_2 particles may even improve the electrical properties of the device, by reducing back contact recombination, but further experiments would be required to study this.

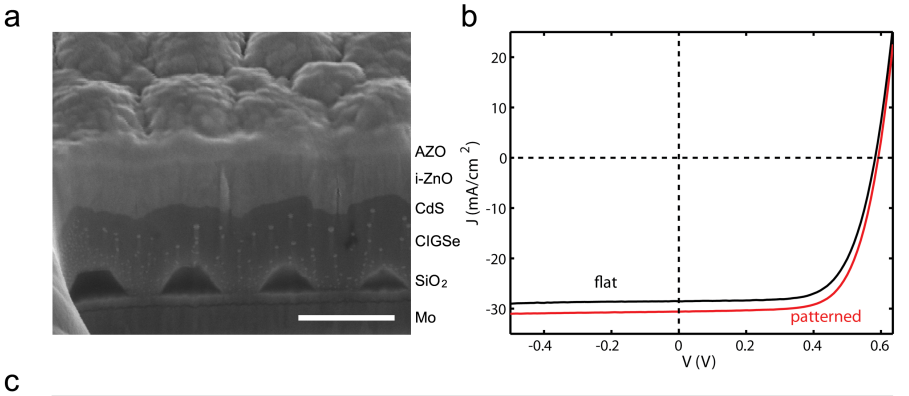

c

cell type	V_{oc} (mV)	J_{sc} (mA/cm^2)	J_{sc} from EQE (mA/cm^2)	FF (%)	efficiency (%)
flat	583	28.6	28.2	67.4	11.0
patterned	592	30.6	30.5	68.2	12.4

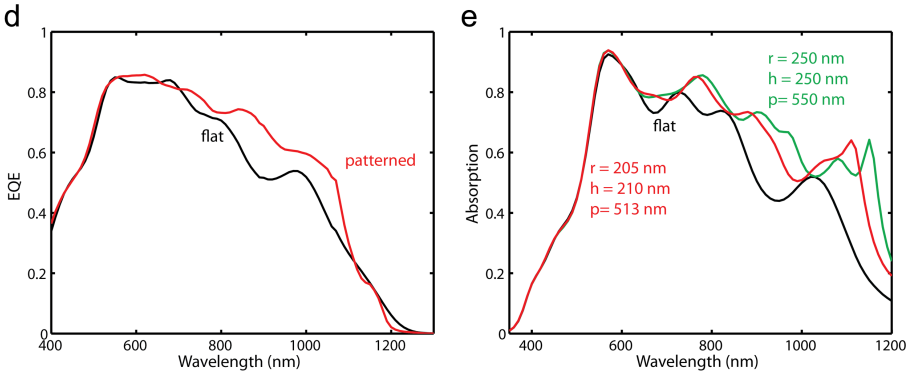

Figure 8.5: (a) SEM image of cross section of a CIGSe solar cells with a periodic array of nanoparticles at the Mo/CIGSe interface. The scale bar indicates 500 nm. (b) IV-measurements for flat (black) CIGSe cells and cells with arrays of SCIL printed SiO_2 particles at the CIGSe/Mo interface (red). (c) Summary of the electrical parameters for both cell types. (d) EQE measurements on the same cell types. (e) FDTD-simulated absorption for a flat cell (black), cell with the same nanopattern as in the experiment (red), and with an optimized nanopattern (green).

Figure 8.5d shows the EQE measurements for flat (black) and patterned (red) cells. At wavelengths up to 550 nm the flat and the patterned cell show a similar response, indicating that the corrugation at the front-side of the devices, which is caused by conformal growth on the particle arrays, does not significantly influence the absorption of the incident light. For wavelengths above 700 nm the EQE of the flat cells (black) decreases significantly due to incomplete absorption of the incident light in the ultra-thin-absorber layer. The patterned cells (red) show a substantial enhancement in this spectral range due to light trapping. To exclude the effect of inaccuracies in the determination of the surface area of these small cells (0.5 cm^2) on the determination of J_{sc}, J_{sc} was also calculated from the EQE measurements (Figure 8.5c) and these values were used to calculate the cell efficiencies. Overall, patterning the back contact of the cell results in a significant increase in efficiency from 11.0% to 12.4%, calculated with the corrected J_{sc} values.

To study this light trapping geometry in more detail, FDTD simulations were performed. In the simulations, the absorber layer thickness of the patterned cell was increased to compensate for the volume excluded by the SiO_2 particles, so that the total absorber volume was the same for the flat and patterned geometries. Figure 8.5e shows the simulated absorption in the CIGSe layer for flat (black) and patterned (red) cells. The trends in simulated absorption are in good agreement with the trends in EQE measurements. Up to 650 nm, the absorption spectra for flat and patterned cells are similar. At larger wavelengths the patterned cell shows significantly enhanced absorption. A clear absorption peak is observed near 1100 nm, which is also present in the EQE measurements in Figure 8.5d. In additional simulations, keeping particle height and diameter constant and increasing the array pitch, we find the peak wavelength increases with the array pitch. We attribute this peak to waveguide-mode coupling. Finally, we optimized the array geometry by changing the particle radius and height and found a further optimized absorption spectrum for the CIGSe layer (Figure 8.5d, green).

Figure 8.6a shows the simulated absorption in all different layers as well as the reflection for the flat (continuous lines) and optimized patterned (dashed lines) cells. At wavelengths for which cell patterning leads to enhanced absorption in the CIGSe layer (black), also a changed reflection spectrum is observed. Overall the patterning leads to a reduced reflection. Furthermore, patterning also leads to a substantial reduction of absorption in the Mo back contact (magenta).

Since absorption in the Mo back contact is a major loss factor in thin-film CIGSe cells, growth of absorber layers on alternative back contacts is of great interest. Figure 8.6b shows the simulated reflection, transmission, and absorption in SiO_2 patterned (dashed lines) and unpatterned (continuous lines) devices on ITO back contacts. Whereas the cells on Mo showed up to 40% absorption in the back contact (for the flat cell, at 1050 nm), the absorption in the ITO layer of this geometry is always below 15%. The flat CIGSe cell on ITO

(black, continuous line) shows an absorption spectrum that rapidly decreases at wavelengths above 750 nm. Compared to the geometry with Mo in Figure 8.6a the overall absorption in the CIGSe layer is lower. The average reflection from the flat cell on ITO is similar to the reflection for the cell on Mo.

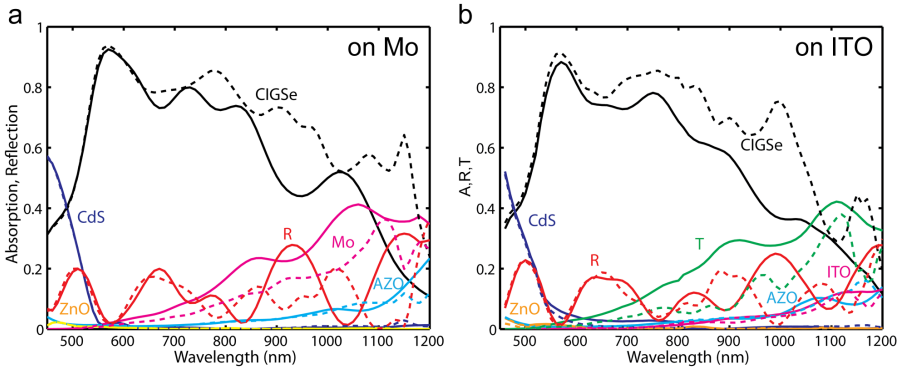

Figure 8.6: Simulated optical losses in thin-film CIGSe cells on (a) Mo and (b) ITO back contact. Continuous lines show data for flat cells and dashed lines for patterned cells. (a) Simulated absorption in the CIGSe layer (black), AZO layer (cyan), CdS layer (blue), ZnO layer (orange), Mo layer (magenta), and simulated reflection (red). (b) Simulated absorption in the the CIGSe layer (black), AZO layer (cyan), CdS layer (blue), ZnO layer (orange), ITO layer (magenta), simulated reflection (red), and simulated transmission through the device stack (green).

The layer stack shows increasing transmission at wavelengths above 550 nm, exceeding 40% at 1120 nm. However, patterning the ITO layer with SiO_2 particles leads to a substantially enhanced absorption in the CIGSe layer (black, dashed line) over the entire 600–1200 nm spectral range. This absorption enhancement is mainly due to reduced transmission (green). Patterning also leads to a slight reduction in the reflection (red), and in the absorption in the ITO layer (magenta). For this optimized patterned ITO geometry, the AM1.5-spectrum-averaged absorption is the same as for the patterned cell on Mo (61%). At the same time, the main losses in this optimized ITO geometry are due to reflection, which is similar as for a patterned Mo cell (11% averaged over the AM1.5 spectrum), and transmission rather than parasitic absorption as is the case for the Mo cells. This is an important result and makes the ITO-based patterned ultrathin CIGSe cells interesting candidates for the top cell in a series-connected multi-junction geometry, provided that wider band gap CIGSe cells have to be used in this geometry.

8.4 Conclusion

We have fabricated dielectric scattering patterns on the front and back side of ultra-thin CIGSe solar cells with absorber layer thicknesses of 460 nm. We showed that printing arrays of TiO_2 nanoparticles at the front side of completed CIGSe solar cells does not significantly increase carrier recombination. These particles do result in a photocurrent enhancement in the 550 nm to 950 nm spectral range, which is mostly due to an anti-reflection effect caused by preferential forward scattering of light. Exploring different array geometries showed that using TiO_2 particles on the front side can result in light trapping, but this comes at the expense of the total absorption enhancement. We demonstrated that efficient light trapping can be achieved in these cells by using array of SiO_2 particles at the Mo/CIGSe interface. This leads to efficient light trapping and does not deteriorate, and maybe even improves, the carrier recombination properties of the device, resulting in a significant cell efficiency increase from 11.0% to 12.4%. Whereas the dielectric scatterers lead to a substantial reduction of the absorption in the Mo back contact, absorption in this layer is still a significant loss factor. This can be avoided in a geometry in which cells are grown on SiO_2 nanopatterned ITO, making these cells interesting candidates for series-connected multi-junction geometries.

9

Optimizing power spectral density of light trapping patterns

In this chapter we study the relation between the power spectral density (PSD) of scattering patterns and their performance in terms of light trapping. We calculate the dispersion relations for waveguide modes in two types of model systems, ultra-thin a-Si:H cells and a-Si:H cells with standard thickness, and use them to define the required spatial frequency band for light trapping. We use a Monte Carlo algorithm to optimize the PSD of a random array of Mie scatterers on top of a-Si:H cells. The optimized particle array has a PSD that is larger in the desired spatial frequency range than the PSD of a random array and contains contributions at more spatial frequencies than the PSD of a periodic array. Three-dimensional finite-difference time-domain simulations on thin-film solar cells with the different light trapping patterns show that the optimized particle array results in more efficient light trapping than a random array of Mie scatterers. However it does not outperform an optimized periodic geometry. We use the same approach to design a random texture with a maximum height similar to the Asahi-U type pattern and compare light trapping with both patterns in thin-film solar cells. We show that the optimized pattern leads to 28% improvement with respect to Asahi-U type in the 550 to 800 nm spectral range and also outperforms an optimized periodic scattering pattern. Since these light trapping patterns do not require patterning of the active layer and they can be tuned for specific spatial frequency ranges, this concept is applicable to all types of thin-film solar cells.

9.1 Introduction

In previous chapters we have studied light trapping with metallic and dielectric scattering patterns. Most of these patterns were periodic arrays of resonant scatterers, which we compared to the random Asahi-U type texture in the case of a-Si:H solar cells. Multiple papers compare random and periodic light trapping patterns [47, 84, 127, 146–150]. The diffractive properties of the scattering pattern depend on its power spectral density (PSD), which is the spatial Fourier transform of the scattering pattern. Periodic patterns have a very large power spectral density at the spatial frequency that corresponds to the array periodicity, but their PSD spectra only consist of very few peaks. To obtain broadband light trapping, a broader distribution of spatial frequencies is required. Random patterns contain a broad distribution of spatial frequencies. However, for each spatial frequency the PSD is much lower than the PSD of the periodic pattern at the spatial frequency that corresponds to the array pitch. Furthermore, random patterns do not have all of their peaks in PSD in the spatial frequency range that is required for waveguide mode coupling. In Chapter 3 we have already seen the correlation between the photocurrent and the power spectral density for different periodic, random and quasi-random patterns.

Quasi-random patterns have a broader distribution of spatial frequencies than periodic patterns and have peaks with higher PSD than random patterns. However, their distribution of spatial frequencies can not be tailored to maximize overlap with a specified set of waveguide modes. From Parseval's theorem we know it is not possible to enhance the PSD at all spatial frequencies simultaneously [151], but the possibility exists to enhance the PSD in the range of spatial frequencies required to couple to waveguide modes by reducing it outside this region.

Other groups have demonstrated the possibility to design light trapping patterns that contain optimized spatial frequency spectra [121, 152, 153]. In this chapter we study the spatial frequencies in dielectric scattering patterns and relate them to the waveguide modes of thin-film solar cells. We present the optimization of state of the art light trapping patterns in realistic solar cell geometries and relate peaks in simulated absorption enhancement to spatial frequencies in the scattering patterns. The patterns either consist of textured TCO or arrays of dielectric resonant scatterers. Since they do not require patterning of the absorber layer, these light trapping patterns are applicable to all thin-film solar cell geometries.

9.2 Results

We apply the patterns we study in this chapter to thin-film a-Si:H solar cells. Because of the high refractive index of a-Si:H, light is very well confined in the waveguide layer. Figure 9.1 shows the dispersion relations of the waveguide

modes of two cell geometries considered in this chapter. The modes were calculated using a mode solving code that finds the solutions for Maxwell's equations based on the transfer matrix method [154, 155]. Both geometries consist of a stack of Ag, Al-doped ZnO (AZO), a-Si:H, and ITO, schematically shown as insets in Figure 9.1a and b.

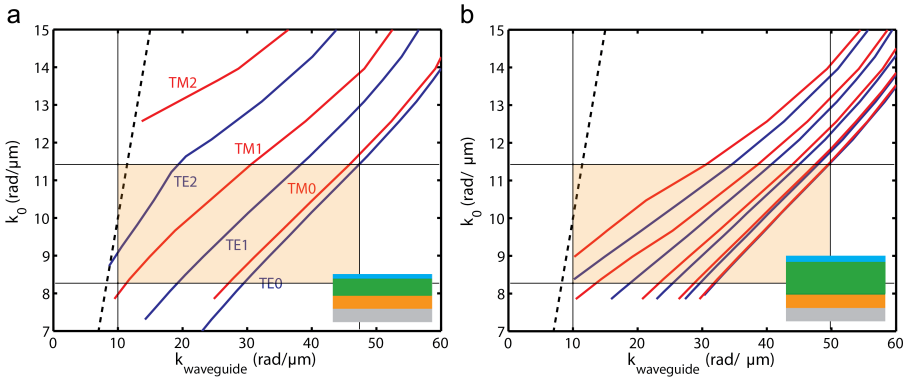

Figure 9.1: Dispersion relations for TE (blue) and TM (red) waveguide modes in thin-film a-Si:H solar cells with i-layer thickness of (a) 145 nm and (b) 350 nm. Insets show the device geometry with all different layers: Ag (grey), Al-doped ZnO (AZO) (orange), a-Si:H (green), and ITO (cyan). The black horizontal lines in (a) and (b) indicate the incident spectral band for which waveguide mode coupling is required. The orange shaded areas depict the overlap between this spectral band and the waveguide modes; the vertical black lines show the corresponding range of spatial frequencies that is required for light trapping.

In Figure 9.1a the a-Si:H layer has a thickness of 145 nm. This geometry supports only six waveguide modes in the absorber layer, 3 TE modes (blue) and 3 TM modes (red). The black dashed line shows the light line in air. All modes are located to the right of the light line, meaning that they are purely bound and cannot couple to free space radiation. The horizontal black lines in this figure indicate the incident wavelength range for which light trapping is required, which is 550–800 nm. To achieve light trapping, this spectral band needs to be coupled to waveguide modes. The lower bound of the spatial frequency range that is required for light trapping is given by the light line in air. For this value we take the spatial frequency corresponding to the light line in the center of the incident spectral band that needs to be trapped in the absorber layer, which corresponds to a spatial frequency of 10 rad/μm, or an inverse wavelength of 1.6 μm^{-1}. The upper limit of the required spatial frequency range corresponds to the spatial frequency for which the lowest order mode still overlaps with the incident spectral band; this is 47.1 rad/μm (7.4 μm^{-1}). In the geometry in Figure 9.1b the a-Si:H layer is 350 nm (corresponding to the thickness of the cells in Chapter 4, 5, and 7). The thicker absorber layer in this geometry supports more waveguide modes than the thin layer in Figure 9.1a. Light trapping is

required between 550 nm and 800 nm, which means that spatial frequencies between 10 rad/µm and 49.7 rad/µm (1.6 μm^{-1} and 7.9 μm^{-1}) are required, quite similar to the required spatial frequency range for the 145 nm thick cell.

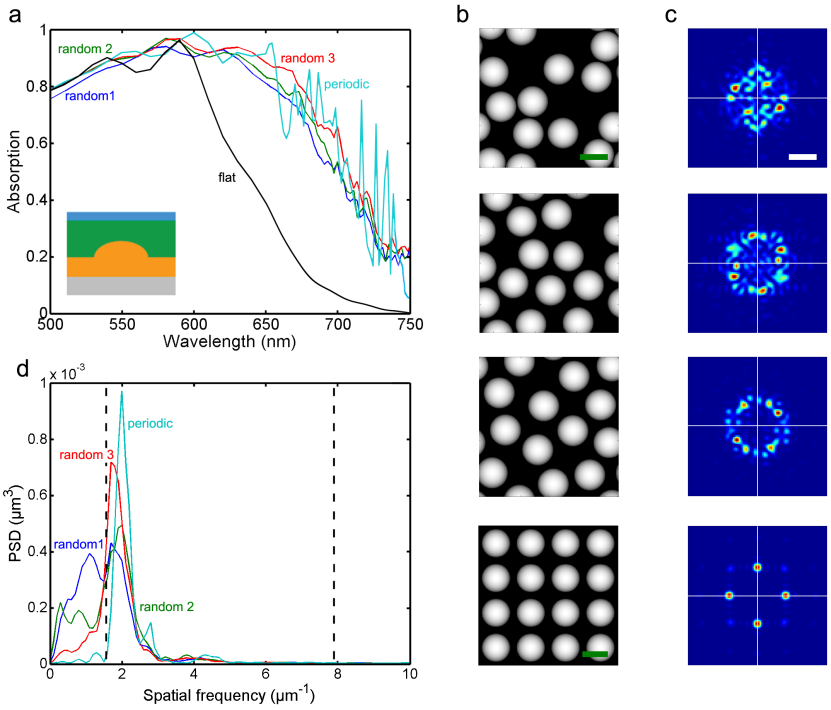

Figure 9.2: (a) Simulated absorption in 350 nm a-Si:H solar cells with arrays of AZO hemispheres with r=225 nm at the a-Si:H AZO interface. Results are shown for a flat cell (black), periodically patterned cell (cyan), and randomly placed particles in a 4 µm unit cell with a minimum particle spacing of 450 nm (blue), 500 nm (green), and 540 nm (red). (b) Different particle arrays used in the simulation, from top to bottom: 2×2 μm^2 box with random arrays with minimum center-to-center distance of 450 nm, 500 nm, and 540 nm, and 2×2 μm^2 box with periodic array. The scale bar in the top figure corresponds to 400 nm and indicates the scale for the first three configurations. The scale bar in the periodic array indicates 440 nm.(c) 2D PSD spectra of particle arrays shown in (b). The scale bar indicates 2 μm^{-1}. (d) $PSD(f_r)$ for the different geometries shown in (b). The horizontal and vertical white lines indicate the axes through the origin. Data are shown for a periodic particle array (cyan) and random particle arrays with minimum center-to-center distance of 450 nm (blue), 500 nm (green), and 540 nm (red). The vertical dashed lines indicate the minimum and maximum spatial frequencies required for light trapping.

Three-dimensional finite-difference time-domain (FDTD) simulations were used to calculate the absorption of normal-incident light in the active layer of the solar cell stack of Figure 9.1b. A 5 nm mesh was used over the entire simulation volume. Perfectly matched layers (PMLs) were used at the top and bottom of the simulation volume and periodic boundary conditions were used in

x and y direction. Figure 9.2 shows the result for cells with different arrays of AZO particles at the AZO/a-Si:H interface (see inset) and a flat reference cell (black). All geometries have similar particle size and density corresponding to an (average) array pitch of 550 nm. The periodic array (cyan) results in the highest absorption and has sharp peaks, which are signatures of waveguide-mode coupling. The red, blue and green lines are simulations for 4×4 μm^2 unit cells with different random particle arrays. They show a continuous enhancement rather than distinct peaks, due to the random geometry of the unit cell. The blue line shows the most random configuration (top geometry in Figure 9.2b). This configuration is obtained by placing particles in the unit cell at positions determined by a random number generator with the restriction that overlap is not allowed. To obtain the other configurations a local search algorithm is used to find a configuration in which all particles have a minimum center-to-center distance of 500 nm (second geometry in Figure 9.2b) or 540 nm (third geometry in Figure 9.2b). In the local search algorithm a particle is selected randomly and then moved with a randomly chosen step size and angle. Increasing the minimum center-to-center distance, increases the amount of order in the array geometry. Compared to the random geometry, the absorption in the a-Si:H layer, shown in Figure 9.2a, is enhanced for the more ordered geometry with 500 nm center-to-center distance (green) and further enhanced for the geometry with the 540 nm center-to-center distance (red). This trend is reproducible for different random initializations and unit cell sizes (not shown).

Figure 9.2c shows the PSD of the four different patterns, defined by

$$PSD(f_\mathrm{x}, f_\mathrm{y}) \equiv \frac{1}{L^2} \sum_\mathrm{n} \sum_\mathrm{m} \left[h_\mathrm{mn} e^{-2\pi i \Delta L (f_\mathrm{x} n + f_\mathrm{y} m)} \Delta L^2 \right]^2$$

where f_x, f_y are the spatial frequencies in x and y direction respectively, L is the length of the pattern, h_mn is the height at position m, n, and ΔL is the pixel size in the height map [156]. The most random pattern shows a filled circle with a broad distribution of spatial frequencies. A large fraction of the total PSD is at spatial frequencies that are to the left of the light line and thus not useful for mode coupling. Increasing the order by increasing the minimum distance results in a reduction of PSD at low frequencies; the PSD changes from a circle into a ring. The periodic pattern shows distinct peaks at spatial frequencies corresponding to the inverse array pitch. Figure 9.2d shows $PSD(f_\mathrm{r})$, with $f_\mathrm{r}^2 = f_\mathrm{x}^2 + f_\mathrm{y}^2$, for the different patterns. The periodic patterns shows a sharp peak at 1.8 μm^{-1}, corresponding to the (0,1) diffraction order in the array, and a second peak at 2.6 μm^{-1}, corresponding to the (1,1) diffraction order. Higher order peaks are observed at larger spatial frequencies at very small intensity. The intensity of these peaks is low because the form factor, which is the spatial Fourier transform of the particle shape, has low intensity at these frequencies. The finite width of the peaks is due to the finite size of the pattern. The peaks would be δ-functions in the case of an infinite array size. Compared to the random patterns, the periodic pattern has an overall higher PSD at frequencies

above 1.6 μm^{-1}. This leads to more efficient mode-coupling, and hence overall higher simulated absorption spectrum. Increasing the order in the random pattern (blue to green to red) results in a higher PSD above 1.6 μm^{-1}, which is in the range useful for mode-coupling. This is in agreement with the trend in simulated absorption that also shows increasing absorption in the red spectral range with increasing order of the light trapping pattern.

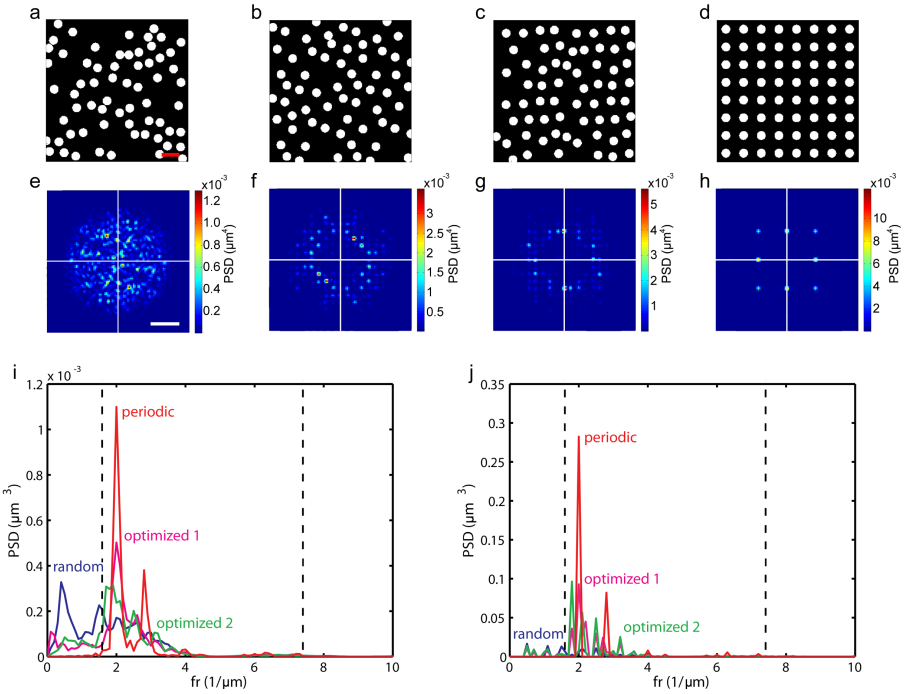

Figure 9.3: (a-d) Particle arrays in 4×4 μm^2 box. Different array geometries are shown: a random array (a), two different optimized arrays (b,c), and a periodic array (d). The scale bar indicates 800 nm. (e-h) Corresponding 2D PSD spectra. The scale bar in these images corresponds to 2 μm^{-1} and the horizontal and vertical white lines indicate the axes through the origin. $PSD(f_r)$ is shown for (i) a single box with particles and (j) including periodic boundaries for periodic (red), random (blue) optimized 1 (magenta), and optimized 2 (green) array geometries. The vertical dashed lines in (i) and (j) indicate the minimum and maximum spatial frequencies required for light trapping.

To have more control over the PSD of the scattering pattern, we optimize a random scattering pattern using a Monte Carlo algorithm. The initial configuration consist of a random or periodic array of cylinders with radius 125 nm, height 200 nm, and average pitch 500 nm. This radius, height and pitch correspond to an optimized periodic geometry as shown in Chapter 7. In each optimization cycle a particle is randomly selected, and subsequently moved with a randomly

chosen distance and angle. A widely varying step size between 1 nm and 700 nm is chosen in order to explore a large number of configurations. A random number generator with a long period is used to avoid ending up in local maxima too easily [157]. If a particle move results in an enhanced PSD it is accepted, otherwise it is rejected. The particle size and density are kept constant during the optimization. Different relatively small unit cell sizes of 2×2 μm^2 and 4×4 μm^2 are explored in combination with periodic boundary conditions. This gives a periodic pattern with a large unit cell that enables us to engineer the spatial frequency distribution. These unit cell sizes are chosen in order to have configurations that can be tested with three-dimensional FDTD simulations. We find that 4×4 μm^2 unit cells result in larger differences after optimization due to the larger number of degrees of freedom.

Figure 9.3 shows a random (a), two different optimized, referred to as optimized 1 and optimized 2 (b,c), and a periodic array geometry (d) with their corresponding 2D PSD spectra (e-h). The two different optimized configurations are generated using different random initializations. Since the particles are smaller than in the array geometry in Figure 9.2, they can have smaller center-to-center distances without overlapping, which means that also larger spatial frequencies can be present. Therefore the PSD of the random array (e) shows a broader distribution of spatial frequencies than the PSD of the random array in Figure 9.2c. The optimized array geometries show more order than the random geometry, which is also visible in the corresponding PSD spectra. The PSD at frequencies around zero is significantly reduced and the PSD at frequencies above the light line is enhanced. The response of the optimized patterns is not isotropic, Figure 9.3b shows 4 peaks close to one of the diagonals and Figure 9.3c shows two peaks with higher intensity than the peaks in Figure 9.3b at $f_x = 0$. At frequencies above 4 μm^{-1}, no substantial enhancement in PSD is observed after the optimization. This is due to the restriction that the particles are not allowed to overlap. Figure 9.3d shows the periodic geometry with similar particle size and density as the geometries in Figure 9.3a-c. The PSD of the periodic pattern (Figure 9.3h) shows higher peaks than the PSD of the optimized random array geometries. Figure 9.3i shows $PSD(f_r)$ for the four different array geometries. The vertical dashed lines indicate the range of spatial frequencies that overlaps with the waveguide modes in 550–800 nm incident spectral range. The difference in PSD at frequencies below the light line (1.6 μm^{-1}) for the different patterns is clearly visible. The random pattern (blue) has a large fraction of its PSD at frequencies that are too low for coupling to bound waveguide modes. The PSD of the optimized patterns (green, magenta) is significantly reduced at these frequencies, but it is still larger than zero. The periodic pattern (red) only shows PSD at frequencies above the light line and the peaks at 2.0 μm^{-1} and 2.8 μm^{-1} are much larger than the peaks in the PSD of the optimized pattern. In contrast, the PSD of the optimized patterns contains a broad distribution of spatial frequencies above the light line.

The unit cells we optimized have a size of only 4×4 μm^2. In order to use them

as a light trapping geometry in a FDTD simulation, the unit cells were combined with periodic boundary conditions. This was done by replicating the box in x and y direction. This also influences the PSD of the light trapping patterns. The PSD of the patterns in combination with periodic boundary conditions (for 25 replications of the unit cell) is shown in Figure 9.3j. The periodic boundaries lead to changed PSD spectra compared to the spectra for a single unit cell in Figure 9.3i. The periodic pattern (red) shows narrower peaks than in 9.3i; increasing the box size to infinity would lead to δ-functions at the spatial frequencies corresponding to the array pitch. The random and optimized random patterns (blue, green, magenta) show multiple narrow peaks that correspond to the periodicity. Comparing PSD for the different patterns shows similar trends as in Figure 9.3i. The random (blue) pattern has a low PSD in the frequency range of interest. The PSD is substantially larger for the optimized patterns (green, magenta), and even larger for the periodic pattern. At spatial frequencies between 3.0 μm^{-1} and 3.9 μm^{-1} all random patterns have a larger PSD than the periodic pattern.

To demonstrate the influence of the PSD of the scattering pattern on the absorption enhancement of the solar cell, Figure 9.4 shows the dispersion relations of the waveguide modes in the thin-film stack (a), together with the power spectral density of the scattering patterns (b), and the simulated absorption in the a-Si:H layer (c) of the solar cell geometry shown in (d). The cell geometry consists of 200 nm Ag (grey), 130 nm AZO (orange), 145 nm a-Si:H (green), 80 nm ITO and an array of TiO_2 particles (brown) with radius 125 nm, height 200 nm, and (average) pitch of 500 nm. Figure 9.4 depicts this relation between PSD and light trapping for the periodic scattering pattern (red). The red semitransparent vertical lines through the PSD spectrum and the dispersion relations of the modes connect the spatial frequencies in the PSD spectrum of the periodic pattern to the waveguide modes. Intersections between these lines and waveguide modes present incident wavelengths at which mode-coupling is possible for the periodically patterned cell, indicated by horizontal red semitransparent lines. Intersections between waveguide modes and peaks in the PSD spectrum that result in peaks in the simulated absorption spectrum are marked with black circles. The absorption enhancement for the periodically patterned cell shows a broad peak between 610 nm and 650 nm. The reason why this peak is so broad is twofold. First, in this incident spectral band there are multiple crossings between the PSD and waveguide modes. The highest peaks in the PSD spectrum at 2 μm^{-1} with the TE_2 mode, the peak at 4.5 μm^{-1} intersects with the TE_1 mode, and the peak at 6.4 μm^{-1} intersects with the TE_0 and the TM_0 modes. Second, in this spectral range absorption in the a-Si:H layer is still quite strong, which causes an uncertainty in the wavevector of the waveguide modes. Another broad peak is observed in the simulated absorption at 585 nm. This peak is attributed to coupling to the TE_2 mode by the peak in the PSD spectrum at 2.8 μm^{-1}.

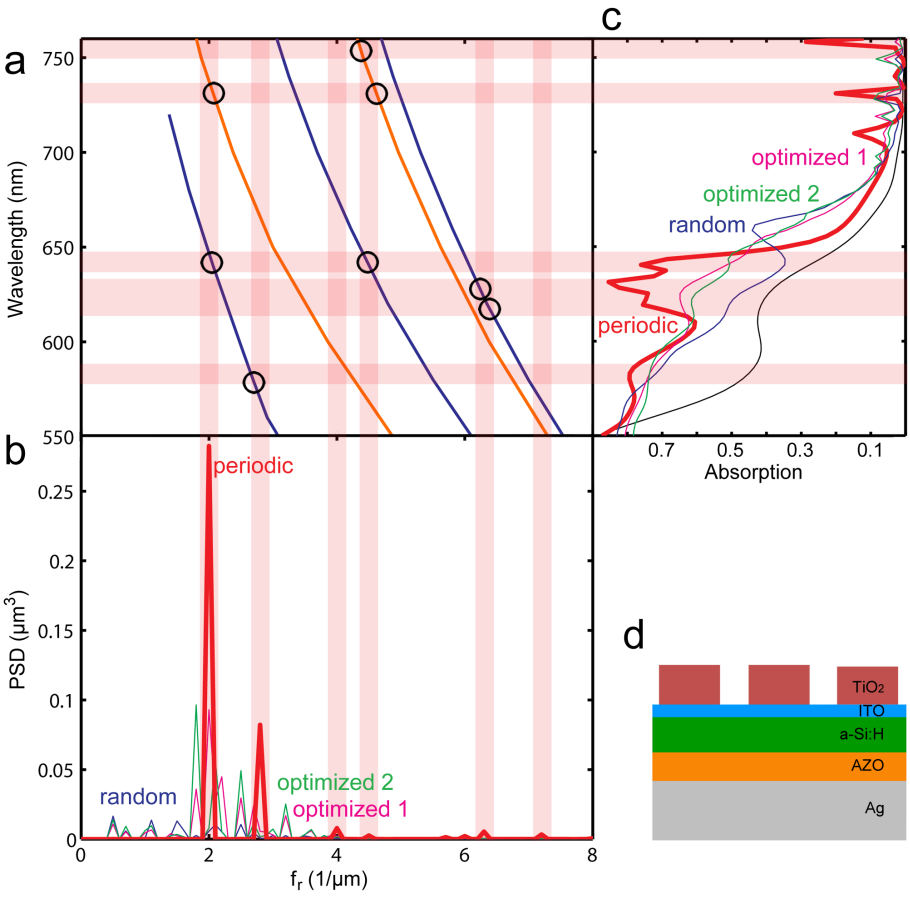

Figure 9.4: (a) Dispersion relations for TE (blue) and TM (red) waveguide modes in 145 nm a-Si:H cell. (b) $PSD(f_r)$ for periodic (red), random (blue), and optimized (green, magenta) array geometries. (c) Simulated absorption in thin-film a-Si:H cells with different scattering patterns. Data is shown for cells with periodic (red), random (blue) and optimized (green, magenta) array geometries. (d) Schematic cross section of the cell geometry, consisting of Ag (grey), AZO (orange), a-Si:H (green) ITO (cyan), and TiO_2 (brown). The semitransparent red vertical lines in (a) and (b) relate the peaks in the PSD of the periodic pattern to the waveguide modes and show at which incident wavelengths mode-coupling is possible. These incident wavelengths are indicated by the horizontal semitransparent red lines. Black circles in (a) indicate intersections between peaks in PSD and waveguide modes at wavelengths for which peaks in simulated absorption are observed.

At wavelengths of 730 nm and 760 nm, two distinct peaks are observed in the simulated absorption spectrum. At these wavelengths, the absorption in the a-Si:H layer is very weak, which leads to more well-defined wavevectors of the waveguide modes than at lower wavelengths, and hence to narrower peaks in the absorption spectrum. The peaks at 730 nm and 760 nm correspond to

coupling to the TE_1 and the TM_0 mode, respectively. The small peak at 710 nm can not be related to mode-coupling and it was found that this peak depends on the particle radius.

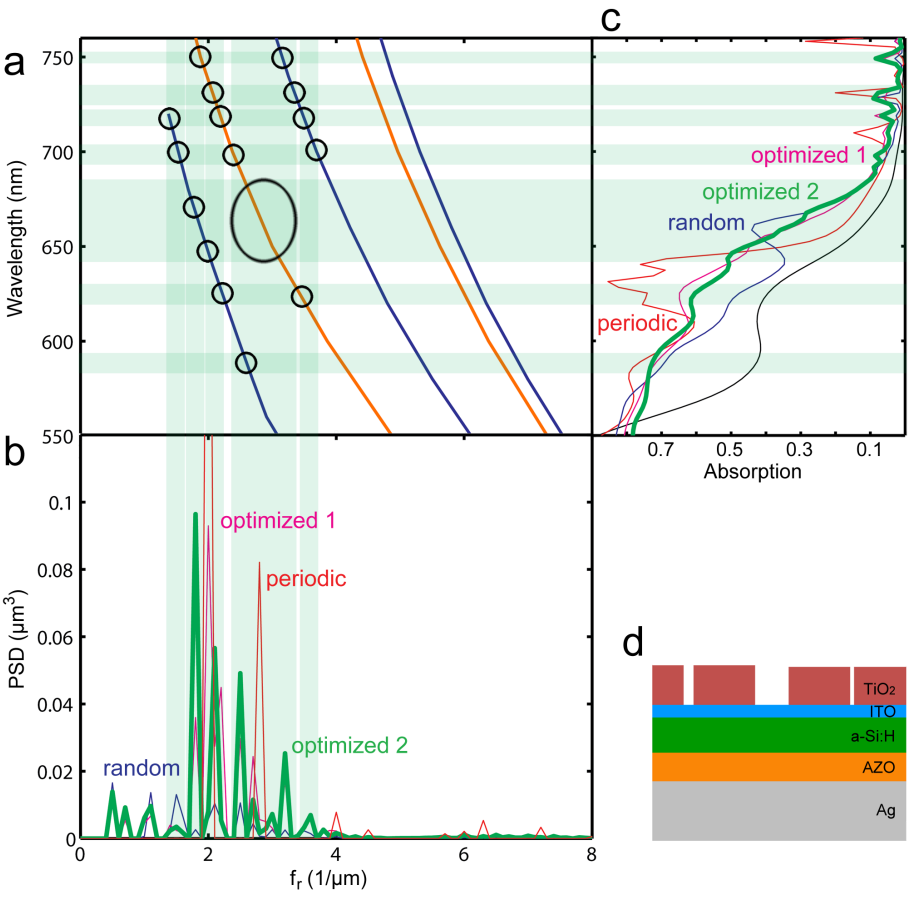

Figure 9.5: (a) Dispersion relations for TE (blue) and TM (red) waveguide modes in 145 nm a-Si:H cell. (b) $PSD(f_r)$ for optimized 2 (green), periodic (red), random (blue), and optimized 1 (magenta) array geometries. (c) Simulated absorption in thin-film a-Si:H cells with different scattering patterns. Data is shown for cells with periodic (red), random (blue) and optimized (green, magenta) array geometries. (d) Schematic cross section of the cell geometry, consisting of Ag (grey), AZO (orange), a-Si:H (green) ITO (cyan), and TiO_2 (brown). The semitransparent green vertical lines in (a) and (b) relate the peaks in the PSD of the periodic pattern to the waveguide modes and show at which incident wavelengths mode-coupling is possible. These incident wavelengths are indicated by the horizontal semitransparent green lines. Black circles in (a) indicate intersections between peaks in PSD and waveguide modes at wavelengths for which peaks in simulated absorption are observed.

Similar to the light trapping shown in Figure 9.4 for the periodic scattering pattern, Figure 9.5 shows the waveguide-mode coupling for the pattern 'optimized 2' (green), which is the optimized pattern shown in Figure 9.3c. Of the two optimized patterns, this one has a PSD spectrum that is most different from the PSD of the periodic pattern. The PSD spectrum of the optimized pattern shows a broad distribution of spatial frequencies compared to the periodic pattern. All peaks in the PSD spectrum are substantially lower than the peak at 2 μm^{-1} in the PSD spectrum of the periodic pattern, which leads to the absence of very distinct peaks in the simulated absorption spectrum (Figure 9.5c). Many intersections between relatively small peaks in the PSD spectrum and waveguide modes are observed. The contribution of all of these intersections leads to a broadband enhancement in the simulated absorption. At wavelengths between 645 nm and 680 nm the simulated absorption in the cell with the optimized pattern exceeds the absorption in the cell with the periodic pattern, which is due to the multiple peaks in PSD between 2.4 μm^{-1} and 3.3 μm^{-1}. The availability of multiple Fourier components in combinations with the strong absorption in this spectral range causes broadband light trapping. The simulated absorption for the optimized geometry also contains the broad peak between 610 nm and 650 nm that is observed for the periodic pattern. However the absorption is lower in this spectral range for the optimized pattern. We attribute this to the lack of the large peak at 2 μm^{-1} that is present in the PSD of the periodic pattern. Overall the optimized pattern results in lower simulated absorption than the periodic pattern, but it performs significantly better than the random pattern (blue). The improvement with respect to the random pattern is consistent with the increased PSD spectrum after the optimization. The other optimized pattern, optimized 1, shows overall somewhat higher absorption than optimized 2.

9.3 Optimization of random textures

Due to the size, shape, and non-overlap restrictions of the array of Mie scatterers, there is limited flexibility in the PSD spectra that can be obtained by optimization. This limitation is particularly found when trying to enhance the PSD at larger spatial frequencies, which overlap with the lower order waveguide modes. In order to design a scattering pattern with a more tunable PSD we optimize a random texture. Our starting configuration is a 2×2 μm^2 AFM scan (512×512 pixels) of the Asahi-U type pattern, the commercial light trapping standard for thin-film Si solar cells. We use a Monte Carlo algorithm to find a configuration with the same maximum height, but an enhanced PSD in the spatial frequency range between 1.6 μm^{-1} and 7.9 μm^{-1}. The optimization algorithm randomly selects a rectangle in the height map with a size between 15 and 30 pixels. Subsequently a height step, Δh, between −50 nm and 50 nm, is chosen randomly. Each pixel in the selected rectangle, except for the outer

5 rows ("edge pixels"), has a probability of 80% to be changed with this height step, and thus a probability of 20% to not be changed. As a result, a certain pattern in the selected rectangle will be shifted by the height step. The edge pixels in the rectangle and all pixels adjacent to height-shifted pixels, will be shifted by 0.5 Δh in order to make a pattern with smooth transitions in height. If the height change of the randomly chosen shape results in a PSD increase and if the new pattern does not exceed the maximum height, the new configuration is accepted, otherwise it is rejected. Figure 9.6 summarizes the results of the random texture optimization. Figure 9.6a shows the height map of the Asahi-U type pattern and its corresponding 2D PSD spectrum. This pattern contains a very broad range of spatial frequencies and many of them are too low or too high in order to be useful for mode-coupling in the cell geometries discussed in this chapter. Figure 9.6b shows the height map and PSD for a texture that is optimized in the spatial frequency range required to couple to the waveguide modes, which is between 1.6 μm^{-1} and 7.9 μm^{-1}. The overall feature size is larger than in the Asahi texture and the 2D PSD shows a more ordered geometry, in which the PSD in the useful spatial frequency range is strongly enhanced with respect to the PSD outside this range. To demonstrate that this concept can easily be applied to tailor a pattern for a specific frequency range, Figure 9.6c shows the optimization for a frequency range between 1.6 μm^{-1} and 4.4 μm^{-1}, which results in an overall larger feature size than in Figure 9.6a and 6b and a large PSD in this low frequency ring. Similarly, the geometry in Figure 9.6d is optimized spatial frequency range between 4.4 μm^{-1} and 7.4 μm^{-1}, which mostly overlaps with the TM_0 and the TE_0 modes in Figure 9.1a. This texture contains smaller features than the texture in Figure 9.6a and the PSD spectrum shows a ring in the desired frequency range.

Figure 9.7 shows $PSD(f_r)$ for the different light trapping textures. All optimized patterns (green, red, magenta) show significantly higher PSD in this spatial frequency range than the Asahi pattern (blue). Comparing the PSD of the optimized pattern clearly demonstrates how well a patterns can be optimized to only have elevated PSD in a certain spatial frequency range. Of the optimized patterns, 'opt 2' has the the largest PSD integrated over the spatial frequency range from 1.6–7.9 μm^{-1}. Figure 9.7b depicts the simulated absorption in the solar cell type described in Figure 9.1b, with patterned AZO layers, using the different textures shown in Figure 9.6, compared to a flat solar cell (black line). The absorption for the flat cell (black) decays rapidly in this wavelength range. The Asahi pattern (blue) results in enhanced absorption with respect to the flat cell, but the different optimized patterns (magenta, green, red) perform substantially better. Of these patterns 'opt 2' (magenta), which is optimized for spatial frequencies between 1.6 μm^{-1} and 4.4 μm^{-1}, shows the largest absorption enhancement, consistent with its large PSD in the spatial frequency range that overlaps with the waveguide modes. Light trapping with the patterns 'opt 1' and 'opt 2' is even larger than for the periodic pattern (cyan). The pattern that is optimized to have a large PSD at frequencies between 4.4 and 7.9 μm^{-1},

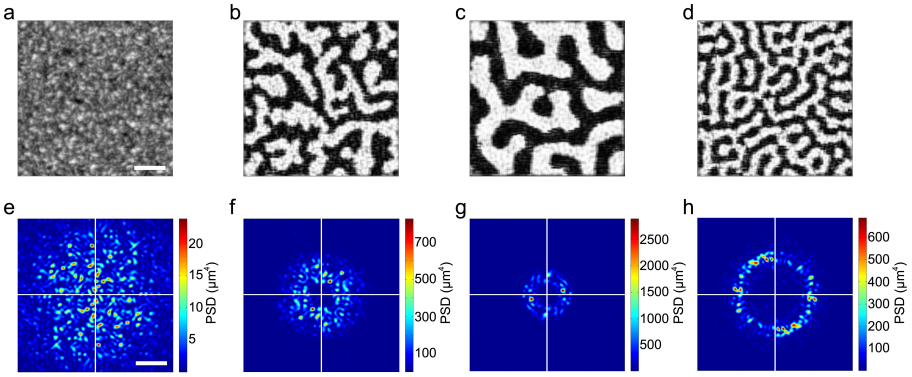

Figure 9.6: (a-d) Height maps for different textures with maximum height 250 nm. The scale bar indicates 400 nm. (a) Asahi-U type, textures optimized for PSD enhancement between (b) 1.6 μm^{-1} and 7.9 μm^{-1}, (c) 1.6 μm^{-1} and 4.4 μm^{-1}, and (d) 4.4 μm^{-1} and 7.9 μm^{-1}. (e-h) 2D PSD spectra corresponding to textures in (a-d). The scale bar indicates 4 μm^{-1} and the horizontal and vertical white lines indicate the axes through the origin.

results in somewhat lower light trapping than the other two optimized patterns. This pattern also shows a lower integrated PSD in the desired frequency range.

Texture	RMS roughness (nm)
Asahi-U	35
opt 1	98
opt 2	103
opt 3	93

Table 9.1: Light trapping textures shown in Figure 9.6a–d with corresponding RMS roughnesses.

Whereas in the optimization of the particle array the particles were moved which resulted in a constant volume of scatterers, in the case of the texture optimization the volume of scatterers is not conserved. Therefore, also the total PSD is not conserved in the optimization. Compared to the Asahi-U type pattern, the optimized textures have a substantially larger PSD is this spatial frequency range. This is due to increased contrast in the height profile. For the Asahi-U type pattern (Figure 9.6a) most points in the height map are close to the mean value, while the optimized textures (Figure 9.6b-d) have many points in their height profile that are close to 0 or to the maximum height. Table 9.1 shows the RMS roughness for the different textures. The Asahi-U type texture has a RMS roughness of 35 nm and all three optimized textures show a substantially higher RMS roughness. Also, the different optimized scattering patterns show

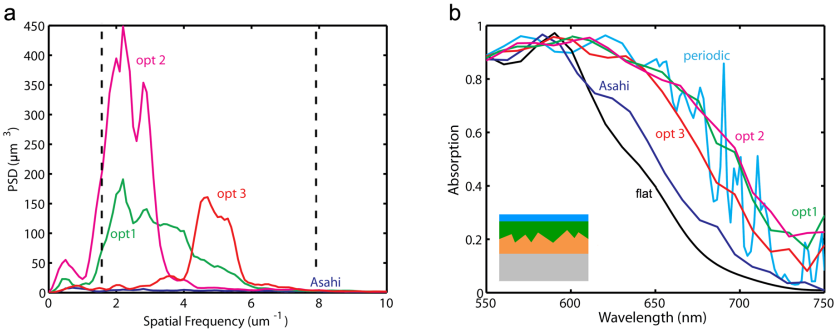

Figure 9.7: (a) $PSD(f_r)$ for the different textures shown in Figure 9.6. Data is shown for Asahi (blue), opt 1, optimized for spatial frequencies 1.6 $\mu m^{-1} < f_r < 7.6\ \mu m^{-1}$, (green), opt 2, optimized for 1.6 $\mu m^{-1} < f_r < 4.4\ \mu m^{-1}$, (magenta), and opt 3, optimized for 4.4 $\mu m^{-1} < f_r < 7.6\ \mu m^{-1}$ (red). The vertical dashed lines indicate the minimum and maximum spatial frequencies required for light trapping. (b) Simulated absorption in the a-Si:H layer of 350 nm a-Si:H cells with different textures at the a-Si:H/AZO interface. Data are shown for flat (black) and periodically patterned (cyan) cells, and cells with textures Asahi-U type (blue), opt 1 (green), opt 2 (magenta), and opt 3 (red). The inset shows a schematic cross section of the device geometry, consisting of Ag (grey), AZO (orange), a-Si:H (green) and ITO (cyan).

different RMS roughnesses. Opt 2, which is optimized for spatial frequencies of 1.6–4.4 μm^{-1} has the highest RMS roughness, indicating most contrast. This pattern also also has the highest PSD (Figure 9.7a) and results in the most efficient light trapping (Figure 9.7b) of the three patterns.

9.4 Light trapping patterns and transverse coherence length of sunlight

The sun is a partially coherent source of light. For the design of light trapping patterns it is important to take into account the transverse coherence length of sunlight. When looking at a cross section of a beam of light, the transverse coherence length is defined as the length over which the phase is correlated; light scattered from two points that are spaced by this distance will exhibit interference [158]. If the separation between two scatterers exceeds the transverse coherence length, they will scatter independently. In this chapter we have seen that whereas the antireflection effect due to surface nanostructures in the blue spectral range mostly depends on the properties of single scatterers, the light trapping is determined by the spatial frequencies in the scattering pattern. The light trapping patterns designed in this chapter show optimized spatial frequency spectra for box sizes of only 2 μm to 4 μm. For direct sunlight the transverse coherence length is of the order of 100 μm [159]; it depends on the

ratio of the square of the wavelength of the light to the solid angle that the sun subtends on earth. This value of the coherence length for sunlight is far beyond the size of our light trapping patterns, so that the analysis described in this thesis is applicable. For indirect sunlight, the transverse coherence length is decreased and further work is required to study this in more detail [160].

9.5 Conclusion

In this chapter we demonstrated the relation between the PSD of scattering patterns and their performance in terms of light trapping. We calculated the dispersion relations for waveguide modes in two different light trapping geometries and use them to define the required spatial frequency range for light trapping. Using a Monte Carlo algorithm, we optimized random arrays of Mie scatterers in order to have increased PSD in this spatial frequency range while maintaining particle size and density. The optimized patterns show an elevated PSD in the spatial-frequency range of interest with respect to a random pattern and also result in more light trapping. However, an optimized periodic light trapping pattern still outperforms this optimized random particle arrays. In order to have more flexibility in the optimization of light trapping patterns, we optimize a random texture composed of smaller-size scatterers. We show that these optimized textures do have the ability to outperform optimized periodic particle arrays. We demonstrate the robustness of this approach by showing that the optimization can be used to specifically enhance PSD in different ranges of spatial frequencies. Because of this, and since the light trapping pattern does not require patterning of the active layer, this concept is applicable to all types of thin-film solar cells.

References

[1] B. Podobnik, *Global Energy Shifts: Fostering Sustainability in a Turbulent Age*, Temple University Press, 2008.

[2] U.S. Energy Information Administration, *International Energy Outlook 2013*, `http://www.eia.gov/forecasts/ieo/world.cfm`.

[3] M. van der Hoeven, *World Energy Outlook 2012*, Technical report, International Energy Agency, 2012.

[4] J. Perlin, *From Space to Earth, The Story of Solar Electricity*, Harvard University Press, 2002.

[5] M. A. Green, K. Emery, Y. Hishikawa, W. Warta, and E. D. Dunlop, *Solar cell efficiency tables*, Prog. Photovolt: Res. Appl. **22**, 701 (2014).

[6] A. Jäger-Waldau, *PV Status Report 2013*, Technical report, European Commission, DG Joint Research Centre, Institute for Energy and Transport, Renewable Energy Unit, 2013.

[7] W. Shockley and H. J. Queisser, *Detailed Balance Limit of Efficiency of pn Junction Solar Cells*, Journ. Appl. Physics **32**, 510 (1961).

[8] J. Meier, S. Dubail, R. Platz, P. Torres, U. Kroll, J. A. A. Selvan, N. P. Vaucher, C. Hof, D. F. F. Keppner, R. Flückiger, A. Shah, V. Shklover, and K. D. Ufert, *Towards high-efficiency thin-film silicon solar cells with the 'micromorph' concept*, Sol. Energy Mat. and Sol. Cells **49**, 35 (1997).

[9] J. Yang, A. Banerjee, and S. Guha, *Triple-junction amorphous silicon alloy solar cell with 14.6% initial and 13.0% stable conversion efficiencies*, Appl. Phys. Lett. **70**, 2975 (1997).

[10] R. T. Ross and A. J. Nozik, *Efficiency of hot-carrier solar energy converters*, Journ. Appl. Physics **53**, 3813 (1982).

[11] A. L. Bris and J. F. Guillemoles, *Hot carrier solar cells: Achievable efficiency accounting for heat losses in the absorber and through contacts*, Appl. Phys. Lett. **97**, 113506 (2010).

[12] A. Luque and A. Martí, *Increasing the efficiency of ideal solar cells by photon induced transitions at intermediate levels*, Phys. Rev. Lett. **78**, 5014 (1997).

[13] G. Wei and S. R. Forrest, *Intermediate-band solar cells employing quantum dots embedded in an energy fence barrier*, Nano Lett. **7**, 218 (2007).

[14] T. Trupke, M. A. Green, and P. Würfel, *Improving solar cell efficiencies by up-conversion of sub-band-gap light*, Journ. Appl. Physics **92**, 4117 (2002).

[15] T. Trupke, M. A. Green, and P. Würfel, *Improving solar cell efficiencies by down-conversion of sub-band-gap light*, Journ. Appl. Physics **92**, 1668 (2002).

[16] B. Parida, S. Iniyanb, and R. Goicc, *A review of solar photovoltaic technologies*, Renew. and Sust. Ener. Rev. **15**, 1625 (2011).

[17] A. Polman and H. Atwater, *Photonic design principles for ultrahigh-efficiency photovoltaics*, Nat. Mater. **11**, 174 (2012).

[18] F. I. for Solar Energy Systems ISE, *Photovoltaics Report*, Technical report, ISE, 2013.

[19] *Photovoltaics report*, Technical report, Fraunhofer ISE, 2014.

[20] H. A. Atwater and A. Polman, *Plasmonics for improved photovoltaic devices*, Nat. Mater. **9**, 205 (2010).

[21] E. Yablonovitch and G. D. Cody, *Intensity enhancement in textured optial sheets for solar cells*, IEEE Trans. Electr. Dev. **29**, 300 (1982).

[22] M. A. Green, *Lambertian light trapping in textured solar cells and light-emitting diodes: analytical solutions*, Prog. Photovoltaics **10**, 235 (2002).

[23] P. Spinelli, M. A. Verschuuren, and A. Polman, *Broadband omnidirectional antireflection coating based on subwavelength surface Mie resonators*, Nature. Comm. **3**, 692 (2012).

[24] U. Kreibig and M. Vollmer, *Optical Properties of Metal Clusters*, Springer **25**, 535 (1995).

[25] C. F. Bohren and D. R. Huffman, *Absorption and Scattering of Light by Small Particles*, Wiley, New York, 2008.

[26] A. A. Tseng, *Recent Developments in Nanofabrication Using Focused Ion Beams*, Small **1**, 924 (2005).

[27] C. Vieu, F. Carcenac1, A. Pépin, Y. Chen, M. Mejias, A. Lebib, L. Manin-Ferlazzo, L. Couraud, and H. Launois, *Electron beam lithography: resolution limits and applications*, Appl. Surf. Science **164**, 111 (2000).

[28] H. Fredriksson, Y. Alaverdyan, A. Dmitriev, C. Langhammer, D. Sutherland, M. Zäch, and B. Kasemo, *Hole-Mask Colloidal Lithography*, Adv. Mater. **19**, 4297 (2007).

[29] K. Aslan, Z. Leonenko, J. R. Lakowicz, and C. D. Geddes, *Annealed Silver-Island Films for Applications in Metal-Enhanced Fluorescence: Interpretation in Terms of Radiating Plasmons*, Journ. of Fluor. **15**, 643 (2005).

[30] Y. Sun and Y. Xia, *Shape-Controlled Synthesis of Gold and Silver Nanoparticles*, Science **298**, 2176 (2002).

[31] S. D. Zilio, K. Tvingstedt, O. Inganäsb, and M. Tormen, *Fabrication of a light trapping system for organic solar cells*, Microelec. Engin. **86**, 1150 (2009).

[32] Y. Xia and G. M. Whitesides, *Soft lithography*, Annu. Rev. Mater. Sci. **28**, 153 (1998).

[33] T. W. Odom, J. C. Love, D. B. Wolfe, K. E. Paul, and G. M. Whitesides, *Improved pattern transfer in soft lithography using composite stamps*, Langmuir **18**, 5314 (2002).

[34] S. Y. Chou, P. R. Krauss, and P. J. Renstrom, *Nanoimprint lithography*, J. Vac. Sci. Technol. B **14**, 4129 (1996).

[35] J. Haisma, M. Verheijen, K. van den Heuvel, and J. van den Berg, *Mold-assisted nanolithography: A process for reliable pattern replication*, J. Vac. Sci. Technol. B **14**, 4124 (1996).

[36] M. D. Austin, H. Ge, W. Wu, M. Li, Z. Yu, D. Wasserman, S. A. Lyon, and S. Y.

Chou, *Fabrication of 5 nm linewidth and 14 nm pitch features by nanoimprint lithography*, Appl. Phys. Lett. **84**, 5299 (2004).

[37] H. Schift, *Nanoimprint lithography: An old story in modern times? A review*, J. Vac. Sci. Technol. B **26**, 458 (2008).

[38] T. Balla, S. M. Spearing, and A. Monk, *An assessment of the process capabilities of nanoimprint lithography*, J. Phys. D: Appl. Phys. **41**, 174001 (2008).

[39] M. A. Verschuuren, *Substrate Conformal Imprint Lithography for Nanophotonic*, PhD thesis, Utrecht University, 2010.

[40] M. D. Kelzenberg, S. W. Boettcher, J. A. Petykiewicz, D. B. Turner-Evans, M. C. Putnam, E. L. Warren, J. M. Spurgeon, R. M. Briggs, N. S. Lewis, and H. A. Atwater, *Enhanced absorption and carrier collection in Si wire arrays for photovoltaic applications*, Nat. Mater. **9**, 239 (2010).

[41] M. Law, L. E. Greene, J. C. Johnson, R. Saykally, and P. D. Yang, *Nanowire dye-sensitized solar cells*, Nat. Mater. **4**, 455 (2005).

[42] J. Zhu., C.-M. Hsu, Z. Yu, S. Fan, and Y. Cui, *Nanodome solar cells with efficient light management and self-cleaning*, Nano Lett. **10**, 1979 (2010).

[43] M. Naughton et al., *Efficient nanocoax based solar cells*, Phys. Status Solidi RRL **4**, 181 (2010).

[44] R. Biswas, J. Bhattacharya, B. Lewis, N. Chakravarty, and V. Dalal, *Enhanced nanocrystalline silicon solar cell with a photonic crystal backreflector*, Sol. Energy Mat. Sol. Cells **94**, 2337 (2010).

[45] S. B. Mallick, M. Agrawal, and P. Peumans, *Optimal light trapping in ultra-thin photonic crystal cryscrystal silicon solar cells*, Opt. Express **18**, 5691 (2010).

[46] V. E. Ferry, M. A. Verschuuren, H. B. T. Li, E. Verhagen, R. J. Walters, R. E. I. Schropp, H. A. Atwater, and A. Polman, *Light trapping in ultrathin plasmonic solar cells*, Opt. Express **18**, A237 (2010).

[47] O. Isabella, A. Campa, M. C. R. Heijna, W. Soppe, R. V. Erven, R. H. Franken, H. Borg, and M. Zeman, *Diffraction Gratings for Light Trapping in Thin-Film Silicon Solar Cells*, in *Proceedings of the 23rd European Photovoltaic Solar EnergyConference*, pages 2320–2324, Valencia, Spain, 2008.

[48] C. Eisele, C. E. Nebel, and M. Stutzmann, *Periodic light coupler gratings in amorphous thin film solar cells*, J. Appl. Phys. **89**, 7722 (2001).

[49] C. Haase and H. Stiebig, *Thin-film silicon solar cells with efficient periodic light trapping texture*, Appl. Phys. Lett. **91**, 061116 (2007).

[50] D. Shir, J. Yoon, D. Chanda, J. H. Ryu, and J. A. Rogers, *Performance of ultrathin silicon solar microcells with nanostructures of relief formed by soft imprint lithography for broad band absorption enhancement*, Nano Lett. **10**, 3041 (2010).

[51] R. H. Franken, R. L. Stolk, H. Li, C. H. M. van der Werf, J. K. Rath, and R. E. I. Schropp, *Understanding light trapping by light scattering textured back electrodes in thin film n-i-p-type silicon solar cells*, J. Appl. Phys. **102**, 014503 (2007).

[52] C. Rockstuhl, S. Fahr, K. Bittkau, T. Beckers, R. Carius, F.-J. Haug, T. Söderström, C. Ballif, and F. Lederer, *Comparison and optimization of randomly textured surfaces in thin-film solar cells*, Opt. Express **18**, A335 (2010).

[53] G. Yue, L. Sivec, J. M. Owens, B. Yan, J. Yang, and S. Guha, *Optimization of back reflector for high efficiency hydrogenated nanocrystalline silicon solar cells*, Appl. Phys. Lett. **95**, 263501 (2009).

[54] J. Müller, B. Rech, J. Springer, and M. Vanecek, *TCO and light trapping in silicon*

thin film solar cells, Sol. Energy **77**, 917 (2004).

[55] H. Sai, H. Jia, and M. Kondo, *Impact of front and rear texture of thin-film microcrystalline silicon solar cells on their light trapping properties*, J. Appl. Phys. **108**, 045505 (2010).

[56] V. Ferry, L. Sweatlock, D. Pacifici, and H. Atwater, *Plasmonic nanostructure design for efficient light coupling into solar cells*, Nano Lett. **8**, 4391 (2008).

[57] V. E. Ferry, J. N. Munday, and H. A. Atwater, *Design considerations for plasmonic photovoltaics*, Adv. Mater. **22**, 4785 (2010).

[58] D. L. Staebler and C. R. Wronski, *Reversible conductivity changes in discharge-produced amorphous silicon*, Appl. Phys. Lett. **31**, 292 (1977).

[59] A. V. Shah, H. Schade, M. Vanecek, J. Meier, E. Vallat-Sauvain, N. Wyrsch, U. Kroll, C. Droz, and J. Bailat, *Thin-film Silicon Solar Cell Technology*, Prog. Photovoltaics **12**, 113 (2004).

[60] P. Campbell and M. A. Green, *The limiting efficiency of silicon solar-cells under concentrated sunlight*, IEEE Trans. Electron Devices **33**, 234 (1986).

[61] M. Verschuuren and H. van Sprang, *3D photonic structures by solgel imprint lithography*, Mater. Res. Soc. Symp. Proc. **1002**, N03 (2007).

[62] C. Stuart and Y. Chen, *Roll in and roll out: a path to high-throughput nanoimprint lithography*, ACS Nano **3**, 2062 (2009).

[63] K. Söderström, J. Escarré, O. Cubero, F.-J. Haug, and C. Ballif, *UV-nano-imprint lithography technique for the replication of back reflectors for n-i-p thin film silicon solar cells*, Prog. Photovoltaics **19**, 202 (2011).

[64] C. Battaglia, K. Söderström, J. Escarré, F.-J. Haug, D. Domine, P. Cuony, M. Boccard, G. Bugnon, C. Denizot, M. Despeisse, A. Feltrin, and C. Ballif, *Efficient light management scheme for thin film silicon solar cells via transparent random nanostructures fabricated by nanoimprinting*, Appl. Phys. Lett. **96**, 213504 (2010).

[65] Y.-F. Huang, S. Chattopadhyay, Y.-J. Jen, C.-Y. Peng, T.-A. Liu, Y.-K. Hsu, C.-L. Pan, H.-C. Lo, C.-H. Hsu, Y.-H. Chang, C.-S. Lee, K.-H. Chen, and L.-C. Chen, *Improved broadband and quasi-omnidirectional anti-reflection properties with biomimetic silicon nanostructures*, Nat. Nanotechnol. **2**, 770 (2007).

[66] F.-J. Haug, T. Söderström, O. Cubero, V. Terrazoni-Daudrix, and C. Ballif, *Influence of the ZnO layer structure on the guided mode structure in Si/ZnO/Ag multilayers*, J. Appl. Phys. **106**, 044502 (2009).

[67] F. Biscarini, P. Samorí, O. Greco, and R. Zamboni, *Scaling behavior of anisotropic organic thin films grown in high vacuum*, Phys. Rev. Lett. **78**, 2389 (1997).

[68] L. Cao, J. S. White, J.-S. Park, J. A. Schuller, B. M. Clemense, and M. L. Brongersma, *Engineering light absorption in semiconductor nanowire devices*, Nat. Mater. **8**, 643 (2009).

[69] K. R. Catchpole and A. Polman, *Design principles for particle plasmon enhanced solar cells*, Appl. Phys. Lett. **93**, 191113 (2008).

[70] F. J. Beck, A. Polman, and K. R. Catchpole, *Tunable light trapping for solar cells using localised surface plasmons*, J. Appl. Phys. **105**, 114310 (2009).

[71] Y. Akimov and W. Koh, *Role of surface metal nanoparticles on the absorption in solar cells*, Plasmonics **6**, 155 (2011).

[72] C. McPheeters, C. J. Hill, S. H. Lim, D. Derkacs, D. Z. Ting, and E. T. Yu, *Improved performance of In(Ga)As/GaAs quantum dot solar cells via light scattering by nanoparticles*, J. Appl. Phys. **106**, 056101 (2009).

[73] R. A. Pala, J. White, E. Barnard, J. Liu, and M. L. Brongersma, *Design of Plasmonic*

Thin-Film Solar Cells with Broadband Absorption Enhancements, Adv. Mater. **21**, 3504 (2009).

[74] C. Rockstuhl, S. Fahr, and F. Lederer, *Absorption enhancement in solar cells by localized plasmon polaritons*, J. Appl. Phys. **104**, 123102 (2008).

[75] P. Spinelli, M. Hebbink, R. de Waele, L. Black, F. Lenzmann, and A. Polman, *Optical Impedance Matching Using Coupled Plasmonic Nanoparticle Arrays*, Nano Lett. **11**, 1760 (2011).

[76] P. Spinelli, C. van Lare, E. Verhagen, and A. Polman, *Controlling Fano lineshapes in plasmon-mediated light coupling into a substrate*, Optics Express **19**, A303 (2011).

[77] W. J. Soppe, H. Borg, B. B. van Aken, C. Devilee, M. Dörenkämper, M. Goris, M. C. R. Heijna, J. Löffler, and P. Peeters, *Roll to roll fabrication of thin film silicon solar cells on nano-textured substrates*, J. Nanosci. Nanotechnol. **11**, 10604 (2011).

[78] I. Diukman and M. Orenstein, *How front side plasmonic nanostructures enhance solar cell efficiency*, Sol. Energy Mat. Sol. Cells **95**, 2628 (2011).

[79] S. Pillai, K. R. Catchpole, T. Trupke, and M. A. Green, *Surface plasmon enhanced silicon solar cells*, J. Appl. Phys. **101**, 093105 (2007).

[80] A. Ji, Sangita, and R. P. Sharma, *A study of nanoellipsoids for thin-film plasmonic solar cell applications*, J. Phys. D: Appl. Phys. **45**, 275101 (2012).

[81] A. Pors, A. V. Uskov, M. Willatzen, and I. E. Protsenko, *Control of the input efficiency of photons into solar cells with plasmonic nanoparticles*, Opt. Comm. **284**, 2226 (2011).

[82] S. H. Lim, W. Mar, P. Matheu, D. Derkacs, and E. T. Yu, *Photocurrent spectroscopy of optical absorption enhancement in silicon photodiodes via scattering from surface plasmon polaritons in gold nanoparticles*, J. Appl. Phys. **101**, 104309 (2007).

[83] P. R. West, S. Ishii, G. V. Naik, N. K. Emani, V. M. Shalaev, and A. Boltasseva, *Searching for better plasmonic materials*, Laser and Phot. Rev. **4**, 795 (2010).

[84] V. E. Ferry, M. A. Verschuuren, M. V. Lare, R. E. I. Schropp, H. A. Atwater, and A. Polman, *Optimized Spatial Correlations for Broadband Light Trapping Nanopatterns in High Efficiency Ultrathin Film a-Si:H Solar Cells*, Nano Lett. **11**, 4239 (2011).

[85] C. Battaglia, J. Escarré, K. Söderström, M. Charrière, M. Despeisse, F. J. Haug, and C. Baliff, *Nanomoulding of transparent zinc oxide electrodes for efficient light trapping in solar cells*, Nat. Phot. **5**, 535 (2011).

[86] P. Spinelli, V. E. Ferry, C. V. Lare, J. V. de Groep, M. A. Verschuuren, R. E. I. Schropp, H. A. Atwater, and A. Polman, *Plasmonic light trapping in thin-film solar cells*, Journ. Opt. **14**, 24002 (2012).

[87] A. Williamson, E. McClean, D. Leipold, D. Zerulla, and E. Runge, *The design of efficient surface-plasmon-enhanced ultra-thin polymer-based solar cells*, Appl. Phys. Lett. **99**, p093307 (2011).

[88] F. J. Beck, E. Verhagen, S. Mokkapati, A. Polman, and K. Catchpole, *Resonant SPP modes supported by discrete metal nanoparticles on high-index substrates*, Opt. Express **19**, A146 (2011).

[89] M. van Lare, F. Lenzmann, M. A. Verschuuren, and A. Polman, *Mode-coupling by plasmonic surface scatterers in thin-film Si solar cells*, Appl. Phys. Lett. **101**, 221110 (2012).

[90] K. R. Catchpole and A. Polman, *Plasmonic solar cells*, Opt. Express **16**, 21793 (2008).

[91] V. Jovanov, U. Planchoke, P. Magnus, H. Stiebig, and D. Knipp, *Inflcells of back contact morphology on light trapping and plasmonic effects in microcrystalline silicon junction and micromorph tandem solar cells*, Solar Energie Materials and Solar Cells **110**, 49 (2013).

[92] U. W. Paetzold, E. Moulin, D. Michaelis, W. Böttler, C. Wächter, V. Hagemann, M. Meier, R. Carius, and U. Rau, *Plasmonic reflection grating back contacts for microcrystalline silicon solar cells*, Appl. Phys. Lett. **99**, p181105 (2011).

[93] A. Shah, P. Torres, R. Tscharner, N. Wyrsch, and H. Keppner, *Photovoltaic Technology: The Case for Thin-Film Solar Cells*, Science **285**, 692 (1999).

[94] H. Keppner, J. Meier, P. Torres, D. Fischer, and A. Shah, *Microcrystalline silicon and micromorph solar cells*, Appl. Phys. **69**, 169 (1999).

[95] Y. Tsunomura, Y. Yoshimine, M. Taguchi, T. Baba, T. Kinoshita, H. Kanno, H. Sakata, E. Maruyama, and M. Tanaka, *Twenty-two percent efficiency HIT solar cell*, Sol. Energy Mat. Sol. Cells **93**, 670 (2009).

[96] M. Taguchi, A. Yano, S. Tohoda, K. Matsuyama, Y. Nakamura, T. Nishiwaki, K. Fujita, and E. Maruyama, *24.7% Record Efficiency HIT Solar Cell on Thin Silicon Wafer*, IEEE J. Photovoltaics **4**, 96 (2014).

[97] *Films that Scatter Sunlight with a Nanoscale Concavoconvex Surface for Improved Power Generation Efficiency*, `http://www.agc.com/english/csr/env/products/3.html`.

[98] O. Kluth, B. Rech, L. Houben, S. Wieder, G. Schöpe, C. Beneking, H. Wagner, A. Löffl, and H. W. Schock, *Texture etched ZnO:Al coated glass substrates for silicon based thin film solar cells*, Thin Solid Films **351**, 247 (1999).

[99] M. Berginski, J. Hüpkes, M. Schulte, G. Schöpe, H. Stiebig, B. Rech, and M. Wuttig, *The effect of front ZnO:Al surface texture and optical transparency on efficient light trapping in silicon thin-film solar cells*, J. Appl. Phys. **101**, 074903 (2007).

[100] S. Faß, J. Steinhauser, N. Oliveira, E. Vallat-Sauvain, and C. Ballif, *Opto-electronic properties of rough LP-CVD ZnO:B for use as TCO in thin-film silicon solar cells*, Thin Solid Films **515**, 8558 (2007).

[101] B. Tian, X. Zheng, T. J. Kempa, Y. Fang, N. Yu, G. Yu, J. Huang, and C. M. Lieber, *Coaxial silicon nanowires as solar cells and nanoelectronic power sources*, Nature **449**, 885 (2007).

[102] E. C. Garnett and P. Yang, *Silicon Nanowire Radial p-n Junction Solar Cells*, J. Am. Chem. Soc. **130**, 9224 (2008).

[103] B. M. Kayes, H. A. Atwater, and N. S. Lewis, *Comparison of the device physics principles of planar and radial p-n junction nanorod solar cells*, J. Appl. Phys. **97**, 114302 (2005).

[104] M. Krunks, A. Katerski, T. Dedova, I. O. Acik, and A. Mere, *Nanostructured solar cell based on spray pyrolysis deposited ZnO nanorod array*, Sol. Energy Mat. Sol. Cells **92**, 1016 (2008).

[105] Y. Kuang, K. H. M. van der Werf, Z. S. Houweling, and R. E. I. Schropp, *Nanorod solar cell with an ultrathin a-Si: H absorber layer*, Appl. Phys. Lett. **98**, 113111 (2011).

[106] Z. Fan, H. Razavi, J. W. Do, A. Moriwaki, O. Ergen, Y. Chueh, P. Leu, J. C. Ho, T. Takahashi, L. A. Reichertz, S. Neale, K. Yu, M. Wu, J. W. Ager, and A. Javey, *Three-dimensional nanopillar-array photovoltaics on low-cost and flexible substrates*, Nat. Mater. **8**, 648 (2009).

[107] M. Vanecek, O. Babchenko, A. Purkrt, J. Holovsky, N. Neykova, A. Poruba,

Z. Remes, J. Meier, and U. Kroll, *Nanostructured three-dimensional thin film silicon solar cells with very high efficiency potential*, Appl. Phys. Lett. **98**, 163503 (2011).

[108] J. Kim, A. J. Hong, J. W. Nah, B. Shin, F. M. Ross, and D. K. Sadana, *Three-Dimensional a-Si:H Solar Cells on Glass Nanocone Arrays Patterned by Self-Assembled Sn Nanospheres*, ACS Nano **6**, 265 (2012).

[109] A. Mavrokefalos, S. E. Han, S. Yerci, M. S. Branham, and G. Chen, *Efficient Light Trapping in Inverted Nanopyramid Thin Crystalline Silicon Membranes for Solar Cell Applications*, Nano Lett. **12**, 2792 (2012).

[110] Y. Kuang, M. D. Vece, J. K. Rath, L. van Dijk, and R. E. I. Schropp, *Elongated nanostructures for radial junction solar cells*, Rep. Prog. Phys. **76**, 106502 (2013).

[111] Y. Kuang, K. van der Werf, Z. Houweling, M. D. Vece, and R. Schropp, *Fabrication and characterization of nanorod solar cells with an ultrathin aSi:H absorber layer*, J. Non-Cryst. Solids **358**, 2209 (2012).

[112] M. Boccard, C. Battaglia, S. Hänni, K. Söderström, J. Escarré, S. Nicolay, F. Meillaud, M. Despeisse, and C. Ballif, *Multiscale transparent electrode architecture for efficient light management and carrier collection in solar cells*, Nano Lett. **12**, 1344 (2012).

[113] M. van Lare, F. Lenzmann, and A. Polman, *Dielectric back scattering patterns for light trapping in thin-film Si solar cells*, Opt. Express **21**, 20738 (2013).

[114] J. M. Spurgeon, H. A. Atwater, and N. S. Lewis, *A Comparison Between the Behavior of Nanorod Array and Planar Cd(Se, Te) Photoelectrodes*, J. Phys. Chem. C **112**, 6186 (2008).

[115] C. M. Hsu, C. Battaglia, C. Pahud, Z. Ruan, F. J. Haug, S. Fan, C. Ballif, and Y. Cui, *High-Efficiency Amorphous Silicon Solar Cell on a Periodic Nanocone Back Reflector*, Adv. Energy Mater. **2**, 628 (2012).

[116] D. Kieven, T. Dittrich, A. Belaidi, J. Tornow, K. Schwarzburg, N. Allsop, and M. Lux-Steiner, *Effect of internal surface area on the performance of $ZnO/In_2S_3/CuSCN$ solar cells with extremely thin absorber*, Appl. Phys. Lett. **92**, 153107 (2008).

[117] V. Ferry, M. Verschuuren, H. Li, R. Schropp, H. Atwater, and A. Polman, *Improved red-response in thin film a-Si:H solar cells with soft-imprinted plasmonic back reflectors*, Appl. Phys. Lett. **95**, 183503 (2009).

[118] G. Mariani, Z. Zhou, A. Scofield, and D. L. Huffaker, *Direct-Bandgap Epitaxial CoreŰMultishell Nanopillar Photovoltaics Featuring Subwavelength Optical Concentrators*, Nano Lett. **13**, 1632 (2013).

[119] M. Mazilu, N. Tigau, and V. Musat, *Optical properties of undoped and Al-doped ZnO nanostructures grown from aqueous solution on glass substrate*, Opt. Mat. **34**, 1833 (2012).

[120] A. Basch, F. J. Beck, T. Söderström, S. Varlamov, and K. R. Catchpole, *Combined plasmonic and dielectric rear reflectors for enhanced photocurrent in solar cells*, Appl. Phys. Lett. **100**, 243903 (2012).

[121] R. A. Pala, J. S. Q. Liu, E. S. Barnard, D. Askarov, E. C. Garnett, S. Fan, and M. L. Brongersma, *Optimization of non-periodic plasmonic light-trapping layers for thin-film solar cells*, Nat. Commun. **4** (2013).

[122] M. Soldera, E. Estrada, and K. Taretto, *Geometric Light Trapping in 2D and 3D Structured Small Molecule Organic Solar Cells*, in *Symposium E/H Ű Photovoltaic Technologies, Devices and Systems Based on Inorganic Materials, Small Organic*

Molecules and Hybrids, 2013.

[123] K. J. Yu, L. Gao, J. S. Park, Y. R. Lee, C. J. Corcoran, R. G. Nuzzo, D. Chanda, and J. A. Rogers, *Light Trapping: Light Trapping in Ultrathin Monocrystalline Silicon Solar Cells*, Adv. Energy Mater. **3**, 1528 (2013).

[124] H. Tan, R. Santbergen, A. H. M. Smets, and M. Zeman, *Plasmonic Light Trapping in Thin-film Silicon Solar Cells with Improved Self-Assembled Silver Nanoparticles*, Nano Lett. **8**, 4070 (2012).

[125] P. Spinelli and A. Polman, *Light Trapping in Thin Crystalline Si Solar Cells Using Surface Mie Scatterers*, IEEE Journal of Photovoltaics **4**, 554 (2014).

[126] S. A. Mann, R. R. Grote, R. M. Osgood, and J. A. Schuller, *Dielectric particle and void resonators for thin film solar cell textures*, Opt. Express **19**, 25729 (2011).

[127] J. Bhattacharya, N. Chakravarty, S. Pattnaik, W. D. Slafer, R. Biswas, and V. L. Dalal, *A Photonic-Plasmonic Structure for Enhancing Light Absorption in Thin Film Solar Cells*, Appl. Phys. Lett. **99**, 131114 (2011).

[128] F.-J. Haug, T. Söderström, O. Cubero, V. Terrazzoni-Daudrix, and C. Ballif, *Plasmonic absorption in textured silver back reflectors of thin film solar cells*, Appl. Phys. **104**, 064509 (2008).

[129] P. Jackson, D. Hariskos, R. Wuerz, W. Wischmann, and M. Powalla, *Compositional investigation of potassium doped Cu(In,Ga)Se_2 solar cells with efficiencies up to 20.8%*, Rapid Research Letters **8**, 219 (2014).

[130] S. Wei and A. Zunger, *Band Offsets and Optical Bowings of Chalcopyrites and Zn-Based II-VI Alloys*, J. Appl. Phys. **78**, 3846 (1995).

[131] M. Gloeckler and J. R. Sites, *Potential of submicrometer thickness Cu(In,Ga)Se_2 solar cells*, J. Appl. Phys. **98**, 103703 (2005).

[132] M. Contreras, J. Tuttle, D. H. Du, Y. Qi, A. Swartzlander, A. Tennant, and R. Noufi, *Graded band-gap Cu(in,Ga)Se_2 thin-film solar-cell absorber with enhanced open-circuit voltage*, Appl. Phys. Lett. **63**, 1824 (1993).

[133] S. Schleussner, U. Zimmermann, T. Wätjen, K. Leifer, and M. Edoff, *Effect of gallium grading in Cu(In,Ga)Se_2 solar-cell absorbers produced by multi-stage coevaporation*, Sol. Energy Mat. Sol. Cells **95**, 721 (2011).

[134] A. M. Gabor, J. R. Tuttle, M. H. Bode, A. Franz, A. L. Tennant, M. A. Contreras, R. Noufi, D. G. Jensen, and A. M. Hermann, *Band-gap engineering in Cu(In,Ga)Se_2 thin films grown from (In,Ga)$_2Se_3$ precursors*, Sol. Energy Mat. Sol. Cells **41-2**, 247 (1996).

[135] T. Dullweber, G. Hanna, W. Shams-Kolahi, A. Schwartzlander, M. A. Contreras, R. Noufi, and H. W. Schock, *Study of the effect of gallium grading in Cu(In,Ga)Se_2*, Thin Solid Films **361**, 478 (2000).

[136] M. Troviano and K. Taretto, *Temperature-dependent quantum efficiency analysis of graded-gap*, Sol. Energy Mat. Sol. Cells **95**, 3081 (2011).

[137] L. Andreani, P. Kowalczewski, C. Mura, M. Patrini, M. Acciarri, S. Binetti, A. Sassella, and S. Marchionna, *Towards CIGS Solar Cells with Reduced Film Thickness: A Study of Optical Properties and of Photonic Structures for Light Trapping*, in *27th European Photovoltaic Solar Energy Conference and Exhibition*, 2012.

[138] M. Schmid, R. Klenk, M. C. Lux-Steiner, M. Topič, and J. Krč, *Modeling plasmonic scattering combined with thin-film optics*, Nanotechnology **2**, 024204 (2011).

[139] M. Schmid, J. Klaer, R. Klenk, M. Topič, and J. Krč, *Stability of plasmonic metal nanoparticles integrated in the back contact of ultra-thin Cu(In,Ga)S_2 solar cells*,

Thin Solid Films **527**, 308 (2013).

[140] K. Orgassa, H. W. Schock, and J. H. Werner, *Alternative back contact materials for thin film Cu(In,Ga)Se_2 solar cells*, Thin Solid Films **431–432**, 387 (2003).

[141] D. J. L. Brémaud, *Investigation and Development of CIGS Solar Cells on Flexible Substrates and with Alternative Electrical Back Contacts*, PhD thesis, ETH Zurich, 2009.

[142] A. M. Gabor, J. R. Tuttle, D. S. Albin, M. A. Contreras, R. Noufi, and A. M. Hermann, *High-efficiency $CuIn_xGa_{1-x}Se_2$ solar-cells made from $(In_xGa_{1-x})_2Se_3$ precursor films*, Appl. Phys. Lett. **65**, 198 (1994).

[143] G. Yin, V. Brackmann, V. Hoffmann, and M. Schmid, *Enhanced performance of ultra-thin Cu(In,Ga)Se_2 solar cells deposited at low process temperature*, submitted to Solar Energy Materials and Solar Cells.

[144] G. Yin, C. Merschjann, and M. Schmid, *The effect of surface roughness on the determination of optical constants of $CuInSe_2$ and $CuGaSe_2$ thin films*, J. Appl. Phys. **113**, 213510 (2013).

[145] G. Yin, P. Manley, and M. Schmid, *Influence of substrate and its temperature on the optical constants of $CuIn_1 - xGa_xSe_2$ thin films*, Journ. of Phys. D: Appl. Phys. **47**, 135101 (2014).

[146] C. Battaglia, C. M. Hsu, K. Söderström, J. Escarré, F. J. Haug, M. Charrière, M. Boccard, M. Despeisse, D. T. L. Alexander, M. Cantoni, Y. Cui, and C. Ballif, *Light Trapping in Solar Cells: Can Periodic Beat Random?*, ACS Nano **6(3)**, 2790 (2012).

[147] P. Kowalczewski, M. Liscidini, and L. Andreani, *Light trapping in thin-film solar cells with randomly rough and hybrid textures*, Opt. Express **21**, A808 (2013).

[148] S. Pattnaik, N. Chakravarty, R. Biswas, V. Dalal, and D. Slafer, *Nano-photonic and nano-plasmonic enhancements in thin film silicon solar cells*, Sol. Energy Mat. Sol. Cells **129**, 115 (2014).

[149] T. Söderström, F.-J. Haug, X. Niquille, and C. Ballif, *TCOs for nip thin film silicon solar cells*, Progr. Photovolt: Res. and App. **17**, 165 (2009).

[150] H. Sai, H. Fujiwara, M. Kondo, and Y. Kanamori, *Enhancement of light trapping in thin-film hydrogenated microcrystalline Si solar cells using back reflectors with self-ordered dimple pattern*, Appl. Phys. Lett. **93**, 143501 (2008).

[151] E. Kreyszig, *Advanced Engineering Mathematics*, Peter Janzow, 1999.

[152] E. R. Martins, J. Li, Y. Liu, V. Depauw, Z. Chen, J. Zhou, and T. F. Krauss, *Deterministic quasi-random nanostructures for photon control*, Nat. Commun. **4** (2013).

[153] E. R. Martins, J. Li, Y. Liu, J. Zhou, and T. F. Krauss, *Engineering gratings for light trapping in photovoltaics: The supercell concept*, Phys. Rev. B **86**, 041404 (2012).

[154] E. Verhagen, *Subwavelength light confinement with surface plasmon polaritons*, PhD thesis, Utrecht University, 2009.

[155] J. van de Groep, *Light trapping in thin silicon waveguides by plasmon mediated mode coupling*, Master's thesis, Utrecht University, 2011.

[156] T. Itoh and N. Yamauchi, *Surface morphology characterization of pentacene thin film and its substrate with under-layers by power spectral density using fast Fourier transform algorithms*, Appl. Surf. Science **253**, 6196 (2007).

[157] *Mersenne Twister*, `http://www.math.sci.hiroshima-u.ac.jp/~m-mat/MT/emt.html`.

[158] W. T. Silfvast, *Laser Fundamentals*, University of Cambridge, 2004.

[159] H. Mashaal and J. M. Gordon, *Fundamental bounds for antenna harvesting of sunlight*, Optics Letters **36**, 900 (2011).

[160] S. K. Nair, K. Rajeev, and K. Parameswaran, *Cloud screening in IRS-P4 OCM satellite data: potential of spatial coherence method in the absence of thermal channel information*, Remote Sens. Environ. **90**, 259 (2003).

Summary

Photovoltaics (PV) is a sustainable and clean source of energy and the sun provides more than enough energy to make PV a major electricity source. To make PV fully competitive with conventional energy sources, a reduction of the cost per watt is required. This can be achieved by increasing the conversion efficiency of the modules or by decreasing manufacturing cost. Thin-film solar cells, which have substantially thinner absorber layers than conventional wafer-based solar cells, offer the potential for lower manufacturing costs. They can also serve as top cells in high-efficiency tandem solar cells. A major problem with thin-film solar cells is the incomplete absorption of the solar spectrum, which leads to a drastic reduction of the efficiency. To enhance the absorption of light in thin-film solar cells light trapping is required, in which nanostructures are integrated in the cell to enhance the path length of the light in the absorber layer. In this thesis we present new insights in light trapping in thin-film hydrogenated amorphous Si (a-Si:H) and Cu(In,Ga)Se_2 (CIGSe) solar cells. We experimentally study arrays of metallic and dielectric resonant scatterers at the front and at the back side of thin-film solar cells, and demonstrate efficient light trapping without deterioration of the electrical properties of the devices. We emphasize the relevance of minimizing optical losses in the light trapping patterns. We compare periodic and random scattering patterns and demonstrate the importance of the spatial frequency distribution in the scattering patterns. We present an optimization of the spatial frequency distribution of light trapping patterns that is applicable to all thin-film solar cell types. In Chapter 2 we present wafer-scale fabrication of nanoscale light trapping patterns using substrate conformal imprint lithography (SCIL). Using SCIL in combination with evaporation and lift off, we fabricate arrays of dielectric and metallic light trapping patterns both at the front and back side of thin-film solar cells. We fabricate patterned metal back contacts for thin-film solar cells by sputter coating printed sol-gel layers with metals.

In Chapter 3 we study light trapping in ultra-thin a-Si:H solar cells, with absorber layer thicknesses of 90–150 nm, grown on top of periodically and randomly patterned metal back contacts. The cells show a broadband photocurrent

enhancement because of light trapping by the patterned back contact and an antireflection effect by the corrugated surface, which originates from conformal growth of the thin-film stack on a patterned back contact. We show that these light trapping patterns outperform the Asahi-U type pattern, which is the commercial light trapping standard for thin-film a-Si:H solar cells. We relate the photocurrent spectra to the spatial correlations in the light trapping patterns.

In Chapter 4 we demonstrate effective waveguide-mode coupling using plasmonic surface scatterers printed onto completed thin-film a-Si:H solar cells, with an absorber layer thickness of 350 nm, using substrate conformal imprint lithography (SCIL). Using numerical simulations, we show that an optimized array geometry can result in an enhanced red- and blue response of the device. The blue response of the device can be further enhanced using Al instead of Ag nanoparticles. We demonstrate that a broadband absorption enhancement can be obtained with dielectric scattering patterns consisting of arrays of TiO_2 particles, which efficiently scatter the light and have low optical losses.

In Chapter 5 we experimentally study the influence of patterning the Al-doped ZnO (AZO) buffer layer that is in between the metal back contact and the absorber layer in the same cell type as in Chapter 4. By comparing light trapping with randomly patterned metal back contacts covered with patterned or flat AZO layers, we show that patterning the AZO layer is indispensable for efficient light trapping in this cell geometry. Using numerical simulations, we demonstrate that light trapping can be further enhanced using purely dielectric scattering patterns, in which the AZO layer is patterned and the metal is completely flat. These dielectric scattering patterns efficiently scatter the light and do not suffer from Ohmic losses as is the case for plasmon resonances in Ag.

In Chapter 6 we present thin-film a-Si:H solar cells, with absorber layer thicknesses of 100 and 200 nm, deposited on top of random arrays of nanorods. These nanorods are grown by chemical bath deposition, which is an inexpensive, scalable and tunable growth process. Full device stacks, consisting of Ag, AZO, a-Si:H and ITO are deposited on top of the nanorods which results in radial junction solar cells. These cells show efficient light trapping and an enhanced blue response. Numerical simulations are in good agreement with experimental EQE data and show that absorption in the Ag layer of these rod cells is strongly enhanced with respect to flat cells. Further enhanced light trapping can be obtained by flattening the metal and only patterning the dielectric layers.

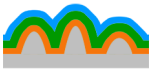

Dielectric back scattering patterns for light trapping are further studied in Chapter 7. This chapter focuses on periodic scattering patterns. We experimentally demonstrate broadband efficient light trapping in 350 nm a-Si:H cells periodically patterned AZO layers and show that these cells outperform reference cells on Asahi-U type texture. Due to conformal growth, also the bottom part of the a-Si:H layer is patterned. Since the AZO particle diameter is close to the array pitch, the AZO particles enclose a-Si:H scatterers. Using numerical simulations, we show that dielectric resonances occur both in the AZO particles in the a-Si:H scatterers and that the size of the a-Si:H scatterers

is crucial for light trapping.

In Chapter 8 we use dielectric scattering patterns to achieve light trapping in ultra-thin CIGSe cells, with absorber layer thicknesses of 460 nm. We experimentally demonstrate a photocurrent enhancement in CIGSe cells with arrays of dielectric scatterers printed on the front side. Using numerical simulations, we show that the absorption enhancement is due to an antireflection effect rather than to light trapping. We experimentally demonstrate light trapping in CIGSe cells with arrays of SiO_2 particles at the CIGSe/Mo interface, which results in an efficiency gain from 11.0% to 12.4%. Using numerical simulations we show that these dielectric scattering patterns reduce the optical losses in the strongly absorbing Mo back contact. To further reduce absorption in the back contact, we replace the Mo layer by ITO and find that, even though there is transmission through the back contact, integrated absorption in a patterned cell on ITO can be as high as in a patterned cell on a Mo back reflector. This geometry could be interesting for tandem devices.

In Chapters 3-8 we showed that efficient scattering can be obtained with scattering patterns, both on the front and back side of the solar cell. In Chapter 9, we present insight in the spatial frequency distributions of the scattering patterns. We demonstrate the relation between peaks in absorption spectra and the power spectral density of spatial frequencies (PSD), which is the spatial Fourier transform of the scattering pattern. Using a Monte Carlo algorithm, we optimize arrays of dielectric scatterers to have elevated PSD in the spatial frequency range that overlaps with the waveguide modes of a specific device geometry. We also demonstrate an approach that gives more freedom in designing the PSD spectrum, which relies on the optimization of random textures.

Overall, this thesis provides fundamental insights in light trapping in thin-film solar cells and focuses on designs with large scattering efficiency, low optical losses, and a PSD spectrum that can be tailored to a specific device stack. It presents light trapping patterns that lead to significant absorption enhancement in thin-film solar cells without deterioration of the electrical properties. The concepts discussed in this thesis are applicable to all types of thin-film solar cells.

Samenvatting

Photovoltaica is een duurzame en schone bron van energie en de zon levert meer dan genoeg energie om photovoltaica een substantiële bron van energie te laten worden voor onze samenleving. Om photovoltaica volledig concurrerend te maken met conventionele energiebronnen is een reductie van de kosten per watt nodig. Dit kan bereikt worden door het verhogen van het conversierendement of het verlagen van de productiekosten. Dunne-film zonnecellen, welke substantieel dunnere lichtabsorberende lagen hebben dan conventionele wafergebaseerde zonnecellen, bieden potentieel lagere productiekosten. Verder kunnen ze als topcel gebruikt worden in hoog-rendement tandemzonnecellen. Een groot probleem van dunne-film zonnecellen is dat zij het zonnespectrum niet volledig absorberen, wat leidt tot een drastische reductie in het rendement. Om de absorptie van licht in deze zonnecellen te verhogen, is het nodig het licht op te sluiten in de dunne-film zonnecel; hiervoor worden nanostructuren geïntegreerd in de cel om de padlengte van het licht in de absorberende laag te vergroten.

In dit proefschrift presenteren wij nieuwe inzichten in lichtopsluiting in dunne-film gehydrogeneerde amorf Si (a-Si:H) en $Cu(In,Ga)Se_2$ (CIGSe) zonnecellen. Door middel van experimenten bestuderen we roosters van metallische en diëlektrische nanodeeltjes aan de voor- en achterkant van dunne-film zonnecellen en demonstreren we efficiënte lichtopsluiting zonder verslechtering van de elektrische eigenschappen van de cellen. We benadrukken het belang van het minimaliseren van absorptieverliezen in de lichtopsluitingspatronen. We vergelijken periodieke en ongeordende roosters van nanodeeltjes en demonstreren de relevantie van de verdeling van de spatiële frequenties in de verstrooiingspatronen. We presenteren een optimalisatie van deze spatiële-frequentieverdeling van lichtverstrooiingspatronen die toepasbaar is op alle typen dunne-film zonnecellen.

Hoofdstuk 2 presenteert de fabricage van nanoschaallichtverstrooiingspatronen op waferschaal door middel van substraat-conforme imprint lithografie (SCIL). Gebruikmakend van SCIL in combinatie met opdampen fabriceren we roosters van diëlektrische en metallische nanodeeltjes zowel aan de voor- als aan de achterkant van dunne-film zonnecellen. We fabriceren nanogestructureerde

achtercontacten voor dunne-film zonnecellen door SCIL-geprinte sol-gel lagen te sputtercoaten met metalen.

In Hoofdstuk 3 bestuderen we lichtopsluiting in ultradunne a-Si:H zonnecellen, met absorberende lagen met een dikte van 90–150 nm, gegroeid op periodieke en ongeordende gestructureerde achtercontacten. De cellen laten een breedbandige toename in de fotostroom zien als gevolg van lichtopsluiting door het gestructureerde achtercontact en een antireflectie-effect door het gestructureerde celoppervlak, dat deze structuur verkregen heeft door conforme groei van de dunne lagen op het gestructureerde achtercontact. We laten zien dat deze patronen tot een hogere fotostroom leiden dan het conventionele Asahi-U type patroon. We relateren fotostroomspectra aan spatiële correlaties in de verstrooiingspatronen.

In Hoofdstuk 4 demonstreren we effectieve koppeling aan golfgeleidermodes in dunne-film a-Si:H zonnecellen, met absorberende lagen met een dikte van 350 nm, door gebruik van plasmonische oppervlaktesverstrooiers geprint door middel van SCIL. Met behulp van numerieke simulaties laten we zien dat een geoptimaliseerde roostergeometrie kan resulteren in een verhoogde rood- en blauwrespons van de cel. De blauwrespons kan verder worden verhoogd door Al nanodeeltjes te gebruiken in plaats van Ag nanodeeltjes. We laten zien dat een breedbandige absorptietoename kan worden verkregen met gebruik van diëlektrische verstrooiingspatronen bestaand uit TiO_2 nanodeeltjes, welke het licht efficiënt verstrooien en lage absorptieverliezen hebben.

In Hoofdstuk 5 bestuderen we door middel van experimenten de invloed van het textureren van de Al-gedoteerde ZnO (AZO) bufferlaag die tussen het metalen achtercontact en de absorberende laag zit in hetzelfde type cel als in Hoofdstuk 4. Door het vergelijken van lichtopsluiting in cellen met een gestructureerd metalen achtercontact bedekt met een getextureerde of met een vlakke AZO laag, laten we zien dat het textureren van de AZO laag essentieel is voor lichtopsluiting in deze celgeometrie. Met behulp van numerieke simulaties laten we zien dat de mate van lichtopsluiting verder kan worden verhoogd door het gebruik van puur diëlektrische verstrooiingspatronen, waarbij de AZO laag getextureerd is en het metaal volledig vlak is. Deze diëlektrische verstrooiingspatronen verstrooien het licht op efficiënte wijze en lijden niet onder Ohmische verliezen zoals wel het geval is voor plasmonische resonanties in Ag.

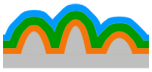

In Hoofdstuk 6 presenteren we dunne-film zonnecellen, met absorberende lagen met diktes van 100 nm en 200 nm, gedeponeerd op ongeordende roosters van ZnO nanostaafjes. Deze nanostaafjes zijn gegroeid door middel van chemische baddepositie, wat een goedkoop, schaalbaar en afstembaar groeiproces is. De volledige stapeling van zonnecellagen, bestaande uit Ag, AZO, a-Si:H en ITO, is gedeponeerd bovenop de nanostaafjesroosters wat resulteert in zonnecellen met een radiale diodeovergang. Deze cellen laten efficiënte lichtopsluting zien en een toename van de blauwrespons. Numerieke simulaties zijn in overeenstemming met experimentele externe kwantum efficiëntie (EQE) data en laten zien dat absorptie in de Ag-laag bij deze staafjescellen sterk is toegenomen ten opzichte

van vlakke cellen. Verder toegenomen lichtopsluiting kan worden verkregen door de metaallaag vlak te maken en alleen de diëlektrische lagen te textureren.

Diëlektrische achterverstrooiingspatronen voor lichtopsluiting worden verder bestudeerd in Hoofdstuk 7. Dit hoofdstuk beschrijft periodieke verstrooiingpatronen. Met experimenten demonstreren we breedbandige efficiënte lichtopsluiting in 350 nm dikke a-Si:H cellen gegroeid op periodiek gepatroneerde AZO lagen en we laten zien dat deze cellen betere lichtopsluiting vertonen dan referentiecellen gegroeid op Asai-U type textuur. Als gevolg van conforme groei is ook het onderste deel van de a-Si:H laag gepatroneerd. Doordat de diameter van de AZO nanodeeltjes de karakteristieke afstand in het periodieke rooster benadert, omsluiten de AZO deeltjes a-Si:H verstooiers. Met behulp van numerieke simulaties laten we zien dat diëlektrische resonanties zowel voorkomen in de AZO deeltjes als in de a-Si:H verstrooiers en dat de grootte van a-Si:H verstrooiers cruciaal is voor lichtopsluiting.

In Hoofdstuk 8 gebruiken we diëlektrische verstrooiingspatronen voor lichtopsluiting in ultradunne CIGSe zonncellen, met een 460 nm dikke absorberende laag. Met experimenten laten we een fotostroomtoename zien in CIGSe cellen met periodieke roosters van diëlektrische verstrooiers geprint aan de voorkant. Met behulp van numerieke simulaties laten we zien dat de absorptietoename voornamelijk wordt veroorzaakt door een antireflectie-effect in plaats van door lichtopsluiting. Met experimenten aan CIGSe cellen met roosters van SiO_2 nanodeeltjes aan het CIGSe/Mo oppervlak demonstreren we lichtopsluiting in CIGSe cellen; de nanodeeltjes resulteren in een rendementsverhoging van 11.0% naar 12.4%. Met numerieke simulaties laten we zien dat deze diëlektrische verstrooiingspatronen de optische verliezen in het sterk absorberende Mo achtercontact reduceren. Om de absorptieverliezen in het achtercontact verder te reduceren, vervangen we de Mo laag door een ITO laag en we observeren dat, ondanks het feit dat er transmissie van licht is door het achtercontact, de geïntegreerde absorptie in een gepatroneerde ITO-cel net zo hoog kan zijn als de absorptie in een gepatroneerde Mo-cel. Deze geometrie is interessant voor toepassing in tandemcellen.

In de Hoofdstukken 3–8 lieten we zien dat efficiënte lichtverstrooiing bereikt kan worden zowel met verstrooiingspatronen aan de voorkant als aan de achterkant van de cel. In Hoofdstuk 9 presenteren we inzicht in de spatiële frequentieverdelingen van de verstrooiingspatronen. We demonstreren de relatie tussen pieken in de optische absorptiespectra en de verdeling van de spatiële frequenties, die volgt uit de Fourier transformatie van het verstrooiingspatroon. Met behulp van een Monte Carlo algoritme optimaliseren we roosters van diëlektrische verstrooiers om een verhoogde intensiteit van spatiële frequenties te verkrijgen in het frequentiebereik dat overlapt met de golfgeleidermodes van een specifieke celgeometrie. Ook presenteren we een methode die meer vrijheid geeft in het ontwerpen van de spatiële frequenctiespectra van verstrooiingspatronen, gebaseerd op de optimalisatie van ongeordende texturen.

Samenvattend geeft dit proefschrift fundamentele inzichten in lichtopslui-

ting in dunne-film zonnecellen. Het richt zich op verstrooiingspatronen met een hoge verstrooiingefficiëntie, lage optische verliezen en een spatiëel frequenctiespectrum dat op maat gemaakt kan worden voor een specifieke celgeometrie. Dit proefschrift presenteert lichtverstrooiingspatronen die leiden tot een significante absorptietoename in dunne-film zonnecellen zonder een verslechtering van de elektrische eigenschappen van de zonnecel. De concepten die besproken zijn in dit proefschrift zijn toepasbaar op alle typen dunne-film zonnecellen.

List of publications

This thesis is based on the following publications:

- *Optimized spatial correlations for broadband light trapping nanopatterns in high efficiency ultra-thin solar cells*, V. E. Ferry, M. A. Verschuuren, C. van Lare, R. J. Walters, R. E. I. Schropp, H. A. Atwater, and A. Polman, Nano Lett. **11**, 4239 (2011). **(Chapter 3)**

- *Mode coupling by plasmonic surface scatterers in thin-film silicon solar cells*, M. van Lare, F. Lenzmann, M. A. Verschuuren, and A. Polman, Appl. Phys. Lett. **101**, 221110 (2012). **(Chapter 4)**

- *Dielectric back scattering patterns for light trapping in thin-film Si solar cells*, M. C. van Lare, F. Lenzmann, and A. Polman, Optics Express **21**, 20738 (2013). **(Chapter 5)**

- *Efficient nanorod-based amorphous silicon solar cells with advanced light trapping*, Y. Kuang, M. C. van Lare, A. Polman, J. K. Rath, and R. E. I. Schropp, submitted to J. Appl. Phys. **(Chapter 6)**

- *Periodic dielectric back patterns for efficient light trapping in thin-film Si solar cells*, M. van Lare, F. Lenzmann, M. A. Verschuuren, and A. Polman, in preparation. **(Chapter 7)**

- *Light coupling and trapping in ultra-thin Cu(In,Ga)Se_2 solar cells using dielectric scattering patterns*, M. van Lare, G. Yin, A. Polman, and M. Schmid, in preparation. **(Chapter 8)**

- *Optimized scattering power spectral density of photovoltaic light trapping patterns*, M. van Lare, and A. Polman, in preparation. **(Chapter 9)**

Other publications by the author:

- *Controlling Fano lineshapes in plasmon-mediated light coupling into a substrate*, P. Spinelli, C. van Lare, E. Verhagen and A. Polman, Optics Express **19**, A303 (2011).
- *Microphotonic parabolic light directors fabricated by two-photon lithography*, J. H. Atwater, P. Spinelli, E. Kosten, J. Parsons, C. van Lare, J. van de Groep, J. Garcia de Abajo, A. Polman, and H. A. Atwater, Appl. Phys. Lett. **99**, 151113 (2011).
- *Plasmonic light trapping in thin-film solar cell nanostructures*, P. Spinelli, V. E. Ferry, C. van Lare, J. van de Groep, M. A. Verschuuren, R. E. I. Schropp, H. A. Atwater, and A. Polman, Journ. Opt. **14**, 24002 (2012).

Dankwoord

Er zijn veel mensen die hebben bijgedragen aan de totstandkoming van dit proefschift, zowel op professioneel als op persoonlijk vlak. Die wil ik hieronder graag bedanken. Als eerste natuurlijk mijn promotor Albert Polman. Albert, jouw optimisme en opbouwende kritiek hebben me altijd erg gemotiveerd. Dankzij jouw connecties had ik de mogelijkheid om samen te werken met geweldige zonnecelgroepen in Nederland en buitenland. Ook bedankt voor de kans om mijn werk te presenteren op veel internationale conferenties, iets waar ik veel van geleerd heb! Verder wil ik graag mijn co-promotor Ruud Schropp bedanken. Ruud, dankjewel voor de mooie projecten die we samen gedaan hebben en voor alles wat ik door jou geleerd heb over zonnecellen. I am very grateful to Harry Atwater for our fruitful collaboration that led to Chapter 3 of this thesis.

This thesis is also a result of the many discussions with and ideas of the Photonic Materials PV team. Piero Spinelli, Vivian Ferry, Jorik van de Groep, Hugo Doeleman, Bonna Newman, Lourens van Dijk, Julia Attevelt, and Mark Knight. Vivian, thank you for our collaboration that led to Chapter 3 of this thesis. Piero and Jorik, you guys have been the 'hard core' of the PV team. It has been absolutely wonderful to work with you. I could always drop by to discuss results, fabrication, and Lumerical issues with you, which was extremely helpful. I had a great time at all the conferences we visited together. Lourens, Bonna, Julia, Mark, and Hugo, thank you for all the interesting discussions on photovoltaics. Mark, I would also like to thank you very much for the photo you made for my thesis cover and also for explaining me many interesting things about photography.

Ook heb ik veel gehad aan de samenwerking met Marc Verschuuren, die leidde tot meerdere hoofdstukken in dit proefschrift. Marc bedankt dat je mij tijdens mijn masterproject hebt geholpen met het opstarten van de SCIL fabricage op Amolf en verder voor al jouw nuttige adviezen over de nanofabricage.

I really benefited from working together with everybody in the Photonic Materials group. Thank you all so much for all the useful discussions and feedback during and outside group meetings and for the great atmosphere in the group.

Thank you, Robb Walters, Ernst Jan Vesseur, James Parsons, Toon Coenen, Rutger Thijssen, Ruben Maas, Bas Zegers, Benjamin Brenny, and Marie Anne van de Haar. En natuurlijk Petra Rodriguez en Karelia Wrona, bedankt voor jullie secretariële ondersteuning.

I have always enjoyed working in room 2.52. I would like to thank Timmo, Jochen, Hinke, and Arko for this. Timmo en Jochen, bedankt voor het delen van jullie voetbalkennis. Timmo, met jou heb ik gedurende mijn hele promotie een kantoor gedeeld en ik wilde je bedanken voor alle leuke en gezellige gesprekken. I would also like to thank the rest of the Nanophotonics department for the useful discussions during poster sessions, and colloquia and for the joyful conversations during coffee breaks. Tijdens mijn promotie heb ik de kans gehad om samen te werken met een aantal fantastische zonnecelgroepen in en buiten Nederland. De meest langdurige samenwerking die ik heb gehad, was met ECN en deze heeft geleid tot maar liefst 3 hoofdstukken in dit proefschift. Ik wil met name Frank Lenzmann bedanken voor het coördineren van dit project vanuit ECN en voor alle interessante discussies over onze samples, maar ook over de socio-economische aspecten van photovoltaica. Verder wil ik Maarten Dörenkämper en Klaas Bakker bedanken voor hun fantastische technische ondersteuning bij dit project. Ook had ik het genoegen projecten te doen samen met de groep van Ruud Schropp. I would like to thank Yinghuan Kuang for our collaboration that led to Chapter 6. I really enjoyed our collaboration and also our discussions on photovoltaics and China. Verder wil ik graag Karine van der Werf, Martin Huizer en Caspar van Bommel bedanken voor hun geweldige bijdrage aan de projecten die ik samen met de groep van Ruud heb gedaan. I have also been very pleased with our collaboration with the NanoOptiX group of Martina Schmid at the Helmholtz Center in Berlin on CIGSe cells that led to Chapter 8 of this thesis. Guanchao Yin and Martina, thanks very much for the great cells. Guanchao, thank you for the many interesting email discussions we had; from this I learned many things about CIGSe cells.

During the last four years, the number of people working on PV at Amolf has been growing significantly. I would like to thank all the people involved in the NPV/LMPV meetings: Jaime Gomez Rivaz, Silke Diedenhofen, Grzegorz Grzela, Mischa Bonn, Enrique Canovas, Søren Jensen, Artem Bakulin, Stefanie Neutzner, Erik Garnett, Sebastian Öner, Sander Mann, Beniamino Sciacca, Cristina Sfiligoj, Parisa Khoram, Jia Wang, Gede Adhyaksa, Jantina Fokkema, Michiel de Goede, Wim Sinke, Daniël Vanmaekelberg, and Freddy Rabouw. It was great to have these meetings in which I learned a lot from all of you.

Verder ben ik alle cleanroomtechnici ontzettend dankbaar voor hun hulp bij de nanofabricage en karakterisatie. Hans Zeijlemaker, Chris Rétif, Gijs Vollenbroek, Dimitry Lamers, Andries Lof en Peter Govers, ik wil jullie bedanken voor al jullie hulp en advies in de cleanroom en het microscopielab. Ook de ICT afdeling was altijd bereid me te helpen. Ik wil met name Carl Schulz, Wiebe de Boer en Jan van Elst bedanken voor al hun hulp bij het oplossen van onze licentieproblemen met de FDTD simulaties. Ook John Donners van SURFsara heeft

hier enorm bij geholpen. Tatjana van der Ben en André Reinders stonden altijd voor me klaar om pakketjes te versturen naar ECN of naar Berlijn. Bedankt voor jullie hulp hierbij.

Dan zijn er nog de mensen die mij op persoonlijk vlak hebben ondersteund. Ik wil mijn vrienden bedanken voor alle gezelligheid en dan met name Lonneke. Lon, je bent echt een geweldige vriendin die er altijd voor me is. Ik ga onze gezellige treinritjes naar het werk missen. Verder was het altijd leuk om de avonduurtjes door te brengen bij het UCK voor wat ballet. Ik wil mijn ouders en Margot bedanken voor hun steun en hun bijdrage aan het ontstaan van mijn interesse in techniek. Tot slot wil ik Robin ontzettend bedanken voor alle leuke avonden, weekenden en geweldige vakanties en voor het feit dat hij werkelijk altijd voor me klaarstaat.

About the author

Claire van Lare was born in Vlissingen, The Netherlands on May 2, 1987. After receiving her high school diploma from 'Het Goese Lyceum' in Goes in 2005, she did a Bachelor's in Chemistry at Utrecht University, followed by the Master's program Nanomaterials: Chemistry and Physics. She graduated cum laude in 2010 with a thesis on light trapping in thin-film solar cells supervised by Prof. Dr. Albert Polman. In 2010, she started a PhD project at the FOM institute AMOLF, in the group of Prof. Dr. Albert Polman, co-supervised by Prof. Dr. Ruud Schropp. The results of this project are presented in this thesis. In her free time, Claire enjoys ballet dancing and traveling.

The work described in this thesis was performed at the FOM Institute AMOLF, Science Park 104, 1098 XG Amsterdam, The Netherlands in collaboration with Energy Research Center of the Netherlands (Petten, Eindhoven), California Institute of Technology (Pasadena), and Helmholtz Center Berlin (Berlin).